Ph.D. DISSERTATION

A STUDY ON ISOTROPIC ANTENNAS AND TRASFER EFFICIENCY BOUND FOR RADIATIVE WIRELESS POWER TRANSMISSION

방사 무선전력전송을 위한 무지향성 안테나 및 전송 효율 한계에 대한 연구

AUGUST 2020

GRADUATE SCHOOL OF ELECTRICAL

ENGINEERING AND COMPUTER SCIENCE

SEOUL NATIONAL UNIVERSITY

JOONHONG KIM

공학박사 학위논문

A STUDY ON ISOTROPIC ANTENNAS AND TRASFER EFFICIENCY BOUND FOR RADIATIVE WIRELESS POWER TRANSMISSION

방사 무선전력전송을 위한 무지향성 안테나 및 전송 효율 한계에 대한 연구

2020 년 8 월

서울대학교 대학원

전기 • 컴퓨터공학부

김 준 홍

A STUDY ON ISOTROPIC ANTENNAS AND TRASFER EFFICIENCY BOUND FOR RADIATIVE WIRELESS POWER TRANSMISSION

지도 교수 남 상 욱

이 논문을 공학박사 학위논문으로 제출함
2020 년 8 월

서울대학교 대학원
전기 • 컴퓨터공학부
김 준 홍

김준홍의 공학박사 학위논문을 인준함
2020 년 8 월

위 원 장 서 광 석 (인)

부위원장 남 상 욱 (인)

위 원 이 정 우 (인)

위 원 오 정 석 (인)

위 원 박 익 모 (인)

Abstract

In this thesis, research on the radiative-wireless power transmission (R-WPT) using radiated electromagnetic(EM) fields is presented. More specifically, the analysis and design of quasi-isotropic antennas, the analytical study on the optimal transmitting current, and the efficiency bounds are described. In addition, research on the comparison of the EM effects on the human phantom, and the effective implementation of the optimal current distribution are conducted. The research is described sequentially from the passive R-WPT to active R-WPT, which indicate the absence or presence of the power supplying base station.

First, research is conducted on the analysis and design of the passive R-WPT antenna. Considering the ambient environment, an antenna with quasi-isotropic pattern, electrically small size, and high efficiency is proposed. A split-ring resonator (SRR) that radiate quasi-isotropic pattern with electrically small size is used as a basic structure. The analysis on the SRR is well matched with the simulation results. Based on the analysis, folded split-ring resonator (FSRR) is proposed and designed for the passive R-WPT antennas, and verified through the measurement. A dualband and wideband FSRR that can harvest more ambient power is designed as an extended work. The proposed antennas are compared with recent studies showing superior performances. On the other hand, the receiving power of the passive R-WPT is very low due to low power

density of ambient field, a study on the active R-WPT, which can transfer wireless powers from the base station to the mobile antenna, is conducted as a next step.

In the active R-WPT, a study on the way to effectively transfer wireless power to the mobile devices by using a transmitting tower is described. The optimal current distribution of the transmitting surface, and maximum power transfer efficiency (PTE) bounds when the transmitting area is limited are analytically derived. Through the results, it is possible to figure out the maximum efficiency bounds for the mid-range R-WPT and the optimal shape of transmission current distribution that could not be found by the conventional method.

The results indicate that the optimum current distribution on the transmitting surface and the maximum efficiency of radiative WPT depend on the radiating field pattern of the mobile antenna. To generalize the proposed theory, an additional analysis in lossy environment is carried out. The optimal transmitting current and efficiency bound in lossy media is found for a couple of examples. The results are compared with the previous works to verify the proposed theory. Based on the results in lossy media, the EM effects on the human body is investigated.

Lastly, research on the effective implementation of the theoretical current distribution as practical antenna arrays is described. Based on the previous research, two techniques that can effectively realize the ideal current are proposed in designing a thinned array. An optimization using genetic algorithm, and deterministic density

tapering are applied to sample the theoretical current distribution. As a results, the proposed thinned arrays show improved performance compared to the same number of densely arranged regular arrays. In particular, the use of density tapering has advantages in cost, weight, efficiency than the same number of the regular array. In addition, it is possible to transmit wireless power with better efficiency even when the position of the receiver changes.

Keywords: RF energy harvesting antenna, Radiative wireless power transmission, Microwave power transmission (MPT), Efficiency maximization, Implanted medical devices Thinned Array

Student Number: 2014-22551

Table of Contents

List of Figures

List of Tables

Chapter 1. Introduction

1.1. Classification of Wireless Power Transmission

Recently, wireless power transfer (WPT) has drawn substantial interest for increasing number of wireless devices and such as personal mobiles, electric vehicles, wearable sensors, and implantable medical devices (IMDs) [1−3]. For example, the numerous sensors for Internet of Things (IoT) environment that require periodic battery changes can be used for a long time without efforts. Particularly, when WPT is applied to IMD inserted in the human body, the battery can be reduced. Therefore, it can also be used for a long time without additional surgery to replace battery. It is also possible to easily charge the compact mobile devices used in daily life without complicated wires. In particular, when remote charging is implemented for the personal mobile devices, the concept of charging, and the worry about running out of battery may disappears.

WPT can be classified in two ways, non−radiative and radiative WPT, according to the use of radiating fields. The majority of wireless power transfer systems used in commercial products are based on non−radiative fields coupling which is also called reactive near−fields coupling [4−7]. For instance, inductive coupling, which uses the mutual magnetic coupling between a receiver coil and adjacent transmitter coil, is one popular technology [4, 5]. It operates with high power transmission efficiency (PTE), even for very high

power applications. However, a misalignment or change in distance between the transceiver coils can severely degrade the PTE. Another popular technique is magnetic resonant WPT, which uses the coupled resonance of transmitter and receiver coils via the magnetic near fields [6, 7]. Even though it lessens the problem of misalignment and distance variation, there are still issues such as efficiency degradations over long receiving range or physical size of receivers which is unsuitably big for compact mobile devices with high efficiency.

Radiative WPT, which is based on the propagating electromagnetic (EM) waves, has been proposed recently to overcome the operating range limits and alignment sensitivity of the non-radiative fields coupling [8-18]. For example, a retro-directive array has been proposed to direct the transmitting propagating waves onto a receiver [8, 9]. The time-reversal (TR) technique is suggested to focus more EM power onto a mobile antenna using channel properties [10-12]. A phased array beam-forming that increases antenna gain has been studied [13-15]. In addition, interesting studies that use both non-radiative and radiative fields have been conducted to increase the PTE, especially for bio medical applications, where the distance between the base and mobile receiver is close [16-20]. Although previous research has demonstrated several methods to improve the PTE of radiative WPT systems, there has been little discussion of the efficiency bound of the radiative WPT, especially when the transmitting area is limited, which can be important for the practical

design of radiative WPT systems.

1.2. Separation of Operating Regions

In general, there are three regions depending on the characteristics of the existing fields: reactive near-field region, radiating near-field (Fresnel) region, far-field (Fraunhofer) region as shown in the Fig. 1.1. The space where the evanescent fields mainly exist is called reactive near-field region, and where evanescent field and radiating fields coexist is known as radiative near-field (Fresnel) region [21,22]. At the far-field region, the propagating fields can be approximated as plane wave and the radiation pattern is independent of the distance. Although the distinction between the regions are not very clear, the boundary of the region is usually defined as a maximum phase difference greater than $\pi/8$ that occurs by the emitted field from the edge and the center of the transmitter antenna.

On the other hand, the radiative-wireless power transmission (R-WPT), which are dealing with in this study, is a region in which the radiating fields are more dominant than evanescent field, so it is slightly different from the boundary of radiative near-field region in the textbook in [20, 21]. The criterion of the radiative region is described in the Fig. 1.2 using an electrical point source [21]. The magnitude of the evanescent field is depicted as a straight line, while the magnitude of the propagating field is plotted as a dashed line.

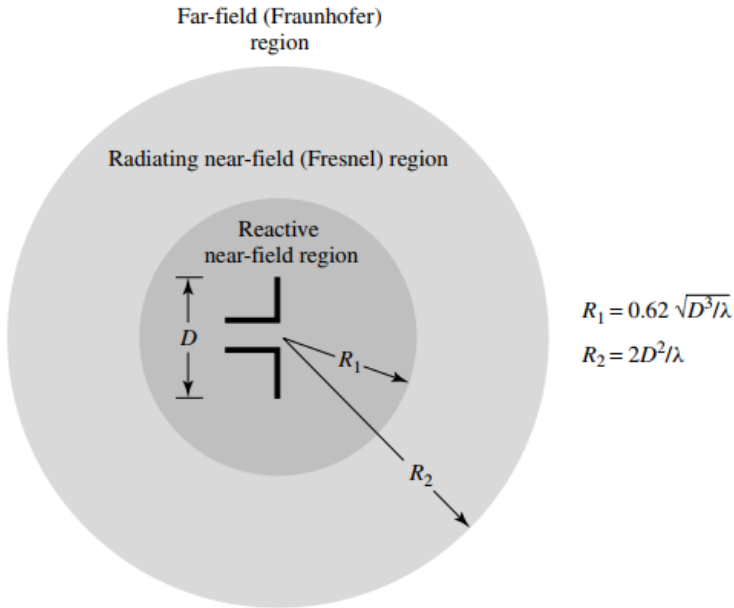

Fig. 1.1. Region separation upon the distance from the transmitting antenna [21].

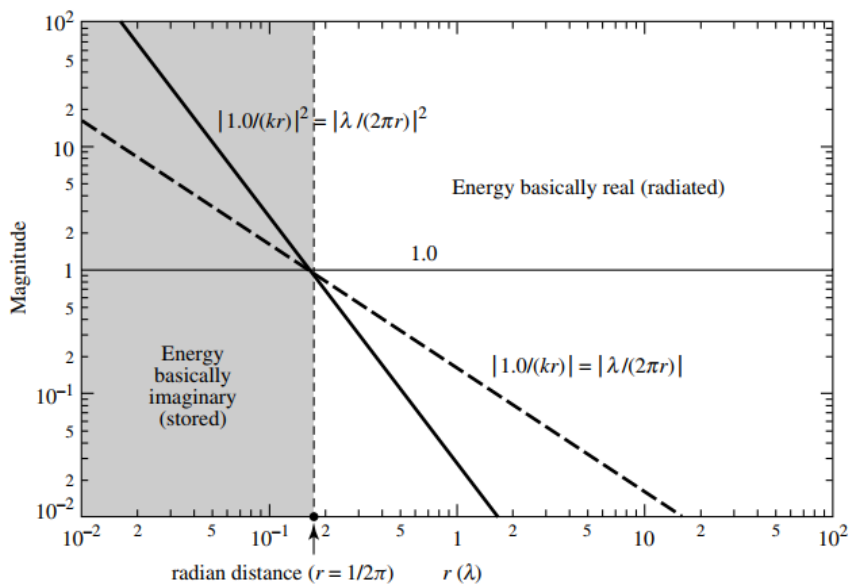

Fig. 1.2 Magnitude of evanescent field and propagating field according to the radial distance [21].

Following that figure, the propagating field predominates the evanescent field from the radian distance, and the area where the magnitude of the propagating field is dominant is defined as radiative region.

For example, consider the current flowing on the large transmitter antenna as sum of equivalent Huygens sources or point sources. The reactive evanescent fields will exist just around each point sources, and even if they are added together, the region where evanescent fields dominate is not as far from each sources as the boundary of the reactive near-field region. It implies that the boundary of the radiative region can be quite different with the boundary of reactive near-field and radiative near-field region. Therefore, this study can be applied from a part of so-called reactive near-field region to far field region, and the distance from the source and even the distance from a scatterer should be carefully determined.

1.3. Passive and Active Radiative-Wireless Power Transmission

In this thesis, two types of the R-WPT, passive R-WPT and active R-WPT, are introduced according to the presence of base station. The passive R-WPT indicates that there is no intended transmitting source. Because the passive R-WPT does not have an intended transmitting base station, it must collect the ambient EM field that exists around itself. By collecting the surrounding EM energy, it can be used as an energy source for low-power sensors. This technology is called radio frequency (RF) energy harvesting (EH), and has recently attracted attention as an energy source for numerous low-power sensor nodes in IoT environments as shown in the Fig. 1.3.

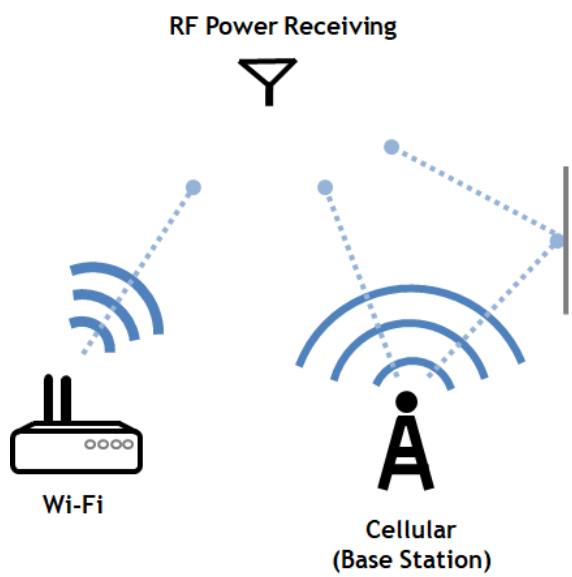

Fig. 1.3 Configuration of RF energy harvesting scenario.

The first thing to consider in order to collect the ambient power using RF EH is to figure out the EM energy in the atmosphere. The measured RF power density at different places, (a)London, UK, (b) Colorado, USA, (c) Seoul, South Korea, are described in the Fig. 1.4 [23-25]. The resultant data indicate the averaged received EM power is strong at GSM 900 and GSM 1800 bands which is approximately a few hundred nW/cm^2 to a few uW/cm^2. In order to harvest weak electromagnetic energy in the atmosphere and utilize it as power source, the design of an antenna for passive R-WPT should consider the effective way to capture ambient power as much as possible. The passive R-WPT can be applied to the low-power devices or self-sustainable devices such as numerous IoT sensors. However, application of the passive R-WPT is restrictive, because it has definite limitation on the receiving power level.

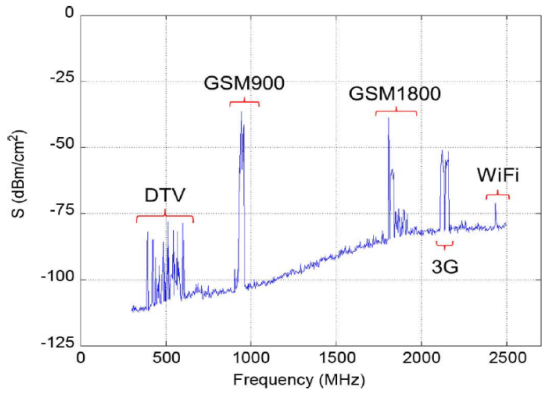

(a)

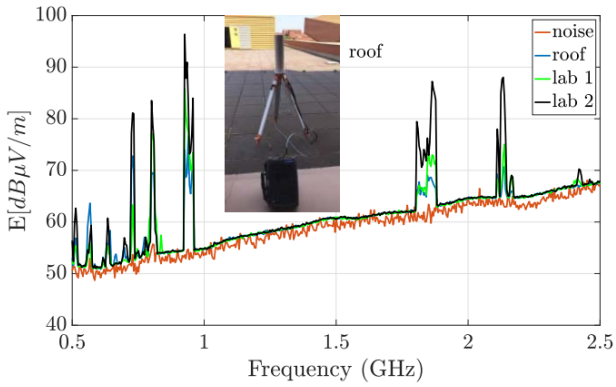

(b)

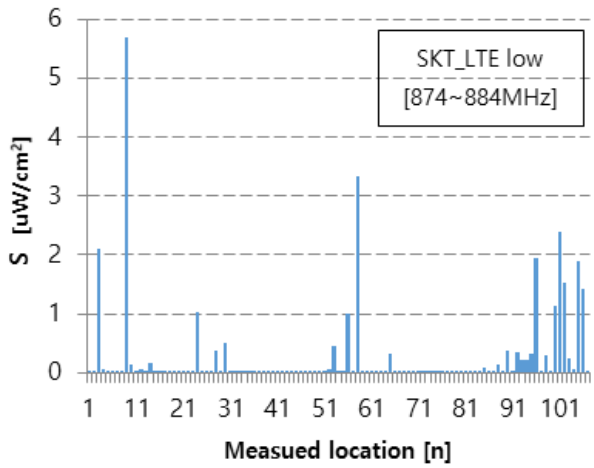

(c)

Fig. 1.4 Measured ambient RF power at ourdoors [23−25]. (a) London. (b) Colorado, USA. (c) Seoul, South Korea.

On the other hand, the active R-WPT, indicating the system including the base station which transmits PTE power for mobile, can provide more power to the receiver as shown in the Fig. 1.5. The EM power emitted by the base station should be properly handled to transfer wireless power to the receiver without harmful effects to the environment. Therefore, the way to maximize PTE is important in the active scenario. The maximum PTE can be improved when the operating distance becomes close. However, the PTE cannot be expected by using Friis equation, which is widely used to calculate link budget, when the distance between the base station and the mobile becomes close. The maximum efficiency versus τ, which contains transmitter and receiver area and distance between them, is plotted in the Fig. 1.6 [26]. The blue line indicates the classic formula based on Friis equation, while the green line indicates the formula including the operation in the radiative region. However, it cannot be applied to practical antennas such as dipole and patch antennas. In this thesis, the maximum PTE is derived analytically regardless of the operating distance and types of receiving antennas.

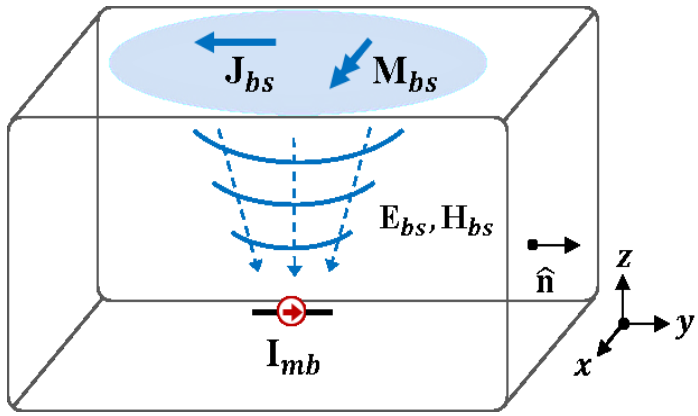

Fig. 1.5 Configuration of active R-WPT scenario. It can operate in various scenarios.

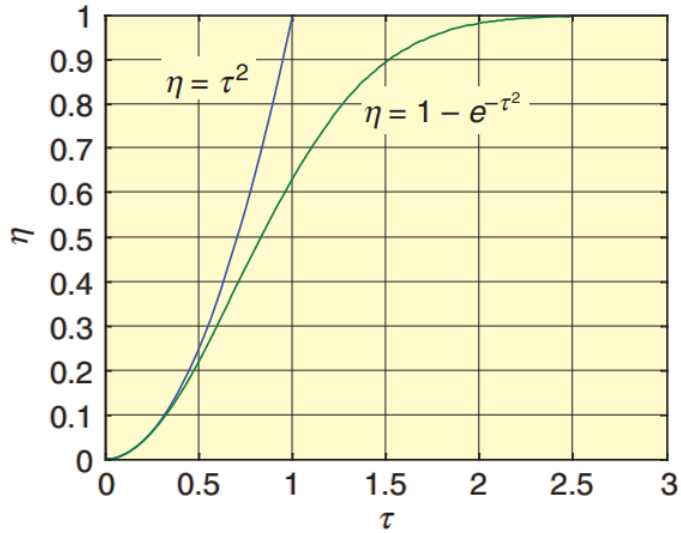

Fig. 1.6 Maximum efficiency for the R-WPT. Green and blue lines are indiacate the far-field and radiative near field region, respectivley [26].

In the active R-WPT, an analysis on the maximization of PTE and optimization of transmitting source is proposed as a first step. Based on the optimal transmitting current, the maximum efficiency bound and the way to minimize transmitting area are described. The active R-WPT is analyzed in the free space (i.e. outdoor and indoor) and extended to the lossy media (i.e. Implanted in human body or concrete layer), which is more general scenario. The applications of R-WPT is described in the Fig. 1.7 [1, 14, 16,27]. In addition, electromagnetic human exposure and the implementation of the optimum transmitting source need to be studied in a practical point of view. Because the active R-WPT is able to control the transmitting power, it has potential to charge mobile devices or implantable medical devices. The outline of 1the R-WPT in this thesis is described in the following figure. The contents are described in order as shown in the Fig. 1.8.

Lastly, the implementation of the theoretical current distribution is described. Array thinning technique is introduced to effectively implement the mathematical current sheet as practical array antennas. It is expected that array thinning of the transmitter can have advantage in terms of weight, cost, power consumption, heat problems, while the PTE may slightly decreases.

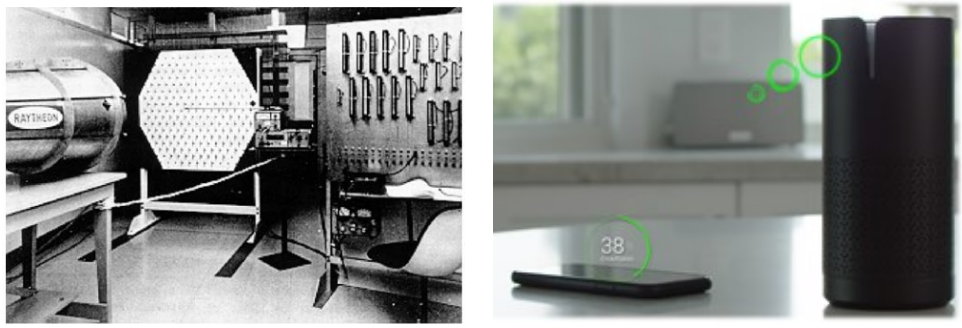

(a) (b)

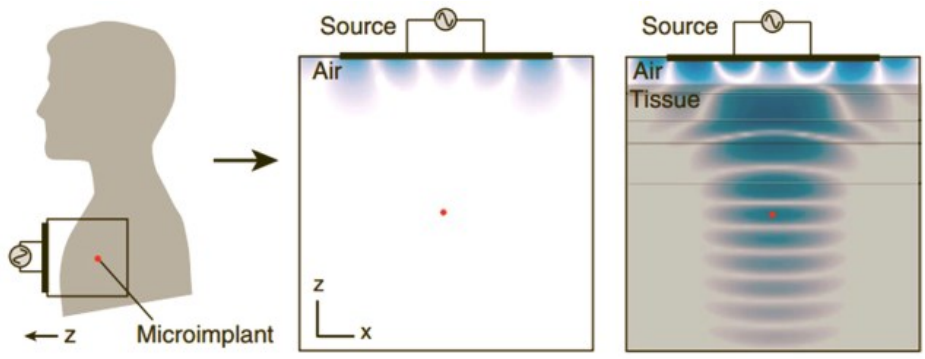

(c)

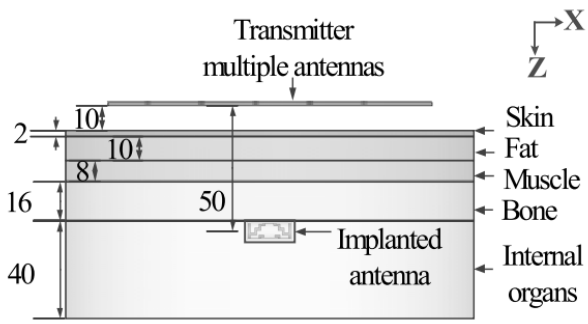

(d)

Fig. 1.7 Application of R-WPT. Examples of lossless R-WPT (a) Array antenna by Raytheon. (b) Indoor R-WPT for mobile devices [1, 14]. (c),(d) Examples of lossy R-WPT : Implatable medical devices [16, 27].

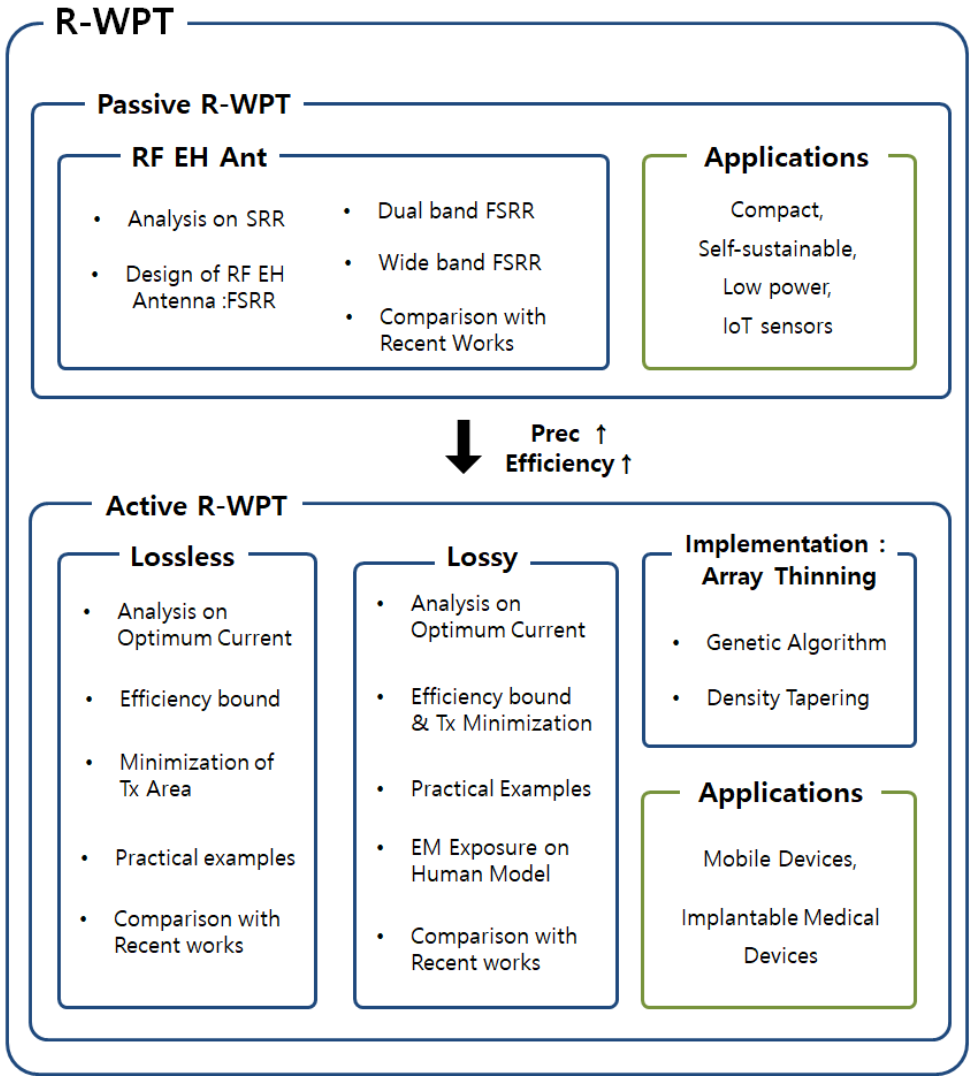

Fig. 1.8. Description of passive and active radiative wireless power transmission.

1.4. References

[1] B. Strassner and K. Chang, “Microwave power transmission: Historical milestones and system components,” Proc. IEEE, vol. 101, no. 6, pp. 1379–1395, Jun. 2013.

[2] Z. Zhang, H. Pang, A. Georgiadis, and C. Cecati, "Wireless Power Transfer – An Overview,” IEEE Trans. Ind. Electron., vol. 66, no. 2, pp. 1044–1058, Feb. 2019.

[3] S. Mingzhao, B. Pavel, K. Polina, "Wireless power transfer inspired by the modern trends in electromagnetics,” Appl. Phys. Rev, vol.4, no.2, pp 021102, Mar. 2017.

[4] J. Dai, D.C. Ludois, “A survey of wireless power transfer and a critical comparison of inductive and capacitive coupling for small gap applications,” IEEE Trans. Power Electron., vol. 30, no. 11, pp. 6017–6029, Mar. 2015.

[5] S.–H. Lee, R.D. Lorenz, "Development and validation of model for 95 %–efficiency 220–W wireless power transfer over a 30–cm air gap,” IEEE Trans. Ind. Appl., vol. 47, no.6, pp 2495–2504, Nov. 2011.

[6] A. Kurs et al., Wireless power transfer via strongly coupled magnetic resonances,” Science, 2007, vol. 317, no.5834, pp.83–86, Jul. 2007.

[7] Y. Li and V. Jandhyala, “Design of retrodirective antenna arrays for short–range wireless power transmission,” IEEE Trans. Antennas Propag., vol. 60, no. 1, pp. 206–211, Jan. 2012.

[8] M. Fu, T. Zhang, C. Ma, and X. Zhu, "Efficiency and optimal loads analysis for multiple-receiver wireless power transfer systems," IEEE Trans. Microw. Theory Tech., vol. 63, no. 3, pp. 801-812, Mar. 2015.

[9] M. Ettorre, W. A. Alomar, A. Grbic, "2D Van Atta Array of Wideband, Wide angle Slots for Radiative Wireless Power Transfer Systems," IEEE Trans. Antennas Propag vol. 66, no. 9, pp. 4577-4585, Sept. 2018.

[10] R. Ibrahim et al., "Experiments of time-reversed pulse waves for wireless power transmission in an indoor environment," IEEE Trans. Microw. Theory Techn., vol. 64, no. 7, pp. 2159-2170, Jul. 2016.

[11] R. Ibrahim et al., "Novel design for a rectenna to collect pulse waves at 2.4 GHz," IEEE Trans. Microw. Theory Techn., vol. 66, no. 1, pp. 357-365, Jan. 2018.

[12] See http://www.ossia.com/cota/.

[13] A. Massa et al., "Array designs for long distance wireless power transmission: State-of-the-art and innovative solutions," Proc. IEEE, vol. 101, no. 6, pp. 1464-1481, Jun. 2013.

[14] See http://energous.com/.

[15] T. T. Ta et al., "A millimeter-wave WPAN adaptive phased array control method using low-frequency part of signal for self-directed system," IEEE Trans. Microw. Theory Techn., vol. 63, no. 8, pp. 2682-2691, Aug. 2015.

[16] Z. Nie, Y. Yang, " A model independent scheme of adaptive focusing for wireless powering to In-Body shifting medical device," IEEE Trans. Antennas Propag., vol. 66, no. 3, pp.1497-1506, Jan. 2018.

[17] D. R. Agrawal et al., "Conformal phased surfaces for wireless powering of bioelectronic microdevices," Nat. Biomed. Eng. vol. 1, no.43, pp.1-9, Mar. 2017.

[18] B. J. DeLong, A. Kiourti, J. L. Volakis, " A radiating near-field patch rectenna for wireless power transfer to medical implants at 2.4 GHz," IEEE J. Electromagn. RF Microw. Med. Biol. vol.2, no.1, pp.64-69, Mar. 2018.

[19] S. Kim, J. S. Ho, A. S. Y. Poon, "Midfield wireless powering of subwavelength autonomous devices," Phys. Rev. Lett., vol. 110, no. 20, pp. 1369-1378, 2013.

[20] S. Kim, J. S. Ho, A. S. Y. Poon, "Wireless power transfer to miniature implants: Transmitter optimization," IEEE Trans. Antennas Propag., vol. 60, no. 10, pp. 4838-4845, Oct. 2012.

[21] C. A. Balanis, Antenna Theory: Analysis and Design, 3rd e.d., Wiley, 2005.

[22] W. L. Stutzman, G. A. Thiele, Antenna Theory and Design, 2nd ed., New York: Wiley, 1998.

[23] M. Piñuela, P. D. Mitcheson and S. Lucyszyn, "Ambient RF energy harvesting in urban and semi-urban environments," in IEEE Transactions on Microwave Theory and Techniques, vol. 61, no. 7, pp. 2715-2726, July 2013.

[24] J. A. Estrada et al., "RF-Harvesting tightly coupled rectenna array tee-shirt with greater than octave bandwidth"
, IEEE Trans. Microw. Theory Techn., accepted.

[25] http://emf.kca.kr

[26] N. Shinohara, "Power without wires," IEEE Microw. Mag., vol. 12, no. 7, pp. S64-S73, Dec. 2011.

[27] J. S. Ho, S. Kim and A. S. Y. Poon, "Midfield wireless powering for implantable systems," in Proceedings of the IEEE, vol. 101, no. 6, pp. 1369-1378, June 2013.

Chapter 2. Passive: Design of RF Energy Harvesting Antenna

2.1. Motivation

In this chapter, we will study the antenna used in the passive R-WPT. This chapter presents a study on the analysis and design of an RF EH antenna that take into account the essential requirements. First, because the electromagnetic energy in the air is incident in a random direction, it must be able to receive electromagnetic waves incident in all directions. Therefore, the RF EH antenna must have an isotropic pattern that can radiate in all directions. Second, it should be designed to be as small as possible so that it can be applied to a small sensor node. Therefore, a compact antenna in terms of electrical size is designed. Lastly, because the energy density of electromagnetic waves in the atmosphere is very weak, the antenna must be able to operate with high efficiency. The following research describes the analysis and design of the RF EH antenna suitable for passive R-WPT environment, aiming to design an antenna with isotropic, electrically small, and high-efficiency features.

2.2. Analytical Study on RF Energy Harvesting Antenna

2.2.1. Previous Research

Designing an ideal isotropic antenna with polarizations in every direction is not possible [1], however, quasi-isotropic antennas have been proposed in recent research [2-8]. A general way to design a quasi-isotropic antenna is to use orthogonal electric or magnetic dipoles which provide omnidirectional radiation pattern, as shown in Fig. 2.1. For instance, a quasi-isotropic radiation pattern is obtained by two perpendicular electric dipoles [2], or four monopoles with a sequential phase feeding network [3]. On the other hand, in [4], a dielectric resonator antenna using an electric dipole combined with an equivalent magnetic dipole generates quasi-isotropic pattern without any complex feeding network as there is a 90-degree phase differences between the radiated fields of an electric and magnetic dipole [9]. However, the quasi-isotropic antennas mentioned above are not electrically small enough to apply to compact wireless platforms.

An electrically small antenna is desirable for the electrically small size of device platforms. Many recent studies have taken advantages of metamaterials (MTMs) to achieve electrically small size of the antennas [10-14]. Particularly, the SRR structure, one of the MTMs, is commonly used in various ways in designing passive elements such as antennas [13-15]. For example, in [15], the several types of SRRs are used to miniaturize the electrical size of antennas with high radiation efficiency. However, the feeding

structures of these SRR antennas are complex and bulky due to the poor radiation characteristics of the SRR structure.

In this chapter, an electrically small quasi-isotropic antenna that uses folded split ring resonator (FSRR) is presented. The compact and simple SRR resonator is used as it can generate an electric dipole and magnetic dipole simultaneously, thereby providing the quasi-isotropic radiation pattern. The magnetic coupling of the folded structure is applied to improve the radiation characteristics of the SRR antenna. The details of the design are described and discussed with general agreements of simulated and measured results.

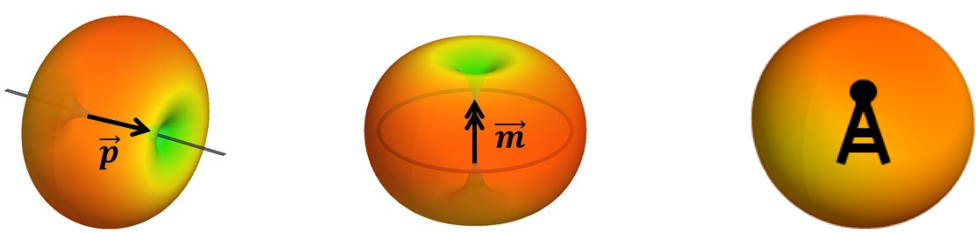

(a) (b) (c)

Fig. 2.1. (a) Radiation pattern of an electric dipole. (b) Radiation pattern of a magnetic dipole. (c) Radiation Pattern of an Isotropic antenna

2.2.2. Analysis on Split-Ring Resonator

In this chapter, an analytical study is presented on the lossless SRR and FSRR. The first step is calculating the magnetic and electric dipole moments in terms of the radiation resistances of the SRR. The folded dipole analysis is then applied to the SRR using the equivalent circuit to verify the operation of the FSRR.

The configuration of the lossless SRR placed on the xy−plane is shown in Fig. 2.2. The SRR can be considered as the curved dipole with the radius (r_0) and gap (g) at the end, therefore, the current distribution can be approximated as a sinusoidal form with the maximum value at the feed center and nearly disappear at the SRR gap. Therefore, the time−varying current can be written as

$$I\ (\varphi, t) = I_0\ \cos\left(\ \frac{\varphi}{2} + \frac{\pi}{4}\ \right)\ \cos(\omega t)\ \hat{\varphi} \tag{2.1}$$

where I_0 is the maximum amplitude of the current, ω is the angular frequency, and the range of φ is ($\frac{-3\pi}{2}, \frac{\pi}{2}$). The radiation resistance ($R_{rad,SRR}$) of the SRR can be obtained by calculating the magnetic and electric dipole moments, which are the sources of the radiated field following the Maxwell's equations.

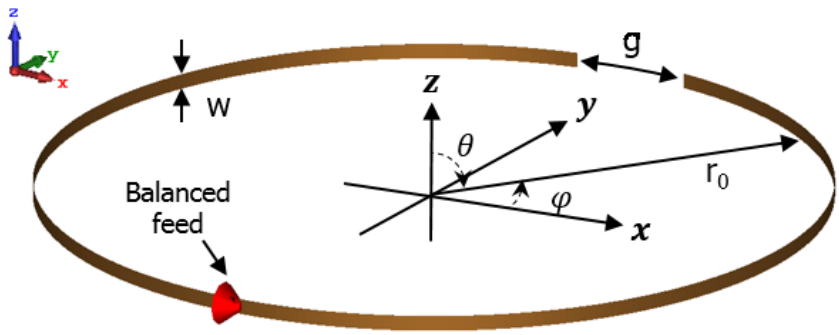

Fig. 2.2. Configuration of the SRR antenna with parameters. W = 0.2, r_0 = 26. g = 10. (unit: mm)

As a first step, the magnetic dipole moment can be calculated [16]:

$$\boldsymbol{m} = \frac{1}{2}\int \boldsymbol{r} \times \boldsymbol{I}\ (\varphi, t)\ dl. \tag{2.2}$$

and the result of the integration is

$$\boldsymbol{m_z} = 2\ I_0\ {r_0}^2\ cos(\omega t)\ \hat{\boldsymbol{z}}. \tag{2.3}$$

The expression of the time averaging power of magnetic dipole moment [17] is:

$$\langle P_{rad,m} \rangle = \frac{\mu_0\ {m_0}^2 \omega^4}{12\ \pi\ c^3}\ . \tag{2.4}$$

where μ_0 is free-space permeability, m_0 is the maximum value of the magnetic dipole moment, and c is the speed of light. The radiation resistance associated with the magnetic dipole moment is

$$R_{rad,m} = \frac{32}{3}\ \pi^3 \eta_0 \left(\frac{r_0}{\lambda} \right)^4 \tag{2.5}$$

where η_0 is the free space intrinsic impedance and λ is a wavelength at the resonance frequency.

The electric dipole moment can be evaluated using the following equation [17]:

$$\boldsymbol{p} = \int \boldsymbol{r}\ \rho_l\ (\varphi, t)\ dl. \tag{2.6}$$

where $\rho_l\ (\varphi, t)$ is the line charge density, which can be obtained from continuity equation below

$$\rho_l\ (\varphi, t) = \frac{I_0}{2\ r_0 \omega}\ \sin\left(\frac{\varphi}{2} + \frac{\pi}{4} \right) \sin(\omega t). \tag{2.7}$$

The integral can be calculated using the antisymmetric line charge density with respect to $\varphi = \left(\frac{-\pi}{2} \right)$, resulting in the x-directed electric dipole moment, as following:

$$\boldsymbol{p_x} = \frac{4}{3} \frac{r_0\ I_0}{\omega}\ \sin(\omega t)\ \hat{\boldsymbol{x}}. \tag{2.8}$$

The radiation resistance of the infinitesimal electric dipole is found using the time averaging power [17]:

$$\langle P_{rad,p} \rangle = \frac{\mu_0 \ {p_0}^2 \omega^4}{12 \ \pi \ c} \tag{2.9}$$

where p_0 is the maximum value of the electric dipole moment. Thus, the radiation resistance of the electric dipole moment is:

$$R_{rad,p} = \frac{32}{27}\pi \ \eta_0 \left(\frac{r_0}{\lambda} \right)^2. \tag{2.10}$$

The total radiation resistance of the SRR, which can be expressed as a sum of $R_{rad,p}$ and $R_{rad,m}$ since each dipole moments is excited by the identical current $\boldsymbol{I} \ (\varphi, t)$, is then

$$R_{rad,SRR} = \frac{32}{3}\pi^3 \ \eta_0 \left(\frac{r_0}{\lambda} \right)^4 + \frac{32}{27}\pi \ \eta_0 \left(\frac{r_0}{\lambda} \right)^2. \tag{2.11}$$

Therefore, the SRR can be considered as the magnetic dipole ($\hat{z}$) with orthogonal electric dipole ($\hat{x}$), which can be the magnetic current source ($\vec{M}$) and electric current source ($\vec{J}$), respectively. According to Maxwell's equations, the radiated electric field from each current source propagates alternately with 90-degree phase shift. Consequently, the SRR provides a quasi-isotropic radiation pattern since the omnidirectional pattern of each dipole which are orthogonally aligned, is added.

2.2.3. Analysis on the Symmetric Folded Split-Ring Resonator

The configuration of the FSRR is shown in Fig. 2.3. The FSRR would be considered as a symmetric (i.e., $W_1 = W_2$) and an asymmetric (i.e., $W_1 < W_2$) FSRR, depending on the width ratio (W_2 / W_1) of the top and bottom SRRs.

For the symmetric FSRR ($W_1 = W_2$), the folded dipole analysis, which uses a transmission line mode (odd mode) and antenna mode (even mode), can be applied to the FSRR so that the input impedance can be written as [18]

$$Z_{in,sym} = \frac{4\ Z_{tl}\ Z_{ant}}{2\ Z_{ant}\ +\ Z_{tl}} \tag{2.12}$$

where Z_{tl} and Z_{ant} are the input impedances of the transmission line mode and antenna mode, respectively. It is worth mentioning that the transmission line mode of the FSRR, which has a curved structure, can be approximated as the transmission line mode in a planar structure when $r_0^2 \gg s^2$ [19]. Thus,

$$Z_{tl} = j\ Z_0 \tan(\ \beta l\ ) \tag{2.13}$$

where β is the phase constant, and l is the half of the circumference of the FSRR, and Z_0 is the characteristic impedance of two-wire transmission line. Referring to [18, 20], Z_0 can be evaluated using the equivalent radius (r_e) approximation to the strip (W) when $\lambda \gg$ W (i.e., $r_e = 0.25$ W) .

$$Z_0 = 120\,cosh^{-1}\left(\frac{s + 2\ r_e}{2\ r_e}\right) \tag{2.14}$$

where s is the distance between top and bottom SRRs as described in Fig. 2.3. The equivalent circuit and its input impedance is presented in Fig. 2.3. The Z_{tl} is calculated using (2.13), whereas the Z_{ant} is evaluated using the equivalent circuit of the SRR with the five elements model [21], which are extracted from the SRR simulation results. The input impedance of the equivalent circuit and the simulation correspond well near the resonance frequency (908 MHz).

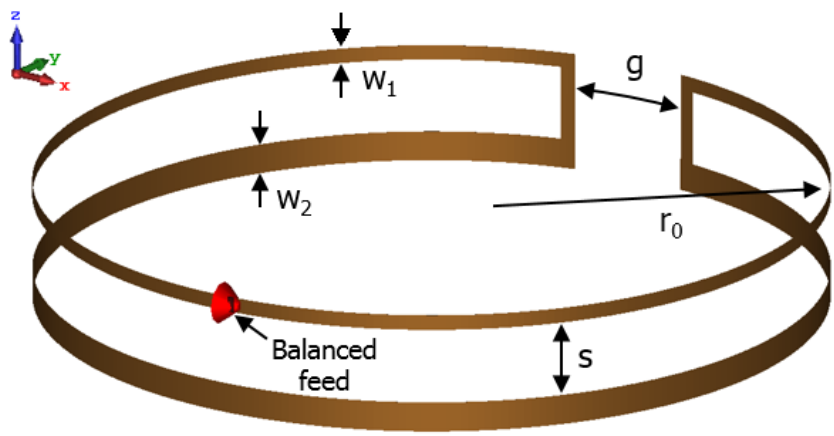

Fig. 2.3. Configuration of the FSRR antenna with parameters. W_1 = 0.2, r_0 = 26, s= 5, g = 10. (unit: mm)

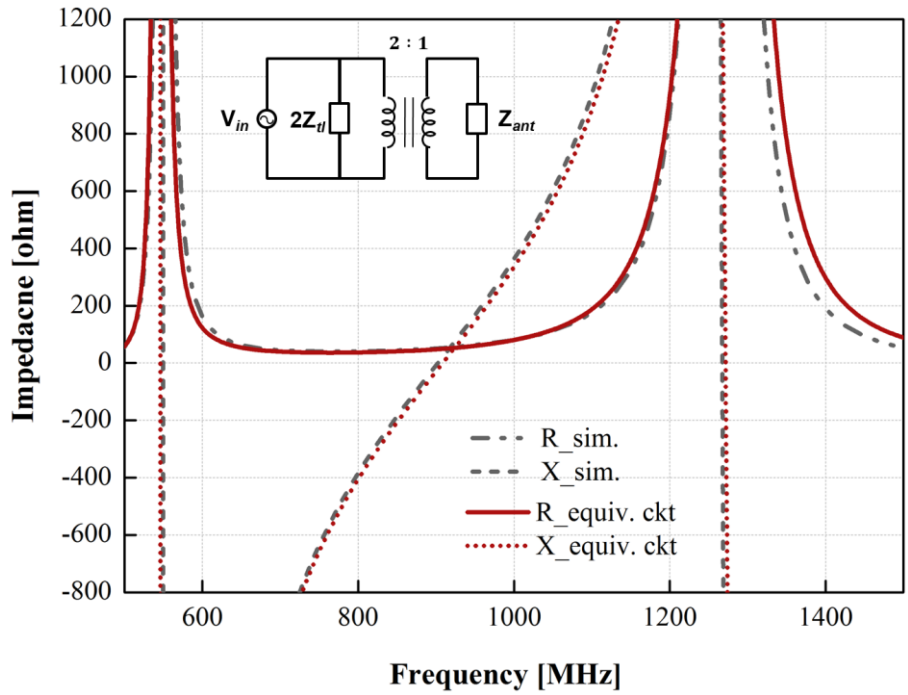

Fig. 2.4. Equivalent circuit model of the symmetric FSRR and its input impedance with simulated results. (W_2 / W_1 = 1)

The point of interest is the input impedance at the fundamental resonance (i.e., $l \approx \lambda/4$), therefore, further study is conducted on the radiation resistance of the FSRR at the resonance with respect to the electrical size (ka). The antenna mode of the lossless FSRR can be understood as the SRR at the fundamental resonance, thus, Z_{ant} would be $R_{rad,SRR}$ in the lossless condition. At the fundamental resonance, the Z_{tl} diverges to infinity and the Z_{ant} would be $R_{rad,SRR}$, therefore, the input impedance of the symmetric

FSRR is

$$Z_{in,sym} = \ 4 \ R_{rad,SRR} \qquad (2.15)$$

which is evaluated in (2.11).

The calculated and simulated radiation resistances at the resonance of the SRR and FSRR in terms of the electrical size are presented in Fig. 2.5. The simulated radiation resistance values are extracted from the full-wave simulator CST at various resonant frequencies by changing the relative permittivity of the lossless substrate, which is circular ring shape inside the FSRR with 1mm thickness. The analytical expression in (2.15) is then calculated using the resonance frequencies of the simulation results. The parameters described in Fig. 2, which satisfy the conditions for the analysis, are used for the calculation (2.14). The simulated and calculated results show reasonable agreement, even though small discrepancies appear around the lower resonances, which are caused by the capacitive loading effect at the gap (g) when the relative permittivity of the substrate is high. The results verify the folded dipole analysis on the FSRR, indicating that the poor radiation properties of the SRR can be enhanced by applying the folded structure and maintaining its quasi-isotropic radiation pattern.

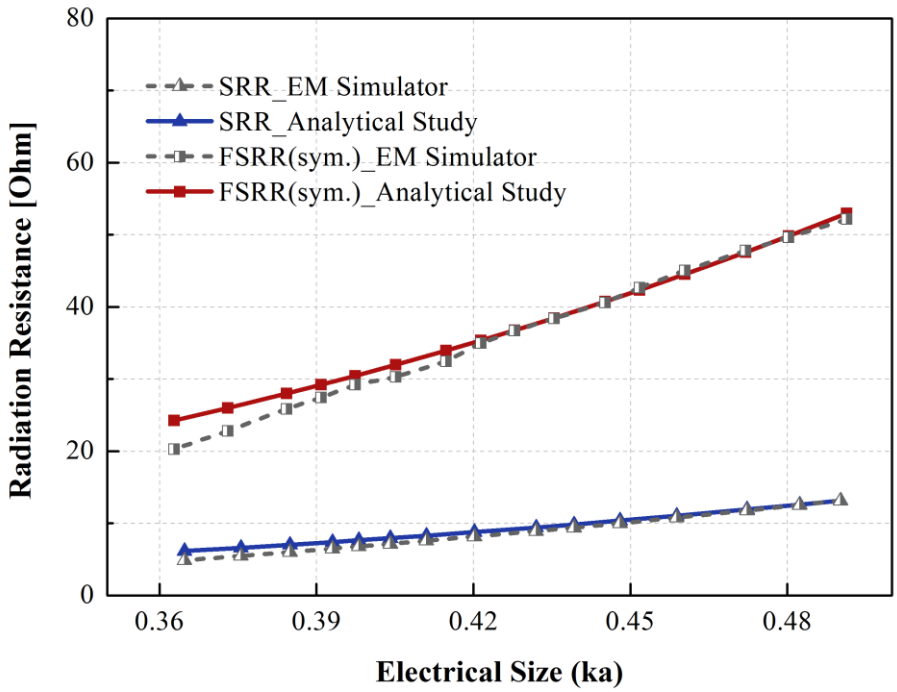

Fig. 2.5. Calculated and simulated radiation resistance plot for the SRR and symmetric FSRR.

2.2.4. Analysis on the Asymmetric Folded Split-Ring Resonator

The analysis of the asymmetric FSRR ($W_1 < W_2$) can be developed with the current ratio of the top and bottom strips of the FSRR, which determine the impedance transform ratio. The current divided on each conductor strip of the asymmetric FSRR can be represented as a current division factor [22] with an equivalent radius approximation to the strip width (i.e., $r_{e1} = 0.25\ W_1$, $r_{e2} = 0.25\ W_2$):

$$a = \frac{ln(s\ /\ r_{e1})}{ln(s\ /r_{e2})} \tag{2.16}$$

where s is spacing, r_{e1} and r_{e2} are equivalent radius of W_1 and W_2, respectively. The input impedance of the asymmetric FSRR at the center of W_1 can then be found as

$$Z_{in,asym} = \frac{2\ (1+a)^2\ Z_{tl}\ Z_{ant}}{(1+a)^2\ Z_{ant}\ +\ 2\ Z_{tl}}. \tag{2.17}$$

The equivalent circuit of the asymmetric FSRR and its input impedance with simulated results are described in Fig. 2.6, and they show acceptable agreement. The radiation resistance of the asymmetric FSRR is also analyzed to describe the features of the FSRR. As Z_{tl} diverges to infinity and Z_{ant} is $R_{rad,SRR}$ at the fundamental resonance, as explained in the previous section, the input impedance becomes

$$Z_{in,asym} = (1+a)^2 \; R_{rad,SRR}. \tag{2.18}$$

The calculated and simulated radiation resistances of the asymmetric FSRR, when the width ratio (W_2 / W_1) is 2 and 4, are compared in Fig. 2.7. The other parameters are set identically with the symmetric FSRR case, and the relative permittivity of the substrate is changed to control the resonant frequency. The results are well matched for both cases even if small errors are present due to the capacitive loading effect near the gap. The results imply that the use of the asymmetric FSRR structure further improves the radiation performances of the antenna by simply increasing the width ratio (W_2 / W_1) or decreasing the spacing (s), which makes the current division factor (a) large.

In Fig. 2.8, the calculated radiation pattern of the asymmetric FSRR is presented with the simulated results. Since the FSRR is an impedance transformed SRR at the resonance, as followed by the equivalent circuits, the radiation pattern can be calculated using the magnetic and electric dipole moments of the SRR. The compared radiation patterns are well matched and present a quasi-isotropic pattern of the FSRR.

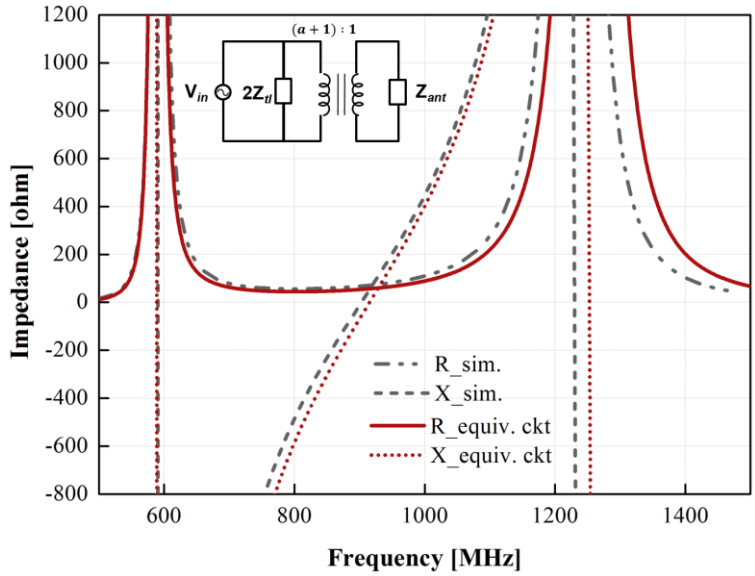

Fig. 2.6. Equivalent circuit model of the asymmetric FSRR and its input impedance with simulated input impedance. (W2 / W1 = 4)

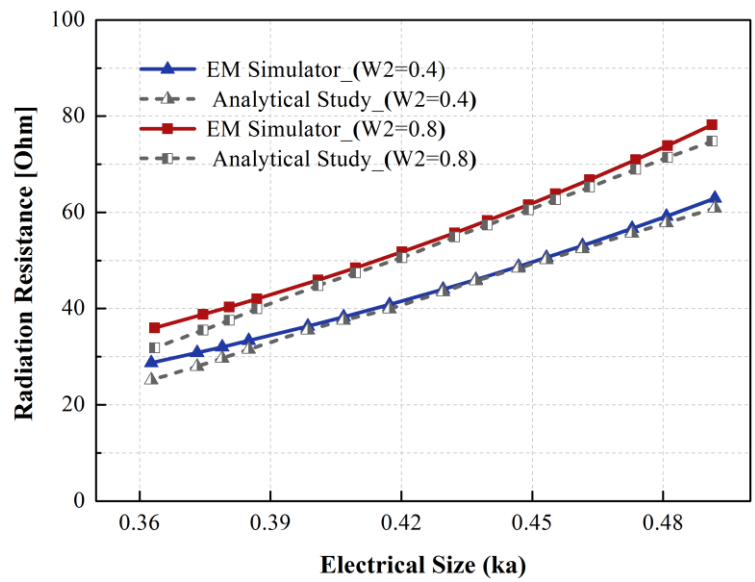

Fig. 2.7. Calculated and simulated radiation resistance plot of the asymmetric FSRR. (W2 / W1 = 2, W2 / W1 = 4)

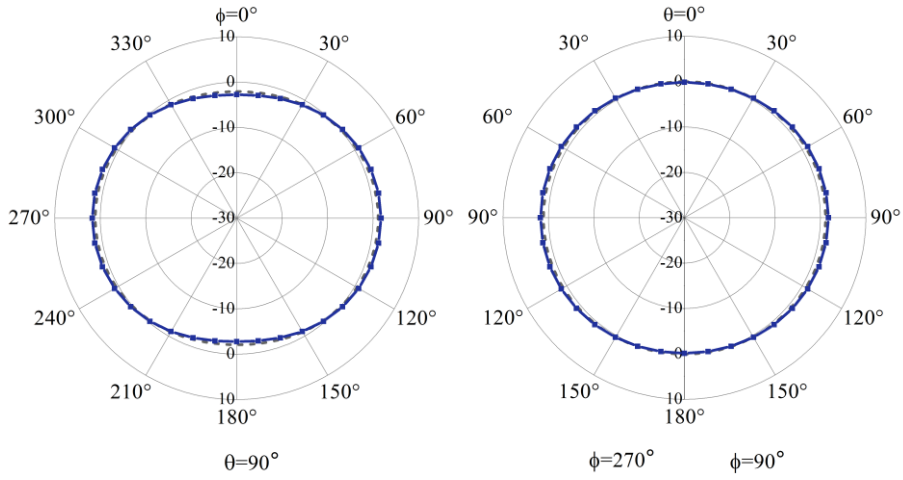

(a) (b)

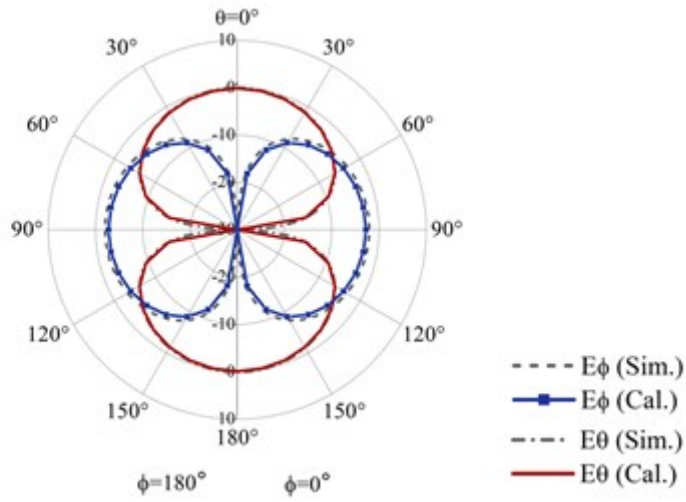

(c)

Fig. 2.8. Simulated and calculated polar pattern at (a) xy−plane, (b) yz−plane, (c) xz−plane

2.3. Design of RF Energy Harvesting Antenna

2.3.1 Antenna Design

Following the analysis in the previous section, the FSRR operating at 900MHz ISM band is designed. The configuration of the proposed antenna is shown in Fig. 2.9(a). The antenna is designed on the Rogers ULTRALAM 3850 flexible substrate with thickness = 25um, εr = 2.9, tan δ = 0.002, and half ounce copper. The proposed antenna is based on SRR structure to take advantage of its benefits, such as the quasi-isotropic radiation pattern and the electrically small size of the resonator. However, the input impedance of the single SRR is too low for direct feeding to a 50-ohm coaxial cable. The radiation characteristics of the single SRR are improved by applying the concept of folded dipole, which uses magnetic coupling of closely spaced dipoles [18]. According to the transmission line and antenna mode analysis of the half-wave folded dipole in [18], the input impedance can be increased by a factor of n2 when there are n-elements of closely spaced half-lambda dipoles. Thus, the radiation characteristics of the single SRR are improved by applying the folded structure, as shown in Fig. 2.9(a). The ratio of the width of the lower SRR (w1) and the upper SRR (w2) is chosen to match the input impedance as 50 ohm.

The FSRR is then made more compact by providing capacitive loading using the interdigital capacitors (IDCs) at the end of two arms, where the voltage would be maximum. The resonance frequency of the FSRR can be easily tuned by controlling the dimensions of the

IDCs. The length (w4), width (w5), and the gap (g3) of the IDCs are determined to set the resonance frequency as 886 MHz. The size of the FSRR is 44 × 44 × 6.5 mm3 (0.13× 0.13 × 0.02 λ3) or ka = 0.41. The values of the parameters are optimized using CST full–wave simulator and are listed in Table2.1.

TABLE 2.1

Design parameters of the proposed antenna

Symbol	Quantity [mm]	Symbol	Quantity [mm]
r	22	w1	1.4
h	6.5	w2	4.3
g1	1	w3	4
g2	0.8	w4	0.7
g3	0.8	w5	1.4

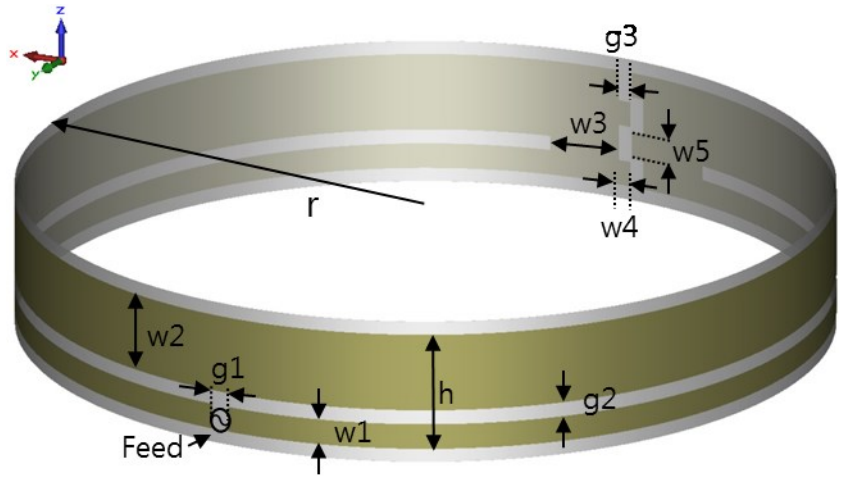

(a)

(b)

(c)

Fig. 2.9. (a) Geometry of the proposed antenna. (b) Perspective view of the fabricated antenna. (c) Rear view of the fabricated antenna.

2.3.2 Results and Discussion

The proposed FSRR antenna is fabricated through a flexible printed circuit board (FPCB) process with the flexible substrate. The perspective view and rear view of the fabricated antenna are shown in Fig. 2.9(b) and (c) respectively. The FSRR antenna with the flexible substrate is soldered at the front center to form a circular shape. The inner and outer conductors of the coaxial cable are connected to the left and right sides of the feeding gap (g1), respectively. The proposed antenna has balanced feeding structure by putting ferrite beads on the outer conductor which are used to prevent the current from flowing the coaxial cable and disturbing the radiation of the antenna.

It is worth mentioning that the radiation of the FSRR antenna with an electric dipole and magnetic dipole differs from that observed with the magneto-electric dipoles which provide unidirectional radiation pattern [23, 24]. The former excites an electric dipole and a magnetic dipole simultaneously, while the latter excites two dipoles with 90-degree phase differences. Therefore, the radiated electric field of the FSRR would not be canceled out, and it forms quasi-isotropic radiation pattern with dual-polarization in the x-direction and y-direction.

The simulated and measured reflection coefficients of the proposed antenna are shown in Fig. 2.10 The resonance frequency of the fabricated antenna is 888 MHz and the resonance frequency of the simulation result is 886 MHz. With reference to Fig. 2.10(a), the

measured 10−dB FBW is 1.8% (881 – 897 MHz). The simulated and measured values of the realized gain and total radiation efficiency are plotted in Fig. 2.10(b). The measured gain of the fabricated FSRR antenna varies in the range of 1.6 dBi to 2.1 dBi in the 10−dB bandwidth, whereas the gain of the simulated one varies from 0.4 dBi to 1.3 dBi. The measured gain shows higher value than the simulated one as a result of the non−uniform radiation pattern, which is caused by measurement tolerances. The peak value of the measured total radiation efficiency is 91% with a lower bound of 81% across the bandwidth. The simulated and measured results of the FSRR antenna show reasonable agreements although small discrepancy arises due to fabrication tolerances.

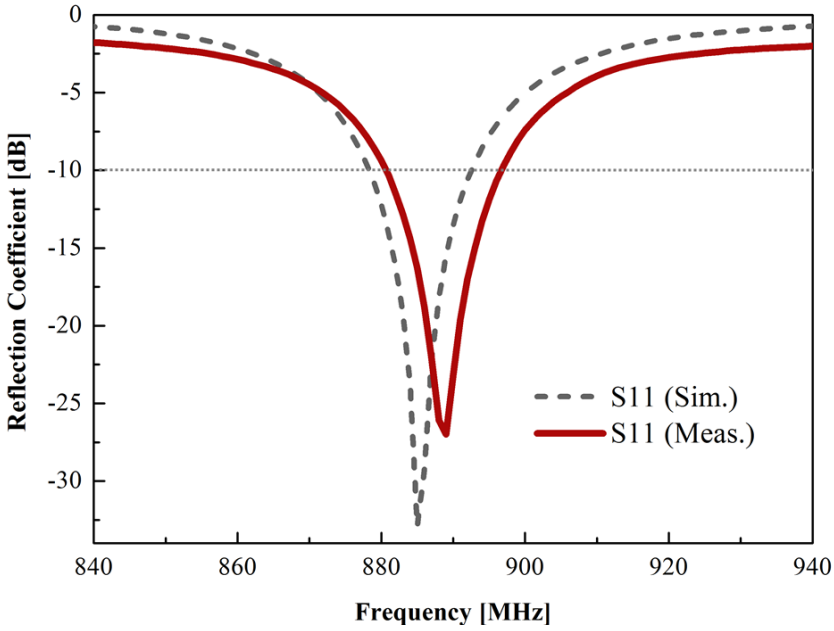

(a)

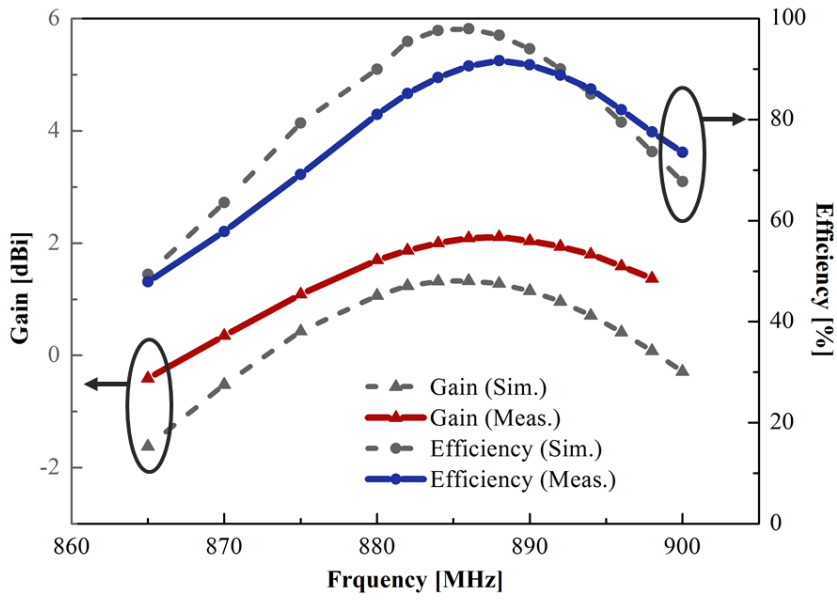

(b)

Fig. 2.10. Simulation and measurement results of (a) Input reflection coefficient. (b) Maximum realized gain and total radiation efficiency.

The simulated and measured radiation patterns in elevation (xz, yz) plane and azimuthal (xy) plane are shown in Fig. 2.11 at the resonance frequency of 886 MHz and 888 MHz, respectively. Based on the polar plot result in the xz plane as described in Fig. 2.11(a), the radiation of two dipoles can be observed by the E_θ component of the x−directed electric dipole and the E_ϕ component of the z−directed magnetic dipole. The electric fields generated from the electric and magnetic dipole radiate with dual−polarization along the x and y direction. In Fig. 2.11 (b) and (c), the E_θ components appeared only in the measurement results, due to unexpected scattering in the experimental environments. As shown in Fig. 2.11, the simulated gain deviation is 2.3 dB with 1.33dBi maximum gain and −1.01 dBi minimum gain. The simulated gain deviation value is less than 3dB, which is the theoretical limit of gain deviation when it is based on two ideal point sources [4] since the proposed antenna does not generate two ideal point sources.

Fig. 2.12 shows the measured gain contour of the proposed antenna at 888 MHz. The maximum gain appears around the y−axis, where omnidirectional radiation patterns of the electric dipole and magnetic dipole are overlapped. The measured gain deviation is 5.2 dB with 2.12 dBi maximum gain and −3.08 dBi minimum gain, as depicted in Fig. 2.12.

Table.2.2 lists the antenna performances of the proposed FSRR antenna compared with recently studied quasi−isotropic antennas [2−4]. As the table shows, the proposed antenna is the most compact

in terms of the electrical size (ka = 0.41) with a minimum value of the measured gain deviation (Δ = 5.2 dB), despite its lack of any requirement for complex feeding structures.

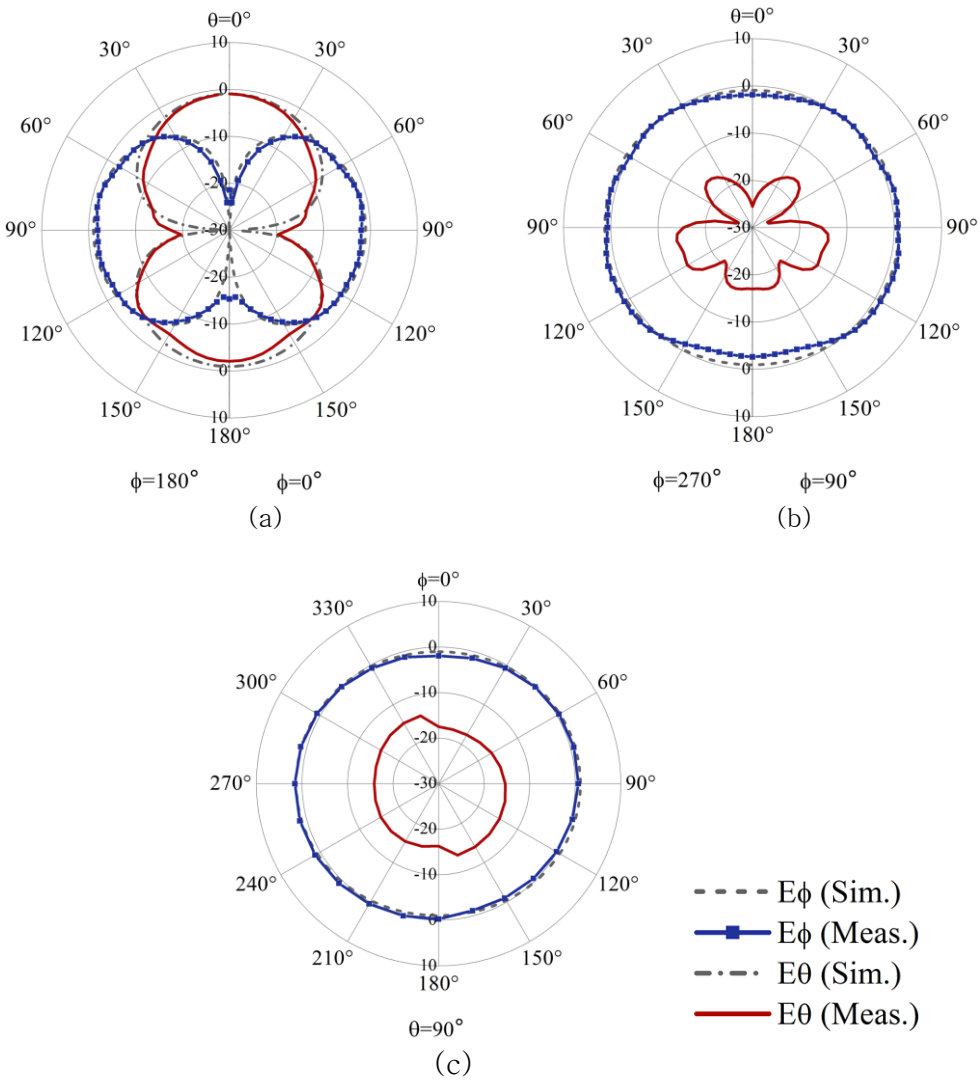

Fig. 2.11. Simulated (886 MHz) and measured (888 MHz) radiation patterns of the proposed antenna. (a) xz−plane. (b) yz−plane. (c) *xy*−plane.

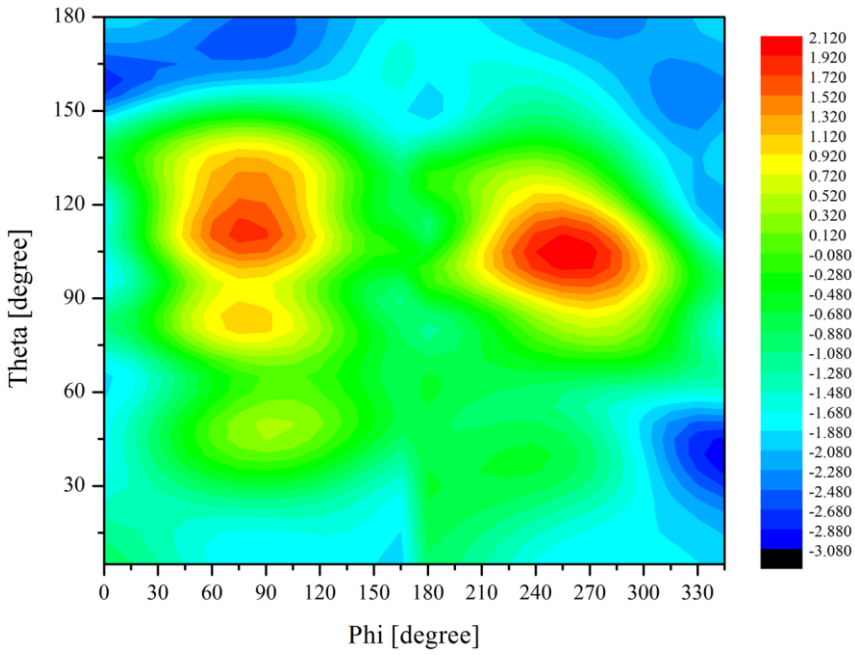

(a)

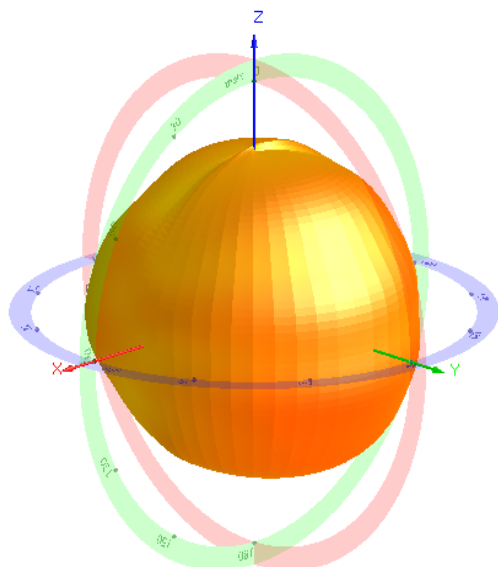

(b)

Fig. 2.12. (a) Measured gain contour of the proposed antenna. (b) Measured 3-dimensional radiation pattern.

Table.2.2 lists the antenna performances of the proposed FSRR antenna compared with recently studied quasi-isotropic antennas [2-4]. As the table shows, the proposed antenna is the most compact in terms of the electrical size (ka = 0.41) with a minimum value of the measured gain deviation (Δ = 5.2 dB), despite its lack of any requirement for complex feeding structures

TABLE 2.2
COMPARISON OF EXPERIMENTAL RESULTS OF THE QUASI-ISOTROPIC ANTENNAS

	This work	[2]	[3]	[4]
Resonant Frequency (MHz)	888	2450	2450	2440
Electrical Size	0.41	1.16	1.63	1.05
Measured Gain deviation (dB)	5.2	6.64	5.75	5.6
Fractional Bandwidth (%)	1.8	11	20.8	6.9
Operation Principle	Electric dipole with magnetic dipole	Two electric dipoles	Four electric monopoles	Electric dipole with magnetic dipole

2.2.3. Conclusion

A compact quasi-isotropic antenna using FSRR is presented in this letter. The proposed antenna is based on the single SRR structure, which can excite the magnetic dipole and orthogonal electric dipole at the same time to form the quasi-isotropic radiation pattern. The folded structure and capacitive loading of IDCs are applied to the single SRR to improve its radiation characteristics and make the electrical size more compact. The resonance frequency of the FSRR antenna is 888 MHz and the FBW is 1.8 % with at least 81 % of total radiation efficiency. The electrical size is ka = 0.41 and the measured gain deviation is 5.2 dB, which are remarkable results compared with those of recently reported studies. The operation of the proposed antenna is verified experimentally with reasonable agreements. Therefore, the proposed antenna can be used as a promising candidate for compact wireless communication systems with quasi-isotropic radiation features.

2.4. RF Energy Harvesting Antenna with Dual-band Operation

2.4.1 Motivation

In order to collect as much power as possible, it is necessary to expand the operating band. In this section, the design of an isotropic, compact, high-efficiency antenna that operates independently in a dual band is proposed. A dualband quasi-isotropic antenna is described by implementing SRRs orthogonally and applying the folded dipole structure. Compared to the conventional quasi-isotropic antennas, which can operate at singleband, the proposed antenna provides dualband operation within a compact size as a first time.

2.4.2 Antenna Design

The proposed antenna configuration is described in Fig. 2.13(a) with parameter values. For better understanding of the suggested antenna structure, it would be considered as two parts, horizontal (xz) and vertical (yz) elements, separately. The horizontal element is based on the SRR, which provides quasi-isotropic radiation pattern by exciting an electric dipole ($\hat{x}$) and perpendicular magnetic dipole ($\hat{y}$) simultaneously. The folded dipole structure is then applied to the SRR, which is FSRR, to enhance the radiation performances of the antenna. The input resistance can be easily controlled by adjusting the width ratio (w_2 / w_1) of the FSRR and the resonance frequency would be tuned by changing the radius (r) and the gap (g) of the

FSRR.

For the design of the dualband quasi-isotropic antenna using FSRRs, the mutual coupling between the elements should be considered. Since the SRR can be regarded as the equivalent electric dipole and magnetic dipole, the mutual coupling would be significantly reduced when the equivalent dipoles of each element are orthogonal. The additional FSRR element is, thus, implemented vertically for the high band operation. As a results, the elements can independently resonate at each band.

The proposed antenna is fabricated on the flexible substrate, Rogers ULTRALAM 3850, with 4 mils thickness, $\varepsilon_r = 2.9$, $\tan\delta = 0.002$. The horizontal element is etched on the front surface of the substrate while the vertical element is etched on the reverse side. The development figure is then folded and soldered. The 50-ohm balanced feed is connected to the both FSRRs through via holes and a ferrite bead is used to prevent the current from flowing on the outer conductor of the coaxial cable. The proposed antenna also can be fabricated using two planar printed circuit boards (PCB) for mechanical stability.

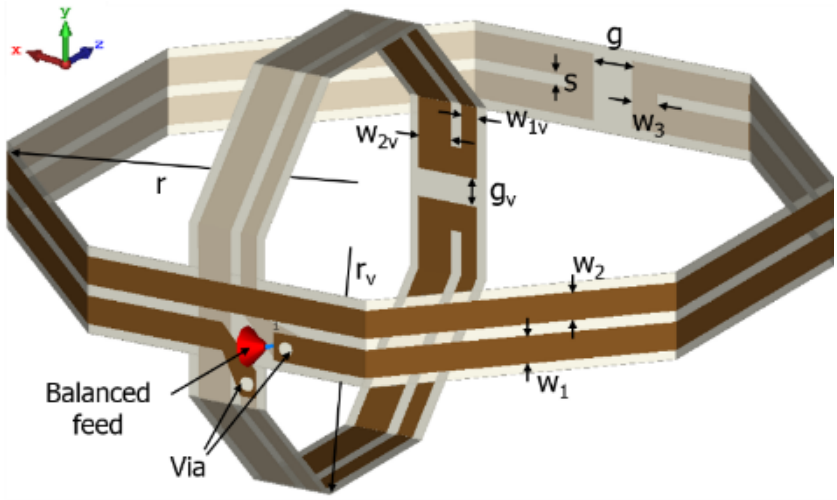

(a)

(b)

Fig. 2.13. Configuration of the proposed antenna. $W_1 = W_2 = 2$, $W_{1v} = 0.8$, $W_{2v} = 3$, $W_3 = 2$, $r = 28$, $g = 3$, $r_v = 18.4$, $g_v = 0.7$, $s = 0.8$. (unit: mm) (a) Geometry of the antenna, (b) Perspective view of the fabricated antenna

2.4.3 Results and Discussion

Fig. 2.14 shows the simulated current distribution at each resonance using CST full-wave simulator. It indicates that the elements resonate at their own frequency with little coupling as intended. In Fig. 3a, the simulated and measured reflection coefficients are depicted. The measured resonant frequencies are 792 MHz and 1124 MHz, with the fractional bandwidth of 2.8 % and 1.8 %, respectively. The measured total radiation efficiency across the bandwidth is higher than 86 % at the low band (LB) and 85.5 % at the high band (HB). as described in Fig. 2.15(b). The measured gain is 1.8 dBi (LB) and 2.33 dBi (HB), which are higher than simulated gain results. The differences might be caused by the measurement environments, which distort the uniform radiation pattern.

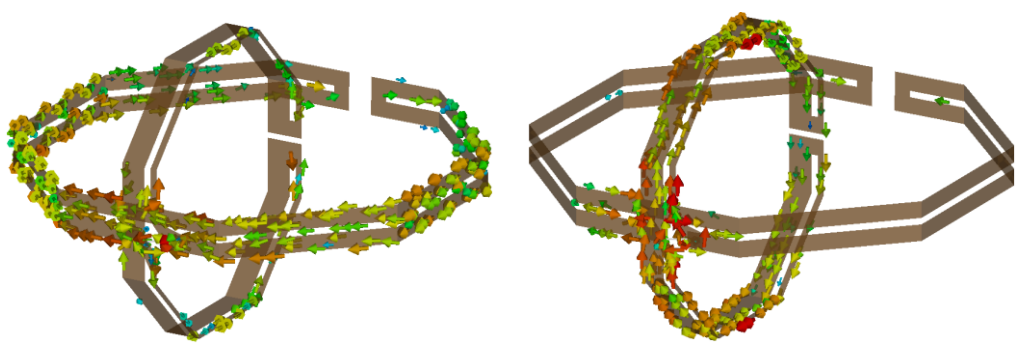

(a) (b)

Fig. 2.14. Simulated current distribution of the proposed antenna. (a) Low band resonance. (b) High band resonance

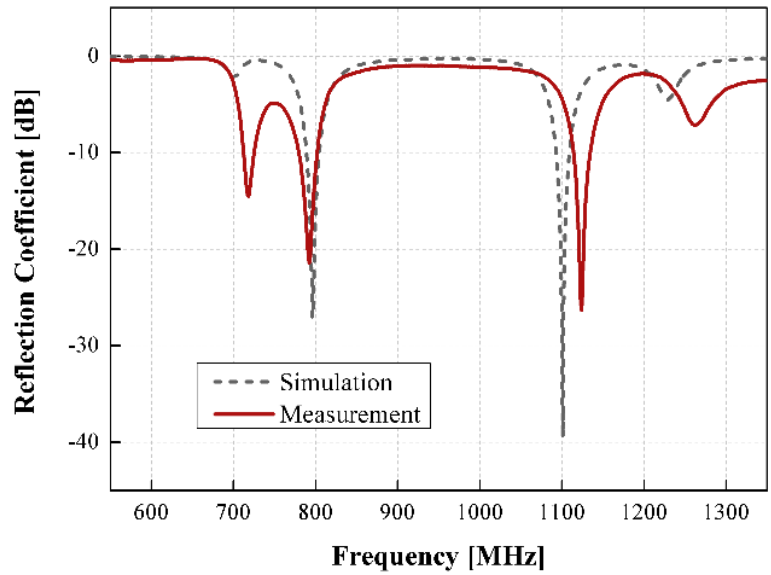

(a)

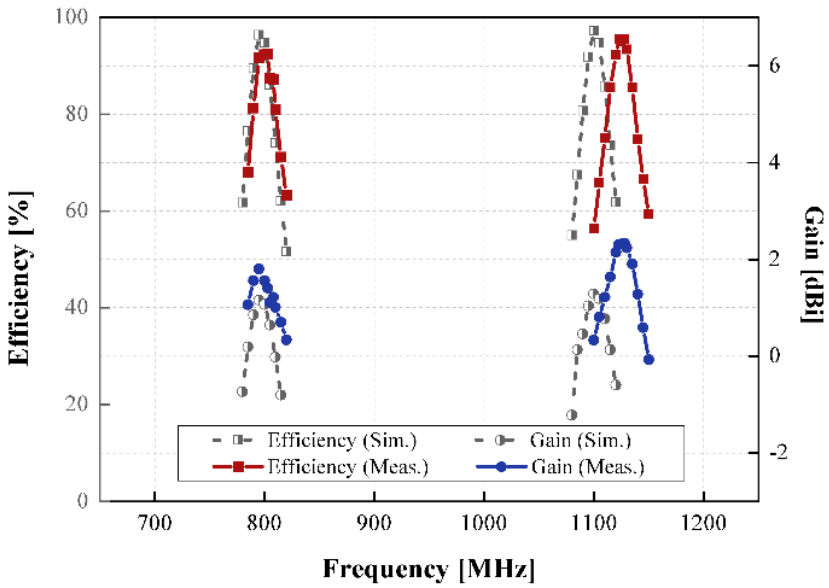

(b)

Fig. 2.15. Simulated and measured results of the proposed antenna. (a) Reflection coefficient. (b) Total radiation efficiency and realized gain

The radiation patterns are plotted in Fig. 2.16 for both LB and HB resonances. The radiated electric field of the equivalent electric dipole and magnetic dipole can be verified from the theta and phi components in Fig. 2.16(a) and Fig. 2.16(d). The measured results generally agree with the simulated results although small discrepancy arises due to fabrication and measurement tolerance. The performances of the proposed quasi-isotropic antenna are compared in Table.2.3. As shown in the table, the suggested work can provide quasi-isotropic pattern at dualband, while other studies can operate at singleband. To the best of the author's knowledge, no previous work has been proposed the dualband quasi-isotropic antenna. In addition, the designed antenna shows an electrically small size and moderate gain deviation, which indicate the uniformity of the radiation pattern.

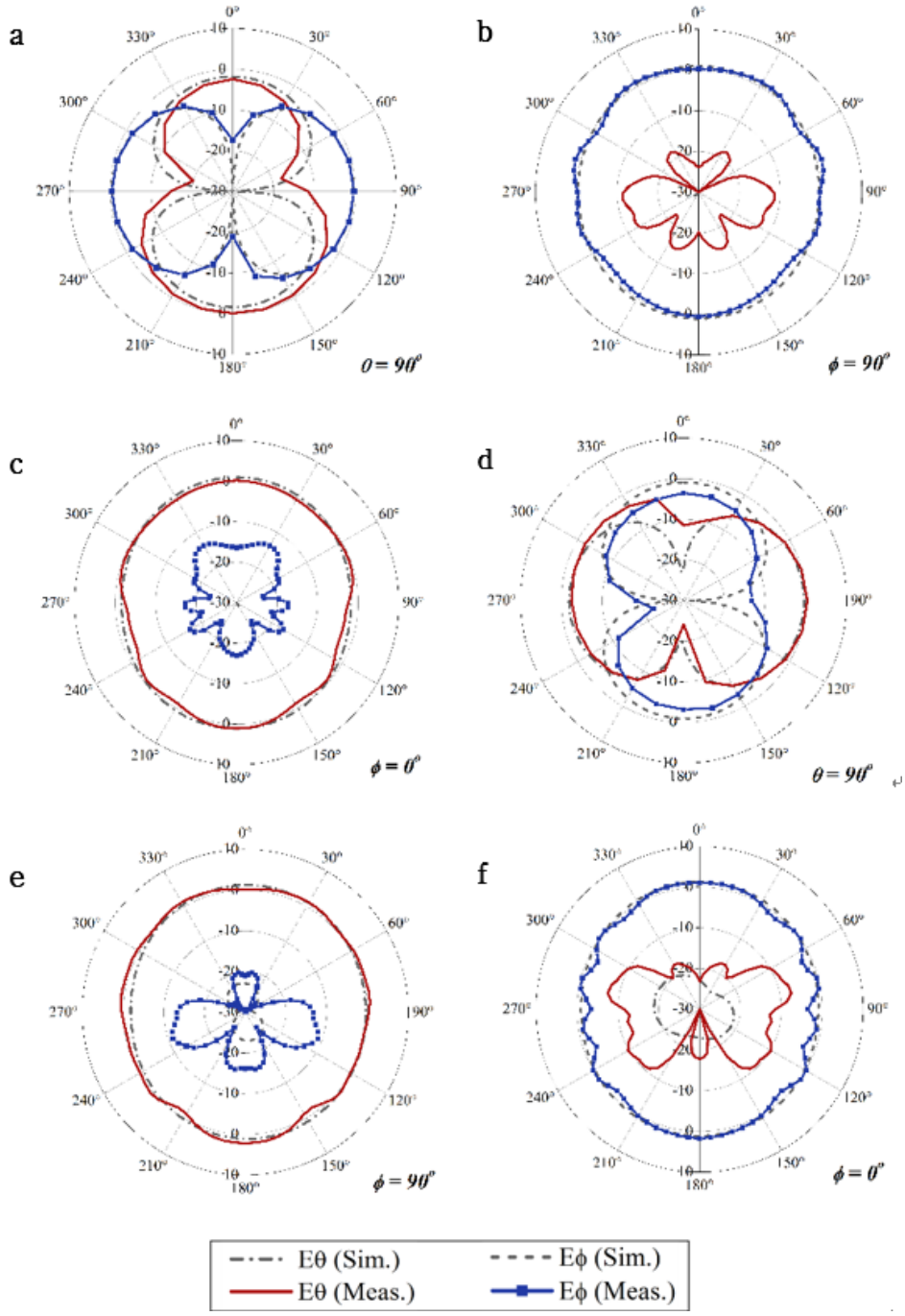

Fig. 2.16. Simulated and measured polar pattern of the proposed antenna. Low band resonance (a) xy−plane. (b) yz−plane. (c) xz−plane. High band resonance (d) xy−plane. (e) yz−plane. (f)xz−plane.

TABLE.2.3

Performance comparisons of the measured results with recent works

Refs	Operation band	Electrical Size (ka)	Gain deviation (dB)		Fractional bandwidth (%)	
[2]	singleband	1.16	6.64		11.0	
[3]	singleband	1.63	5.75		20.8	
[4]	singleband	1.05	5.60		6.9	
[25]	singleband	0.41	5.20		1.8	
This work	dualband	0.47	LB	HB	LB	HB
			4.42	5.76	2.8	1.8

2.5. RF Energy Harvesting Antenna with Wide-band Operation

2.5.1. Motivation

In the previous sections, antennas for energy harvesting operating in a single band and a dual band are proposed. In this section, a wide-band RF energy harvesting antenna that complements the shortcomings of the previous antennas are proposed. The bandwidth-enhanced model is devised to improve the FBW of the single-band energy harvesting antenna. The FBW of the Korean LTE band is 3.4% (865 MHz ~ 890 MHz), but the FBW of the designed single band antenna is 1.8%. The proposed wideband model can cover 4.9% of FBW, and it can fully harvest the ambient EM energy of the targeted cellular band signals

In this section, a bandwidth-enhanced quasi-isotropic antenna using two orthogonally aligned FSRRs is described. The bandwidth is increased by placing each resonance closely with little coupling. The details of the proposed antenna are discussed, and the experimental results show general agreement with simulated results.

2.5.2. Antenna Design

The configuration of the proposed orthogonal folded split ring resonators (OFSRRs) is shown in Fig. 2.17. The OFSRR antenna is composed of two perpendicular FSRR antennas, one on the horizontal (xz) plane with the outer conductor of the substrate and the other on the vertical (yz) plane with the inner conductor. The balanced port is set to directly feed both FSRRs through the via holes that connect the feeding points of the two elements. The horizontal and vertical FSRR elements are designed with identical parameters except the gap (gh, gv) and the parameters optimized with full-wave simulator CST are listed in Table.4.

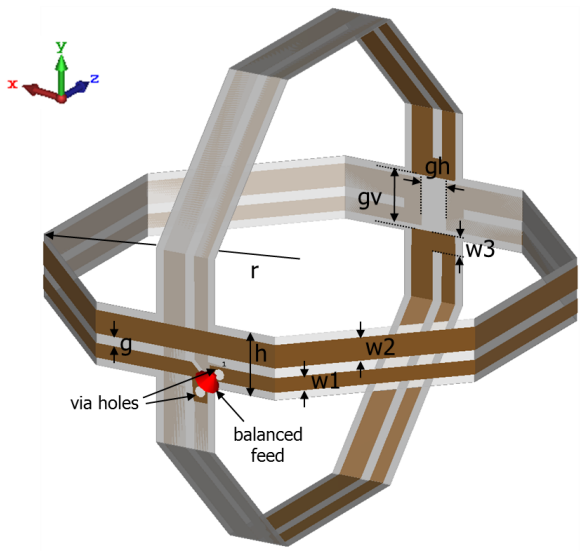

Fig. 2.17. Proposed antenna configuration with the design parameters

TABLE. 2.4
Parameter Values of the Proposed Antenna

Symbol	Quantity	Symbol	Quantity
r	26	h	6.5
w1	1.5	g	1
w2	2.4	gh	2.7
w3	2	gv	5.7

Following the current analysis in [25], the SRR can excite the equivalent electric dipole and the orthogonal magnetic dipole that compensate each pattern null providing a quasi-isotropic radiation pattern. Then the FSRR can be easily matched to 50ohm by applying the folded dipole concept to the SRR structure to make the radiation characteristics better.

The OFSRR is composed of two FSRRs that provides a quasi-isotropic pattern and each resonance is placed close together to enhance the bandwidth. The coupling between two FSRRs can be reduced by implementing them orthogonally, which means that the equivalent electric dipole or magnetic dipole of the horizontal FSRR is orthogonally aligned with the electric dipole or magnetic dipole of the vertical FSRR, respectively. As a result, the proposed OFSRR can achieve the expanded bandwidth providing the quasi-isotropic pattern with electrically small size.

The development figure of the proposed antenna is fabricated using

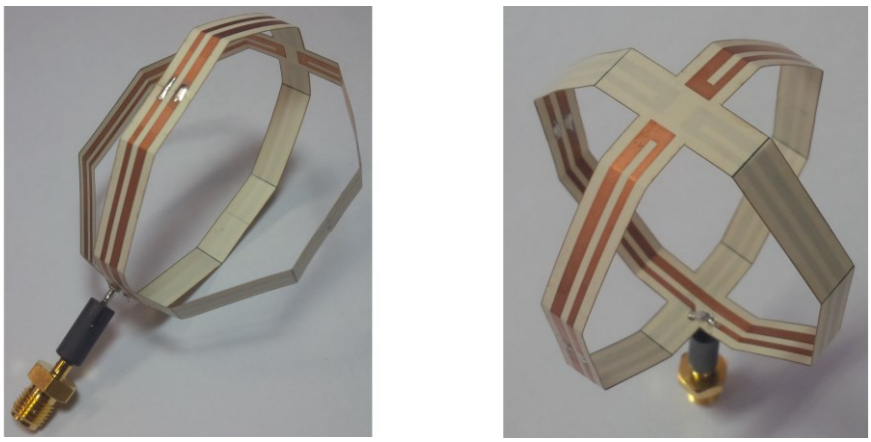

(a) (b)

Fig. 2.18 Photos of fabricated OFSRR antenna. (a) Perspective side view. (b) Perspective top view.

the flexible printed circuit board (FPCB) process on the flexible substrate, Rogers ULTRALAM 3850 with 4 mils thickness, $\tan\delta$=0.002, ε_r=2.9 and half ounce copper. The development figure is then folded and soldered at the side as shown in Fig. 2.18. Ferrite balun is used to keep the current from flowing in the outer conductor of the coaxial cable, which can distort the operation of the antenna.

2.5.3. Result and Discussion

Fig. 2.19(a) shows the reflection coefficient of the proposed antenna with the resonant points of the simulated values at 859 MHz and 886 MHz and the measured values at 868 MHz, 884 MHz. The simulated 10-dB fractional bandwidth is 5.49%, which is from 850 MHz to 898 MHz. The measured 10-dB FBW is about 5% (854-898 MHz) with ka=0.47. In Fig. 2.19 (b), the simulated and measured total radiation efficiency and maximum realized gain are plotted. The measured total radiation efficiency is higher than 76.3% in the bandwidth with two peak values around 94%. The measured maximum realized gain values are in the range of 0.94 to 1.98 dBi and normally higher than the simulated values as the uniformity of the quasi-isotropic simulated pattern is affected by the measurement environments. The simulated and measured results show good agreement despite of small discrepancies due to fabrication tolerances.

The simulated current distributions at each resonance are described in Fig. 2.20 The current distribution shows that the horizontal FSRR resonates only at the first resonance and operates as an equivalent electric dipole in the x-direction and as a magnetic dipole in the minus y-direction resulting in dual polarization on the xz-plane [25]. Fig. 2.20(b) indicates that the vertical FSRR resonates only at the second resonance exciting an electric dipole on the y-axis and magnetic dipole on the x-axis leading to dual polarization on the yz-plane. The electric dipole and the magnetic

dipole at each resonance provide a quasi-isotropic pattern as the omnidirectional patterns of the dipoles are added. In addition, the two electric dipoles or magnetic dipoles are perpendicular to each other, which means there would be little coupling although the two resonances are set close together.

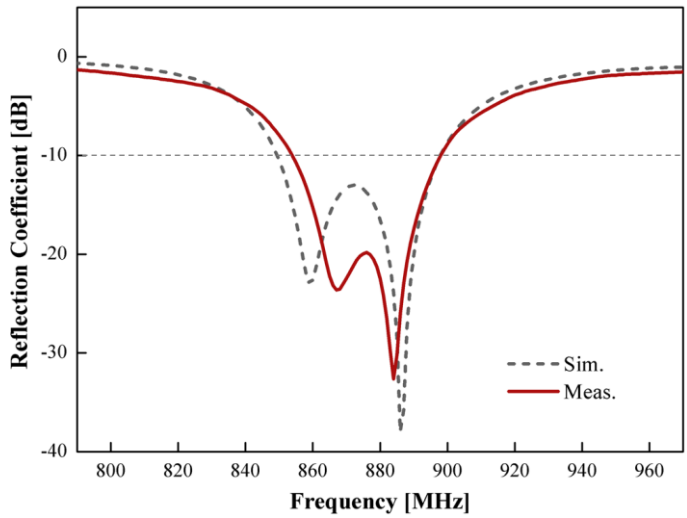

(a)

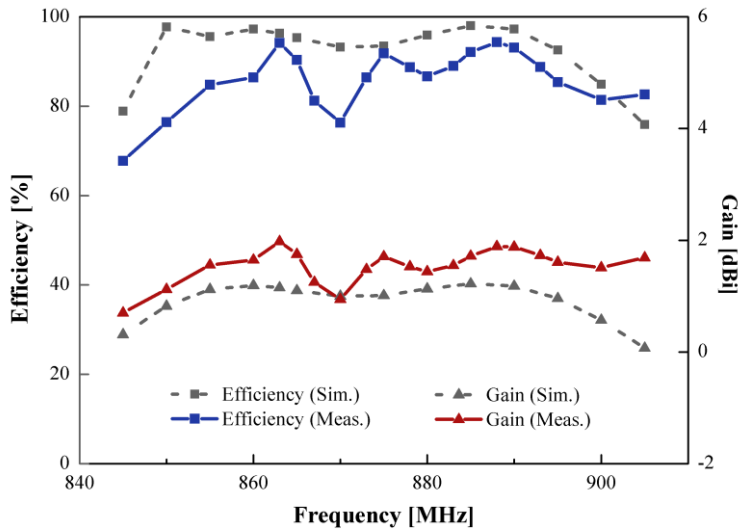

(b)

Fig. 2.19. Simulated and measured results of the OFSRR antenna. (a) Reflection coefficient. (b) Total radiation efficiency and maximum realized gain.

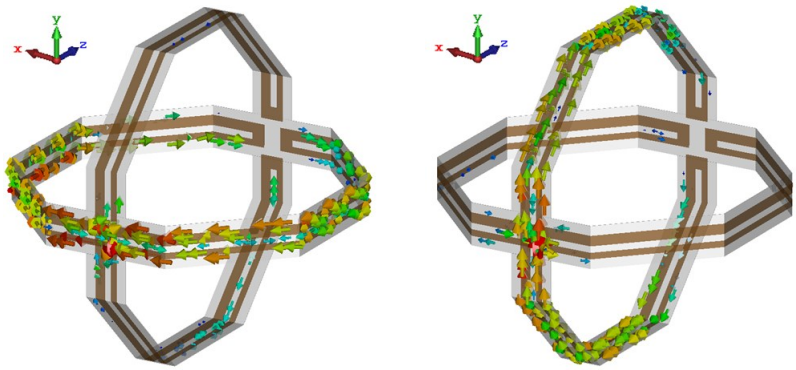

(a) (b)

Fig. 2.20. Simulated current distribution of the proposed OFSRR antenna. (a) At the first resonance (859 MHz). (b) At the second resonance (886 MHz).

Fig. 2.21 presents the polar patterns of the proposed OFSRR antenna at both resonances. The overall patterns are similar to those of the single FSRR antenna in [25], except the stronger cross polarization caused by the other perpendicular element. Although the pattern nulls of the xy-plane are not clear due to strong cross polarization, it can be observed that the equivalent dipoles are aligned with the x-axis or y-axis at both resonances as explained.

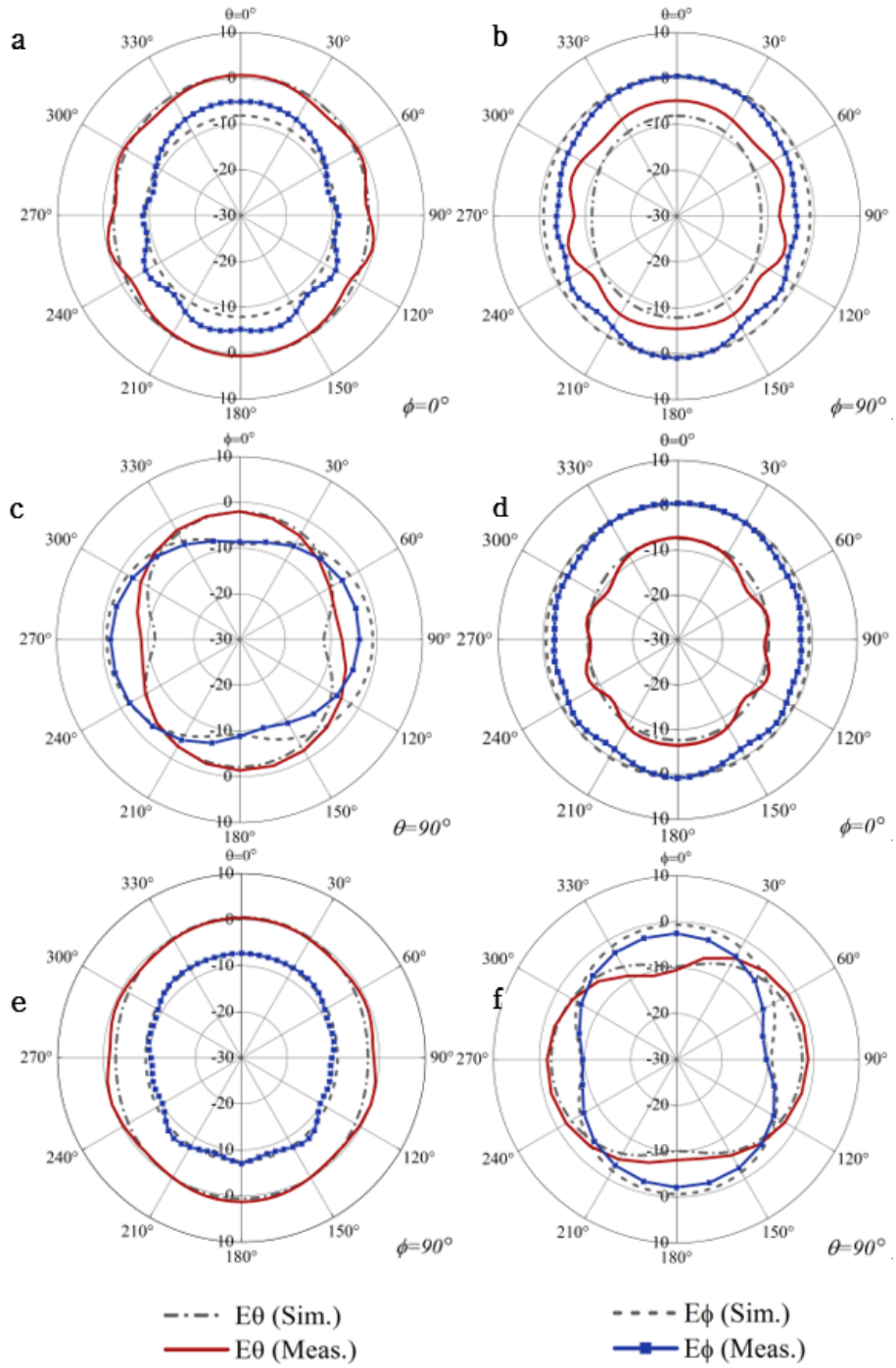

Fig. 2.21. Polar plot results of the proposed antenna. At low band resonances. (a) xz−plane. (b) yz−plane. (c) xy−plane. At high band resonance. (c) xz−plane. (d) yz−plane. (e) xy−plane.

In Fig. 2.22, the measured gain contour graphs are plotted at each resonance. The results show that the maximum realized gain appears around the z−axis where the two omnidirectional patterns of the electric and magnetic dipoles overlapped. The simulated gain deviations are 2.59 dB and 2.99 dB at the lower and higher resonances, and the values are smaller than 3 dB, a theoretical gain deviation limit of the crossed electric and magnetic dipoles [2], since the proposed antenna does not work as ideal point sources. The measured gain deviations are 4.6 dB and 4 dB at each resonance as shown in the Fig. 2.21. The maximum and minimum gain values are 1.98 dBi and −2.62 dBi at 863 MHz and 1.89 and −2.11 dBi at 888 MHz.

The simulated gain deviation versus the operating frequency is described in the figure 2.23. The result indicates that the gain deviation is greater than 2.3300 and less than 2.9127 at the operating frequency (865 MHz ~ 890 MHz). The value of gain deviation becomes lower when the two resonances are overlapped. Referring the reflection coefficient in the Fig. 2.19(a), the two resonances are similarly excited around 870 MHz. Therefore, there exist 4 equivalent dipole moments, consisting of two orthogonal electric and the other two orthogonal magnetic dipole moments. Since the equivalent dipole moments can compensate other's pattern null, the lowest gain deviation is derived around 870 MHz as shown in the Fig. 2.23.

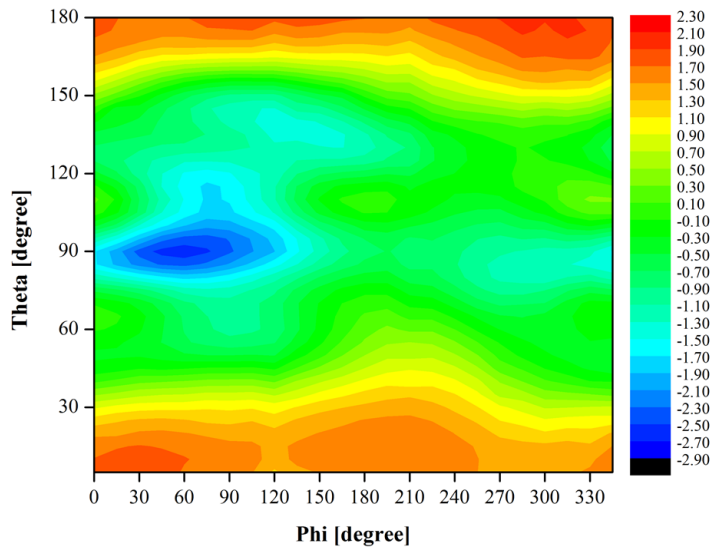

(a)

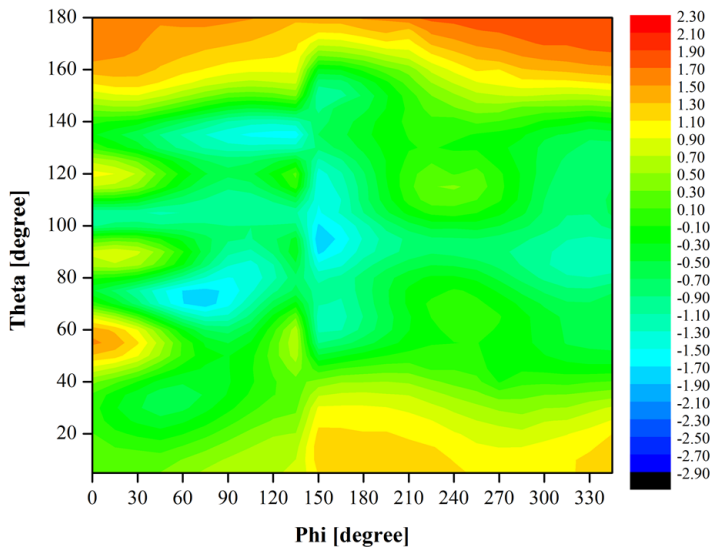

(b)

Fig. 2.22 Measured gain contour graph of the proposed antenna. (a) At the first resonance (863 MHz). (b) At the second resonance (888 MHz).

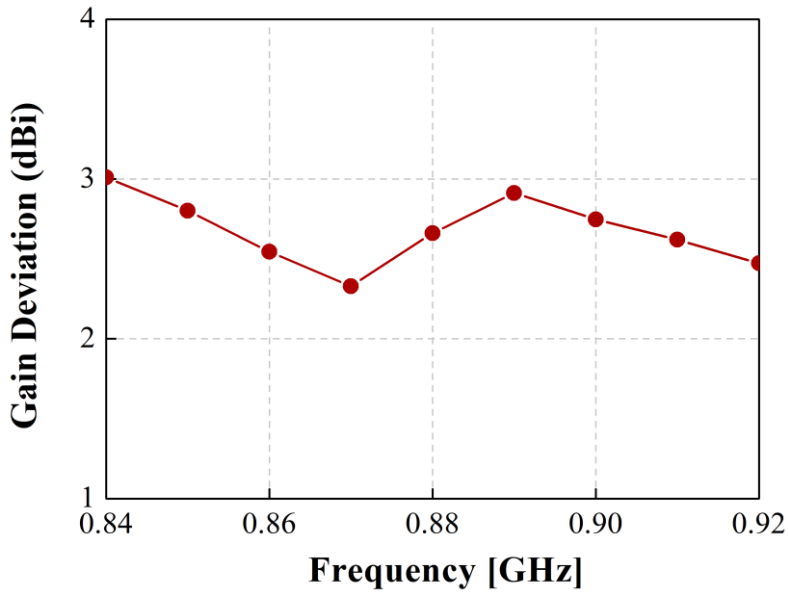

Fig. 2.23 Simulated gain deviation versus operating frequency.

2.6. Conclusion

The lossless SRR is analyzed in terms of radiation resistance by evaluating the magnetic and electric dipole moment with sinusoidal current approximation. Based on the result, the symmetric FSRR is studied by applying the folded dipole analysis that uses the antenna mode and the transmission line mode. The asymmetric FSRR is then analyzed using the current division factor. The input impedance and polar pattern results of the equivalent circuits of the FSRRs generally correspond with the simulation. The calculated and simulated radiation resistances at the fundamental resonances also show good agreement, meaning that the folded dipole structure is successfully applied to the SRR to enhance the radiation properties. This study presents a validation of the operation principle of the FSRR, which provides a quasi-isotropic pattern and a way to improve its radiation characteristics. Therefore, this work can be useful in the design of a compact radio frequency identification (RFID) tag antenna that needs to match the impedance of the tag chip and that is beneficial with quasi-isotropic radiation pattern

The second section demonstrates the dualband quasi-isotropic antenna for the first time. The FSRRs are implemented orthogonally to reduce mutual coupling between the elements at each band. The simulated and measured results generally corresponds. The input resistance and the resonance frequency of the antenna can be easily controlled by changing the design factors of each FSRR element. The

proposed dualband quasi-isotropic antenna with high efficiency, compact size, simple direct feeding can be a prominent candidate in modern wireless communication systems.

The third part describes the bandwidth-enhanced compact quasi-isotropic antenna based on an OFSRR is investigated in this paper. The proposed antenna can simultaneously excite the equivalent electric dipole and the perpendicular magnetic dipole at each resonance providing a quasi-isotropic pattern. The bandwidth is expanded by placing the two resonances close together with little coupling as the equivalent dipoles of each resonance align orthogonally. The concept of the folded structure is applied for direct feeding, and the gap capacitors are used to reduce the electrical size as ka = 0.47. The FBW is 5% with measured resonant frequencies of 868 MHz and 884 MHz, and the measured gain deviation (Δ) values are 4.6 dB and 4dB at each resonance. The proposed antenna operates with noticeable performances compared to other recent works and it is a good candidate for a compact RF energy harvesting antenna covering the Korean downlink band with the most quasi-isotropic pattern.

Based on the proposed antenna, the received power can be calculated. The power density of ambient fields, which are describe in the Fig. 1.4, can be assumed as $1\mu W/cm^2$ at GSM 900 band and $0.3\,\mu W/cm^2$ at Wi-Fi band. Assume there is no conductor and polarization losses. The effective aperture of the isotropic antenna (gain ~1) is approximately $86.7\,cm^2$ and $12.4\,cm^2$ at 900MHz and

2400MHz, respectively. The rectifying efficiency is about 10% when the input power is about −30dBm [28]. Therefore, the received power of the singleband RF EH is about 8.7 μW. If dualband RF EH is applied, 12.4μW can be harvested. Note that the received power can easily varying according to the power density of the ambient fields.

The power consumption of the low power sensors and mobile devices are listed in the Fig. 2. 24 [29]. For example, the small calculator is expected to be powered using RF EH. The smoke detector should be charged for 5 seconds, while the gas detector needs 6 minutes and 52 seconds. The smart watches (41 minutes 40 seconds) and even mobile phones (11 hours 12 minutes) is very hard to be charged by passive R−WPT. Therefore, the transmitting base station needs to be considered in practical scenarios to charge various mobile devices.

Device	small calculator	digital thermometer	smoke detector	wall clock	CO detector	gas meter	LED	lightbulb
P_{DC}	2μW	20μW	55μW	120μW	1.5mW	5.12mW	60mW	1W
Form factor	70x110mm	50x40mm	110x110mm	200x200mm	130x130mm	200x150mm	30x30mm	50x50
A_{eff} **cm**^{2}	77	20	121	400	169	300	9	25
no. USRPs	1	6	2	1	21	38	14300	84487

Device	wristwatch	wearable [49]	hearing aid	mouse	smartwatch	Wi-Fi Flash memory	smartphone
P_{DC}	10μW	60μW	1.5mW	20mW (10μW)	31mW	350mW(210μW)	0.5W
Form factor	40x35mm	19x19mm	20x10mm	115x60mm	50x40mm	32x24mm	50x90mm
A_{eff} **cm**^{2}	14	3.6	2	69	20	7.68	45
no. USRPs	6	69	1774	630 (2)	3349	10^5 (83)	2.35×10^4

Fig. 2.24 The power consumption table for compact sensors and mobile devices [29].

2.6. References

[1] H.F. Mathis, “A short proof that an isotropic antenna is impossible,” Proc. I.R.E. vol. 39, p. 970, 1951.

[2] G. Pan, Y. Li, Z. Zhang, and Z. Feng, "Isotropic radiation from a compact planar antenna using two crossed dipoles,” IEEE Antennas and Wireless Propag. Letters, vol. 11, pp. 1338-1341, 2012.

[3] C. Deng, Y. Li, Z. Zhang, and Z. Feng, "A wideband isotropic radiated planar antenna using sequential rotated L-shaped monopoles,” IEEE Trans. Antennas Propag., vol. 62, no. 3, pp.1461 -1464, Mar. 2014.

[4] Y.-M. Pan, K. W. Leung, and K. Lu, "Compact Quasi-Isotropic dielectric resonator antenna with small ground plane,” IEEE Trans. Antennas Propag., vol. 62, no. 2, pp.577 -585, Feb. 2014.

[5] M. Arrawatia, M. S. Baghini, and G. Kumar, Broadband bent triangular omnidirectional antenna for RF energy harvesting,” IEEE Antennas Wireless Propag. Lett., vol. 15, pp. 36-39, 2016.

[6] L. Liang and S. V. Hum, "A low-profile antenna with quasi-isotropic pattern for UHF RFID applications,” IEEE Antennas Wireless Propag. Lett., vol. 12, pp.210 -213, 2013.

[7] L. Pazin, A. Dyskin and Y. Leviatan, "Quasi-isotropic X-band inverted-F antenna for active RFID tags,” IEEE Antennas Wireless Propag. Lett., vol. 8, pp.27 -29, 2009.

[8] A. Mehdipour, H. Aliakbarian and J. Rashed-Mohassel, "A novel electrically small spherical wire antenna with almost isotropic

radiation pattern," IEEE Antennas Wireless Propag. Lett., vol. 7, pp.396 -399, 2008.

[9] C. A. Balanis, Antenna Theory: Analysis and Design, 3rd ed. Hoboken, NJ, USA: Wiley, 2005, pp.151-161, 232-242

[10] Y. D. Dong and T. Itoh, "Metamaterial-based antennas," Proc. IEEE, vol. 100, no. 7, pp.2271 -2285, 2012.

[11] H. Lee, D. J. Woo, S. Nam, "Compact and bandwidth-enhanced asymmetric coplanar waveguide (ACPW) antenna using CRLH-TL and modified ground plane," IEEE Antennas Wireless Propag. Lett., vol 15, pp 810-813, 2016.

[12] L. Y. Liu, B. Z. Wang, "A broadband and electrically small planar monopole employing metamaterial transmission line," IEEE Antennas Wireless Propag. Lett., vol. 14, pp 1018-1021, 2015.

[13] M.-C. Tang and R. W. Ziolkowski, "A study of low-profile, broadside radiation, efficient, electrically small antennas based on complementary split ring resonators," IEEE Trans. Antennas Propag., vol. 61, no. 9, pp.4419 -4430, Sep. 2013.

[14] I. K. Kim and V. V. Varadan, "Electrically small, millimeter wave dual band meta-resonator antenna," IEEE Trans. Antennas Propag., vol. 58, no. 11, pp.3458 -3463, Nov. 2010.

[15] O. S. Kim, "Low-Q electrically small spherical magnetic dipole antennas," IEEE Trans. Antennas Propag., vol. 58, no. 7, pp. 2210-2217, Jul. 2010.

[16] J. D. Jackson, Classical Electrodynamics. 3rd ed, New York: Wiley, 1975. pp.184-188.

[17] D. J. Griffiths, Introduction to Electrodynamics, 3rd ed. CA: Pearson Benjamin Cummings, 2008, ch. 11.

[18] W. L. Stutzman and G. A. Thiele, Antenna Theory and Design, 2nd ed. New York: Wiley, 1998.

[19] C. W. Harrison, Jr. and R. W. P. King, "Theory of coupled folded antennas" IRE Trans. Antennas Propag., vol. AP-8, pp. 131-135, Mar, 1960.

[20] R. C. Johnson, Ed. Antenna Engineering Handbook, 3rd ed., McGraw-Hill, New York, 1993, ch. 4, ch. 42.

[21] M. Hamid and R. Hamid, "Equivalent circuit of dipole antenna of arbitrary length," IEEE Trans. Antennas Propag., vol. 45, no. 11, pp. 1695-1696, Nov. 1997.

[22] R. Guertler, "Impedance transformation in folded dipoles," Proc. IRE, vol. 38, pp. 1042-1047, Sept. 1950.

[23] K. He, S. X. Gong, F. Gao, "A wideband dual-band Magneto-electric dipole antenna with improved feeding structure" IEEE Antennas Wireless Propag. Lett., vol. 13, pp. 1729-1732, 2014.

[24] M. Li, K. M. Luk, "Wideband magneto-electric dipole antenna for 60-GHz millimeter-wave communications," IEEE Trans. Antennas Propagat., vol. 63, no. 7, pp. 3276-3279, Jul. 2015.

[25] J.-H. Kim and S. Nam, "A compact quasi-isotropic antenna based on folded split ring resonators," IEEE Antennas and Wireless Propag. Lett., 16, pp. 294-297, 2017.

[26] J.-H. Kim and S. Nam, "Design of a compact dualband quasi-isotropic antenna," Electron. Lett., 53, 8, pp.515-516, Apr. 2017.

[27] J. Kim, H. Kim and S. Nam, "Design of a compact quasi-isotropic antenna for RF energy harvesting," 2017 IEEE Wireless Power Transfer Conference (WPTC), Taipei, 2017.

[28] C. R. Valenta and G. D. Durgin, "Harvesting wireless power: survey of energy-harvester conversion efficiency in Far-Field, Wireless Power Transfer Systems," in IEEE Microwave Mag., vol. 15, no. 4, pp. 108-120, June 2014

[29] P. Manuel, et al., "Ambient RF energy harvesting in urban and semi-urban environments," IEEE Trans. Microw. Theory Techn., vol. 61, no. 7, pp. 2715-2726, July 2013.

** Most of the contents of this chapter were published in [25 – 27].

Chapter 3. Radiative-WPT in Lossless Medium

3.1. Motivation

In the previous chapter, research was conducted for the passive R-WPT scenario. However, the power density in the air is not constant and is very weak, so the amount of power that can be actually collected is quite low in the practical situation. In addition, when the incident power is low, the RF to DC rectification efficiency is very deteriorated because the incident voltage is hard to exceed threshold voltage of the rectifier. Therefore, the passive R-WPT described in the previous chapter can be applied to limited applications such as low power sensor nodes or self-sustainable devices.

In order to utilize wireless power transmission in real life, the magnitude of the received power must be secured to some extent. Therefore, in this chapter, a study is conducted to increase the power received from the mobile by actively transmitting wireless power from the base station.

3.2. Previous Research

Over the last decades, WPT, which can charge the batteries of mobile devices without wires, has been developed to improve the convenience of mobile users. There are several WPT technologies, such as inductive coupling, resonant coupling, and microwave power transmission (MPT). Many recent studies on WPT have been

conducted on inductive coupling and resonant coupling, which are based on the use of the near-field, or evanescent field. In contrast, MPT, which is based on the propagating field, has not recently been studied as much, even though MPT can increase the operating range of WPT.

Prior studies on MPT have been conducted on long distance WPT, which is far-field region. However, in the far-field region, PTE is too low to be used in practical environments because of high path loss resulting in scarce field density, which also causes poor rectifying efficiency. As the distance between transmitter and receiver gets closer, there is a possibility that the efficiency can be increased while providing spatial freedom. The PTE will be naturally improved when the operating distance becomes closer, but it is hard to figure out the efficiency using conventional Friis equation since the far-field approximation is not satisfied so that the antenna gain cannot be defined. It is because the wave front of the transmitting EM fields is no longer plane wave, and the field propagating as spherical wave, which becomes radiative near-field region. Several previous studies have been conducted to handle this difficulty as follows.

MPT in Fresnel region is extensively researched in the 1960s using large array antennas [1–11]. Brown conducted many pioneering experiments on MPT for high power applications [1–3]. Glaser proposed a future energy source in which a satellite that harvested solar power in space using huge array antennas transmitted the power to earth via a microwave beam [4]. Goubau

suggested a point-to-point reiterated microwave reply system using cylindrical waves and showed that a Gaussian beam is the approximately optimum transmitting source between two planar apertures, especially in the Fresnel zone, which is also known as the radiative near-field [5–9]. Kay and Borgiotti also described the optimum field of a symmetric transmitting aperture for an ideal receiving aperture in the Fresnel region [10,11]. In 1983, experiments on MPT applying the phased array technique are conducted in space using rockets in Japan [12–14]. Schlesak et al. carried out experiments on a fuel-less airplane powered by a microwave beam using an array of parabolic antennas [15]. The phase-controlled magnetron is designed and employed in airship MPT experiments by Shinohara [16–18]. In addition, studies on RF–DC rectifiers, which are an important component for overall PTE, have been carried out [16,18]. Previous research and experiments on MPT have proved that MPT can operate with high efficiency, even approaching 100%. However, such an MPT system would be too large to apply to practical mobile applications in our daily lives. Although the optimal transmitting field has been found previously, it is derived using an ideal receiving aperture whose shape is circular or rectangular with a symmetric tangential field distribution. Hence, the results cannot be applied to practical mobile antennas [5–11].

Moreover, there have been several methods proposed for efficient WPT via the radiative field in small-scale scenarios: retro-directive arrays (RDAs) and time-reversal (TR) techniques [19–26]. In [19],

an RDA is used in a room scenario to transmit power wirelessly, where the efficiency is defined by the beam width. Time-reversal is a technique that flips the received signal in time to refocus the original field as an incoming wave [23, 24]. Time-reversal in the time domain can be interpreted as a phase-conjugation in the frequency domain, especially for a monochromatic wave. Fink conducted many studies on electromagnetic time-reversal using a cavity-like environment [23, 24]. Time-reversal is also used in open space using pulse waves to improve efficiency [25,26]. However, in most previous works on RDA and time-reversal have provided little information about the efficiency bound of the WPT and the optimal shape of the transmitters within a given area.

In this paper, the PTE bound of the radiative WPT is derived for a given size of transmitting area and distance between the base station (base) and mobile antenna. Moreover, a way to effectively minimize the transmitting area to achieve the target PTE is proposed, especially for practical mobile antennas. The proposed theory can be used for indoor WPT scenarios such as seminar rooms, where base area minimization is an important factor relating to the cost, weight, and complexity of the system.

3.3. Theoretical Approach

3.3.1 Power Transfer Efficiency

First, consider an arbitrary transmitting current as a base surface at position A and a mobile antenna at position B, as shown in Fig. 3.1. Assume both electric and magnetic current flow in the tangential direction on the base surface. Moreover, the mobile antenna is lossless and matched to its load impedance. The PTE is then defined as the receiving power at the load of the mobile antenna over the real input power at the transmitting current, i.e., $\eta = P_{B\_rec}/P_{A\_in}$, which is well known as the transducer gain. Our first goal is to determine the optimal transmitting current distribution for general types of mobile antennas.

As a first step to formulating the radiative WPT scenario, P_{A_in}, which denotes the real input power of the transmitting current, is presented in terms of the radiating EM field from the current at A, which is denoted as $(\mathbf{E_A}, \mathbf{H_A})$. Because it is assumed to be a lossless system, the real input power is equal to the radiating power propagating through the closed surface around A as follows:

$$P_{A\_in} = \frac{1}{4}\oint\left(\mathbf{E_A} \times \mathbf{H_A}^* + \mathbf{E_A}^* \times \mathbf{H_A}\right) \cdot \hat{\mathbf{n}}\, dS, \tag{3.1}$$

where $\hat{\mathbf{n}}$ is the normal vector of the closed surface.

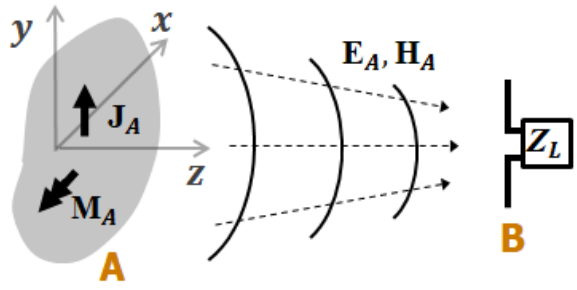

(a)

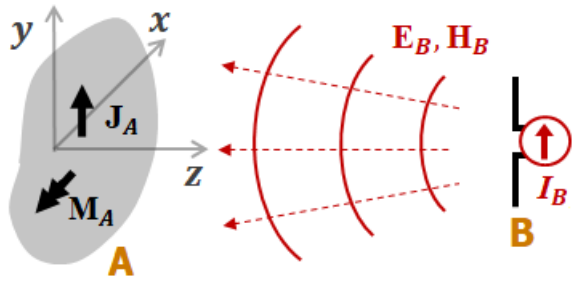

(b)

Fig. 3.1. Configurations for the analysis of radiative WPT. (a) A continuous base current $(\mathbf{J_A}, \mathbf{M_A})$ flowing on a surface emits a field $(\mathbf{E_A}, \mathbf{H_A})$. (b) Reciprocal situation: The mobile antenna transmits propagating EM waves $(\mathbf{E_B}, \mathbf{H_B})$

Because we discuss only the real radiating power, which consists of the propagating wave, the evanescent field is assumed to be negligible in this study. Therefore, the electric and magnetic fields radiated from the base current can be related with the free space wave impedance Z_0.

The numerator of the PTE (P_{B_rec}) can be described in terms of the EM field and current density. Using the open circuit voltage V_{B_oc} of the equivalent circuit model of the receiving mobile antenna, P_{rec_B} can be expressed as

$$P_{B_{rec}} = \frac{|V_{B_{oc}}|^2}{8\ R_L}, \tag{3.2}$$

where R_L is the matched load resistance at the mobile antenna terminal, as shown in Fig. 3.1(a). The open circuit voltage V_{B_oc} is then represented as the radiating field from the current density on the base surface and the source of the mobile antenna ($\mathbf{J_B}, \mathbf{M_B}$) using reaction [27, 28] as follows:

$$V_{B\_oc} = -\ \frac{1}{I_B}\ \int (\ \mathbf{E_A} \cdot \mathbf{J_B} - \mathbf{H_A} \cdot \mathbf{M_B}\ )\ \ dS_B, \tag{3.3}$$

where I_B is the magnitude of the current source at the mobile antenna when it is used as the transmitting antenna, as shown in Fig. 3.(b).

However, it is too complicated to calculate $\mathbf{E_A}$ and $\mathbf{H_A}$, which are the radiated field from the current at A and include the scattered field by the conductor surface of the mobile antenna [27, 28]. Then we can use the reciprocity theorem to replace them using the field radiated by the mobile antenna ($\mathbf{E_B}$, $\mathbf{H_B}$), which is assumed to be known variables if the mobile antenna has been determined. The PTE

is then expressed as follows:

$$\eta = \frac{1}{2R_L\ |I_B|^2}\ \frac{|\int(\ \mathbf{E_B}\cdot\mathbf{J_A}-\mathbf{H_B}\cdot\mathbf{M_A}\ )\ \ dS_A\ |^2}{\oint(\ \mathbf{E_A}\times\mathbf{H_A}^*+\mathbf{E_A}^*\times\mathbf{H_A}\ )\cdot\hat{\mathbf{n}}\ dS}. \tag{3.4}$$

3.3.2. Optimum Transmitting Current

The analysis on PTE in (3.4) is a tedious because it involves solving all the intricate integrals for the EM field vectors from the base current at A ($\mathbf{E_A}$, $\mathbf{H_A}$) as described in previous studies [5–11]. Here, we use a simple idea to determine the denominator of (3.4) for ease of calculation.

Consider two independent scenarios in which the base current at A and the mobile antenna at B radiate respectively, as shown in Figs. 3.1(a) and (b). Because the input power of the two cases can be expressed as radiating power, which is a real value, they can be related with an arbitrary positive real constant value α, i.e., $P_{in\_A} = \alpha \times P_{in\_B}$. Therefore, the denominator of (3.4) can be represented in terms of ($\mathbf{E_B}$, $\mathbf{H_B}$), the radiating field from the mobile antenna at B, with the scaling constant α, so that the optimization problem for the PTE can be easily solved without complex calculations.

The PTE is clearly formulated using the following matrix forms of the field and current density vectors:

$$\psi = \begin{pmatrix} \mathbf{E} \\ \mathbf{H} \end{pmatrix}, \tag{3.5a}$$

$$\rho = \begin{pmatrix} J \\ -M \end{pmatrix}, \tag{3.5b}$$

Replacing the real input power of the mobile antenna at B, (3.4) becomes

$$\eta = \frac{1}{\alpha} \frac{\left|\langle\ {\psi_B}^T, {\rho_A}^\dagger\ \rangle_{S_A}\right|^2}{\left|\langle {\psi_B}^T Z, {\psi_B}^T\ \rangle_S\right|^2}, \tag{3.6}$$

where $\langle f, g \rangle_S$ denotes the inner product of function f and the conjugate of function g on the given surface (i.e., $\int f\ g^* dS$), ${\psi_B}^T$ is the transpose of the matrix representing the fields radiated by the mobile antenna at B (Fig. 3.1(b)) and ${\rho_A}^\dagger$ is the Hermitian of the current distribution on the base surface at A. Matrix Z represents the relationship between the electric field and magnetic field radiated by the mobile antenna, as described in (3.7). Because only the pointing vector normal to the base surfaces is considered, as described in (3.4), matrix Z can be expressed in terms of the inner product of the radial vector of the propagating fields (ψ_B) and the normal vector of the base surface (S_A), i.e., $\hat{\boldsymbol{r}} \cdot \hat{\boldsymbol{n}}$. This indicates the wave impedance of the mobile fields in the normal direction to the base surface currents, as follows:

$$Z = \begin{pmatrix} (\hat{\boldsymbol{r}} \cdot \hat{\boldsymbol{n}})/Z_0 & 0 \\ 0 & (\hat{\boldsymbol{r}} \cdot \hat{\mathbf{n}})\ Z_0 \end{pmatrix}. \tag{3.7}$$

The expression in (3.6) is a well-known form used in optimization

problems for estimation and detection [29,30]. Because matrix Z is positive definite, there exists a nonsingular matrix U such that $Z = UU^{\dagger}$. The maximum value of (3.6) can be obtained using the Cauchy–Schwarz inequality. The resultant optimum transmitting base current on the surfaces is $\rho_{A\_opt} = k(\ \psi_B{}^T\ \mathrm{Z}\ )^{\dagger}$, which is

$$\mathbf{J_{A\_opt}} = k\frac{1}{Z_0}(\hat{\boldsymbol{r}}\cdot\hat{\boldsymbol{n}})\ \ \mathbf{E_B}^{*}, \tag{3.8a}$$

$$\mathbf{M_{A\_opt}} = -kZ_0\ \ (\hat{\boldsymbol{r}}\cdot\hat{\boldsymbol{n}})\ \ \mathbf{H_B}^{*}, \tag{3.8b}$$

where k is a proportional constant. The value of k can be determined using the initial assumption $P_{in\_A} = \alpha \times P_{in\_B}$. The impressed input power at the source A is

$$P_{in\_A} = \ \ \frac{1}{4}\ Re(\int\ \ \mathbf{E_A}\cdot\mathbf{J_A}^{*} + \mathbf{H_A}^{*}\cdot\mathbf{M_A}\ \ dS_A). \tag{3.9}$$

The radiating field ψ_A in (3.9) can be expressed in terms of source current ρ_A using equivalent theorem. Applying the optimal currents of (3.8) to the impressed power of (3.9) to solve the initial condition, the square of the proportional constant is

$$k^2 = \ \ \alpha\frac{\langle\psi_B{}^T Z, \psi_B{}^T\ \rangle_S}{\langle\psi_B{}^T Z, \psi_B{}^T\ \rangle_{S_A}}. \tag{3.10}$$

As a result, the optimal efficiency becomes

$$\eta_{opt} = \frac{\left|\langle \psi_B{}^T Z, \psi_B{}^T \rangle_{S_A}\right|}{\left|\langle \psi_B{}^T Z, \psi_B{}^T \rangle_{S}\right|} . \quad (3.11)$$

Note that the denominator of (3.11) indicates the power radiated by the mobile antenna at B, while the numerator implies the power passing through the region of the given base surface at A (S_A). Therefore, the optimal efficiency can be understood in terms of the radiating field for the mobile antenna and the shape of the base surface.

We can see that the optimum current on the base surface for the mobile antenna in (3.8) is related to conjugation of the tangential fields, which are radiated from the mobile antenna in transmitting mode (Fig. 3.1(b)). Note that the optimum current is the same as the time-reversal current in the time-harmonic case when the scaling factor α is 1 and the propagating vector is aligned to the normal vector ($\hat{\mathbf{r}} \cdot \hat{\mathbf{n}} = 1$) [23-25]. This implies that the maximum PTE can be obtained when the radiating field $(\mathbf{E_B}, \mathbf{H_B})$of the mobile antenna in transmitting mode is reconstructed in the reverse (inward) propagating direction. Therefore, the correlation between the transmitting field from the base and the radiating field of the mobile antenna is an important factor that determines the PTE.

Note that the proposed theory can be applied to general receiving antennas to reveal the shape of the optimum transmitting current and the efficiency bounds, while previous works have generally used symmetric receiving apertures.

3.3.3. Minimizing Transmitting Area

Following the results of the previous section, the optimum base current should flow on the whole of the surface through which the radiating field of the mobile antenna passes to achieve 100% PTE. However, it is impossible to use the entire area as a transmitting base from a practical point of view. Therefore, we must determine the optimal shape of the base current that minimizes the transmitting area, as well as the PTE bound when using the allowable area.

The derivation of (3.11) and its results are valid not only for a closed surface of base but also for an arbitrary unclosed surface. If the denominator in (3.11) is fixed, the numerator then becomes the factor determining the PTE. Following the terms in (3.4) with (3.8), V_{B_oc}, which is a critical factor determining the PTE, is defined as the correlation of the field emitted from the mobile ψ_B and optimal source ρ_{A_opt} on the surface of the base (Fig. 3.1(b)). Therefore, in order to maximize the PTE and use the minimum area of the transmitting surface, it is necessary to use the region with high current flow. To maximize the integral of the numerator over a limited transmitting area, any base current below a certain value should be removed because it contributes less to the receiving power of the mobile antenna. Using this approach, the maximum PTE and the minimum transmission area can be related.

For the sake of better understanding, flow chart in Fig. 3.2 explains the method used to maximize the PTE by decreasing the transmitting area. The process is based on the arrangement of the base and mobile

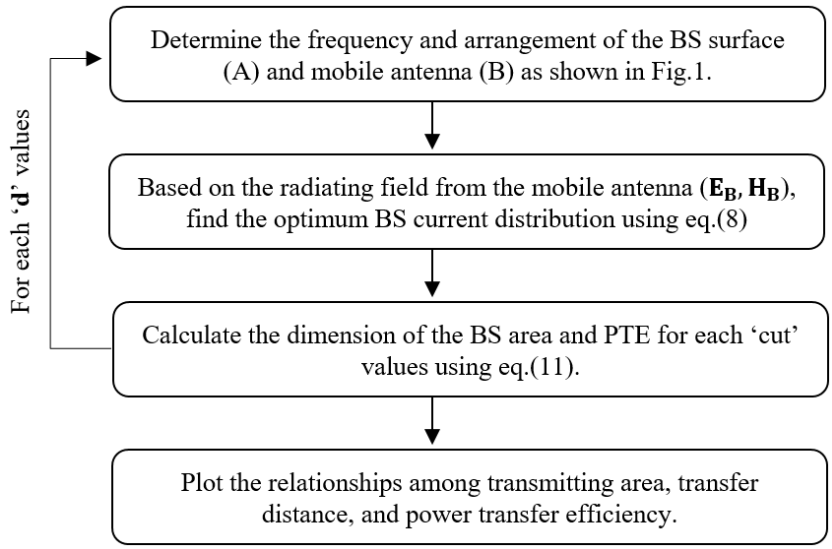

Fig. 3.2. Flow chart of the relationships among the transmitting area, transfer distance, and the PTE.

antenna, the radiating fields of the mobile antenna, and the results of the proposed theory in (3.8) and (3.11). The proper use of the "cut" value can link each parameter.

3.4. Numerical Examples

The proposed theory is then used to analyze three kinds of actual antennas. A 0.5 λ dipole and patch antenna are used as representative examples of mobile antennas, and a high-gain horn antenna is described as a reference for an aperture antenna. Fig. 3.3 shows the configuration of the mobile antenna and transmitting base surface which could also be a spatially distributed or conformal surface. The transmitting current is assumed to be an ideal electric and magnetic current flowing on the tangential surface of the base area. The size of the transmitting surface is $L_{BS} \times L_{BS}$. The base and the mobile antennas are separated by the transfer distance $\mathbf{d}$. The resonance frequency of the mobile antenna is set to 2.4 GHz (the licensed ISM band), but can be scaled arbitrarily for specific applications. The value of $\mathbf{d}$ is set to 0.7 m (5.6 λ), and that of L_{BS} is set to 8 m (64 λ) to observe the shape of the optimal current in the radiative near-field region.

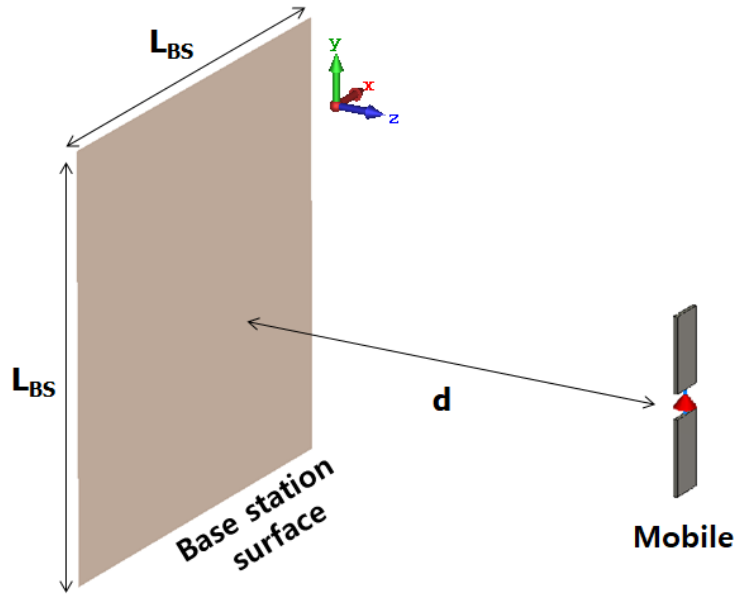

Fig. 3.3. Configuration for the numerical examples. The base surface on which the ideal electric and magnetic current flow on the xy−plane with a size of $L_{BS} \times L_{BS}$. The mobile antenna is placed at a distance d from the base surface.

3.4.1 Dipole Antenna

The first example of a mobile antenna considered in this study is a commonly used 0.5 λ dipole that is aligned in the y−direction. The proposed theory is applied to determine the minimum transmitting area and the efficiency bound of the dipole antenna. The normalized optimal current distribution for the mobile antenna is plotted in Fig. 3.4. The current on the transmitting surface is removed according to a certain percentage (called the "cut") of the maximum value of the square root of the normal pointing vector, as shown in Fig. 3.4. When the cut value is 0%, the entire current on the given transmitting surface is used. The results show that the shape of the optimal transmitting current distribution is not a circle or rectangle, but varies from a jar shape to an oval shape according to either the target efficiency or available transmitting area, which are both related to the cut value. Applying this approach, the target PTE can be obtained using minimized transmitting area or a smaller number of transmitting antennas. As an example, the transmitting area for a cut of 10% is about 1185 λ^2 (18.5 m^2) and the maximum PTE is about 40.5%. When the cut value is 30%, the area of the transmitting surface is about 250 λ^2 (3.9 m^2) and the optimal efficiency is about 29.5%. However, the ability to reproduce an omnidirectional field using only one side of a planar transmitting surface is limited. Because the dipole emits an omnidirectional EM field, the base also needs to reconstruct the radiating field of the dipole antenna in a reverse way. Therefore, the PTE for a dipole antenna is inevitably low.

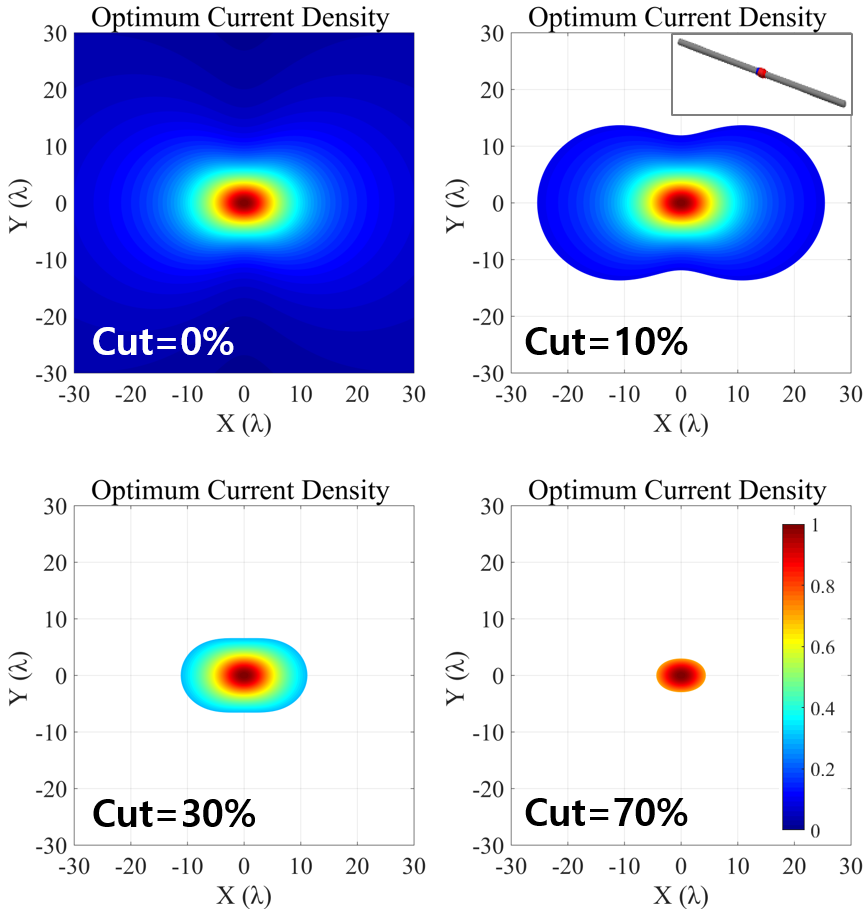

Fig. 3.4. Magnitude of the optimal current density on the base surface when a 0.5 λ dipole is used as a mobile antenna. The current density below a certain value (cut) is removed to minimize the transmitting area.

3.4.2 Patch Antenna

To improve the PTE using a single planar transmitting base surface, a unidirectional patch antenna is designed. The patch antenna is placed on the xy−plane facing the base surface. The lengths of the square patch and square ground plane are about 0.5 λ and 1 λ, respectively. The direct feed is used with an offset in the y−direction resulting in the y−polarized radiating field with gain of 9.4 dBi. The magnitude of the optimal current density is shown in Fig. 3.5(a). Because the designed patch antenna radiates an asymmetric field caused by the diffraction effect of the compact ground plane, the magnitude of the optimal current density is slightly squashed. Compared with the optimal transmitting current of the dipole antenna, the current is concentrated in a smaller region. For a cut value of 10%, the size of the remaining base area is about 330 λ^2 (5.2 m^2) and the maximum PTE is about 85.0%, which is much higher than that of the dipole antenna.

3.4.3 Horn Antenna

A horn antenna is employed to demonstrate the proposed method for a realistic aperture antenna and compare its PTE with the ideal receiving apertures reported in the preceding works. The operating frequency is also set to 2.4 GHz, and the width of the square horn aperture is 1.9 λ. The radiating aperture of the horn antenna is placed at the center of the xy−plane at a distance of d from the base surface, emitting a y−polarized field with gain of 14.8 dBi. Fig. 3.5(b) shows the optimal transmitting current for the horn antenna. As shown in the figure, it can focus more of the field on the smaller base surface. When a cut value of 10% is applied, the existing base area is only 121 λ^2 (1.9 m^2) whereas the maximum efficiency is 90.1%.

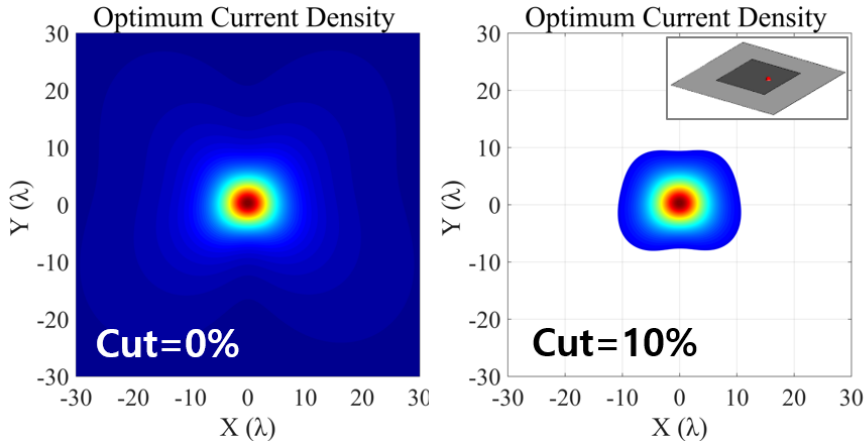

(a)

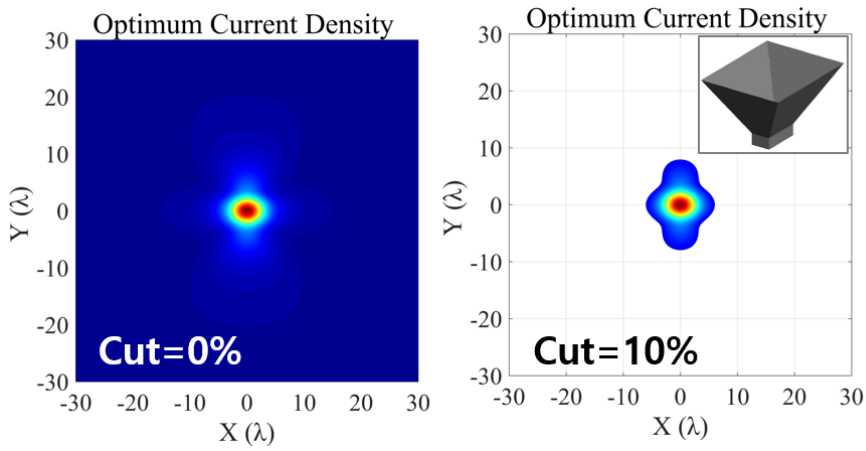

(b)

Fig. 3.5. Normalized magnitude of the optimal current density for unidirectional antennas: (a) Results for a patch. (b) Results for a horn antenna

3.5. Results and Discussion

Using the optimum current distribution and minimum transmitting area, the maximum PTE bounds relative to the size of the transmitting surface and transfer distance are investigated. The efficiency bounds for the three types of mobile antennas are shown in Fig. 3.6(a). The transmitting current on the base surface outside $L_{BS} \times L_{BS}$ (L_{BS} =64 λ) is not considered because it is negligible. The maximum PTE bound for the dipole antenna, which is denoted as a black line, is relatively low (44.2 %) compared with those of the other cases. Because the dipole antenna has an omnidirectional radiation pattern, the maximum PTE cannot exceed 50 % when using only one planar transmitting surface. However, if the base surface are implemented on both sides of the dipole or as a conformal shape, the maximum efficiency bound would be increased. To compare the size of the source area of each antenna, we consider a target PTE of 20 %. As shown in Fig. 3.6(a), a transmitting area of 100 λ^2 (1.57 m^2) would be required to achieve this PTE using a dipole antenna.

In contrast, the PTE result of the patch antenna is highly improved. This is because the patch emits most of its field to a single side, which focuses the radiating field better on the base surface. For the patch antenna, the PTE of 20 % can be achieved by using a transmitting area of 11 λ^2 (0.17 m^2). If the patch antenna is designed to focus more of the field on the base surface, the PTE can be further increased, although the area of the transmitting surface would be the same.

A horn antenna, which is a type of aperture antenna, yields the best performance. The PTE bound of the horn antenna converges to nearly 97.4% for a large size of the transmitting aperture. When the horn antenna is used, a transmitting area of only 4 λ^2 (0.06 m^2) can attain the target PTE.

The PTE bounds reported previously in [8, 11] are compared with the results obtained by the proposed method in Fig. 3.6. The PTE bound results cannot be compared exactly because the definition of the receiving power differs among the previous and current works. For an approximate comparison, a horn antenna is employed as a representative practical aperture antenna with the same size of the ideal receiving apertures used in [8,11]. The results in Fig. 3.6(a) show certain difference of PTE bounds among them, describing the superior performance of the previous works. This difference arises from the previous research [5– 11] defining the receiving power as the power passing through the ideal receiving aperture in which the tangential field is focused as the waist of the Gaussian beam. However, we used the real receiving power at the load of the mobile antennas, which is a more realistic definition because the practical mobile antenna is hard to capture all of the through power. Therefore, the efficiency bounds from the previous methods are unsuitable for mobile antennas, while the proposed theory can provide the practical maximum efficiency bound and shape of the optimal transmitting area. Notably, the proposed theory can also be applied to a general transmitting base surface shape, e.g., the top and bottom surface of

a rectangular room or a conformal shape. In contrast, previous methods have assumed that the receiving aperture is unidirectional or even symmetric.

Here, the PTE data reported in [11] are compared to those obtained in this study only at one point, as shown in Fig. 6. This is because [11] used the assumption that the transmitting aperture and receiving aperture are identical in size, which is also symmetric. Therefore, the PTE bounds in various configurations could not be compared.

Note that the PTE of radiative WPT is not a function of the operating frequency when all of the electrical lengths of the system are fixed. This is because the magnitude of the optimum base current on the given tangential surface is determined solely by the radiating field pattern of the mobile antenna, as described in (3.8). It can also be explained by (3.11) with the configuration of Fig. 3.1(b). Equation (3.11) implies that the maximum PTE is the ratio of the power radiated to the entire space to the power passing through the given base surface. However, it should be noted that when the transfer distance (d) is fixed in meter for a specific WPT scenario, the electrical distance is changed and thereof the efficiency bounds are modified

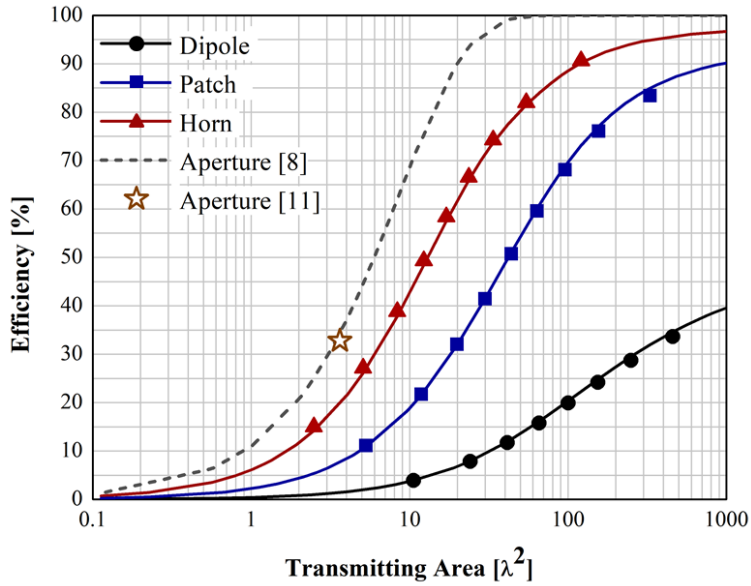

(a)

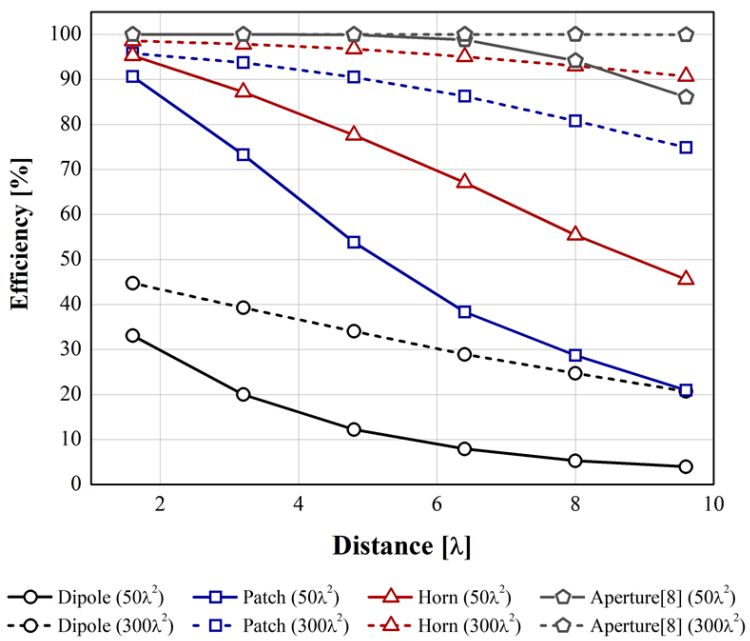

(b)

Fig. 3.6. Comparison of the PTE bounds. Efficiency bound according to the (a) size of the transmitting area, (b) distance between the base surface and the mobile antenna.

To confirm the validity of the proposed theory, a full-wave simulator, FEKO, is used. Because the simulation of a continuous current sheet using full wave EM tools is not available, numerous infinitesimal electric and magnetic dipoles are used to emulate the continuous base current sheet [31, 32]. The distance between each infinitesimal dipole is $0.33\ \lambda$ in the x and y directions. The operating frequency is set to 2.4 GHz. The simulation PTE results are defined as the ratio of the receiving power at the matched load of the mobile antenna to the total input power of the numerous infinitesimal sources. The discrete simulation points are plotted in Fig. 3.6(a) using solid symbols. The maximum relative errors are 2.8%, 1.4%, and 0.5% for the dipole, patch, and horn antenna, respectively. These differences occur because the discrete infinitesimal dipoles cannot realize an exact optimum base current, which is continuous. The theoretical and simulated maximum PTE results are in good agreement, confirming the proposed theoretical efficiency bound for a given area.

Fig. 3.6(b) shows the efficiency bound of the ideal aperture and the three types of antennas in terms of the distance between the base surface and the mobile antennas. The solid and dash lines indicate the cases with the transmitting area of 50 λ^2 and 300 λ^2, respectively. The hollow symbols indicate the calculated points in terms of the transfer distance. The gray lines represent the data of the previous study in [8] and show higher PTE than the real antennas. The graph shows that the patch antenna has better performance than the dipole antenna, although the efficiency of the patch antenna

declines rapidly with distance. It also shows that MPT can achieve a high efficiency (up to 89%) even with a transmitting area of only 50 λ^2 (0.78 m^2) and a compact mobile patch antenna located in the radiative near-field region.

3.6. Conclusion

In this study, for MPT, the bound of the PTE and the optimal shape of the transmitting surface are proposed using simplified analytical steps that can also be applied to the general types of mobile antennas. It is shown that the phase-conjugation of the mobile field is the optimum transmitting current on the base surface. Note that the radiation characteristics of a mobile antenna that can concentrate the field on the base surface are important factors in determining the maximum PTE bound. Following the results, clear differences among the PTE bounds are found for identically sized ideal apertures in the previous works and a practical horn antenna in the current work. Therefore, the proposed theory can provide analytical and physical insight for radiative WPT using practical mobile antennas, which cannot be understood based on previous research. On the other hand, the results show that MPT using a compact mobile antenna, such as a patch antenna, can achieve high PTE when the transfer distance is within the Fresnel region. It is expected that the basic knowledge of this study can assist research on MPT, especially for practical mobile applications in daily life.

3.6. References

[1] W. C. Brown, "Adapting microwave techniques to help solve future energy problems," IEEE Trans. Microw. Theory Tech., vol. MTT-21, no. 12, pp. 753-763, Dec. 1973.

[2] W. C. Brown, "The history of power transmission by radio waves," IEEE Trans. Microwave Theory Tech., vol. 32, pp. 1230-1242, 1984.

[3] W. C. Brown, "Experiments involving a microwave beam to power and position a helicopter," IEEE Trans. Aerosp. Electron. Syst., vol. 5, no. 5, pp. 692-702, 1969.

[4] P. E. Glaser, "Power from the sun: Its future," Science, vol. 162, no. 3856, pp. 857-886, 1968.

[5] G. Goubau and F. Schwering, "On the guided propagation of electromagnetic wave beams," IRE Trans. Antennas Propag., vol. AP-9, pp. 248-256, May 1961.

[6] G. Goubau and P. Schwering, "Free space beam transmission," in Microwave Power Engineering Vol. 1, C. Okress, Ed., New York: Academic Press, 1968, pp. 241-255.

[7] G. Goubau, "Microwave power transmission from an orbiting solar power station." J. Microwave Power, vol. 5, no. 4, pp. 223-231, 1970.

[8] N. Shinohara, "Power without wires," IEEE Microw. Mag., vol. 12, no. 7, pp. S64-S73, Dec. 2011.

[9] N. Shinohara, Wireless Power Transfer Via Radiowaves. NY, USA: Wiley, 2014

[10] A. F. Kay, "Near field gain of aperture antennas," IRE Trans. Antennas Propag., vol. 8, pp. 586-593, Nov. 1961.

[11] G. V. Borgiotti, "Maximum power transfer between two planner aperture in the Fresnel zone," IEEE Trans. Antennas Propag., vol. 14, no. 2, pp. 158-163, Mar. 1966.

[12] H. Matsumoto, "Research on solar power satellite and microwave power transmission in Japan: review and perspectives," IEEE Microw. Mag., vol. 3, no. 4, pp. 36-45, Dec. 2002.

[13] N. Shinohara, "Beam control technologies with a high-efficiency phased array for microwave power transmission in Japan," Proc. IEEE, vol. 101, no. 6, pp. 1448-1463, Jun. 2013.

[14] S. Sasaki, K. Tanaka, and K.-I. Maki, "Microwave power transmission technologies for solar power satellites," Proc. IEEE, vol. 101, no. 6, pp. 1438-1447, Jun. 2013.

[15] J. J. Schlesak, A. Alden, and T. Ohno, "A microwave powered high altitude platform," in IEEE MTT Int. Microw. Symp., New York, 1988, pp. 283-286.

[16] N. Shinohara and H. Matsumoto, "Experimental study of large rectenna array for microwave energy transmission," IEEE Trans. Microw. Theory Tech., vol. 46, no. 3, pp. 261-268, 1998.

[17] N. Shinohara, H. Matsumoto, and K. Hashimoto, "Phase-controlled magnetron development for SPORTS: Space power radio transmission system," URSI Radio Sci. Bull., vol. 77, no. 3, pp. 29-35, 2004.

[18] C. Wang, N. Shinohara, and T. Mitani, "Study on 5.8-GHz single-stage charge pump rectifier for internal wireless system of satellite," IEEE Trans. Microw. Theory Tech., vol. 65, no. 4, pp. 1058-1065, 2017.

[19] Y. Li and V. Jandhyala, "Design of retrodirective antenna arrays for short-range wireless power transmission," IEEE Trans. Antennas Propag., vol. 60, no. 1, pp. 206-211, Jan. 2012.

[20] M. Ettorre, W. A. Alomar, and A. Grbic, "Radiative wireless power transfer system using wideband, wide-angle slot arrays," IEEE Trans. Antennas Propag., vol. 65, no. 6, pp. 2975-2982, Jun. 2017.

[21] M. Ettorre, W. A. Alomar, and A. Grbic, "2-D Van Atta array of wideband, wideangle slots for radiative wireless power transfer systems," IEEE Trans. Antennas Propag., vol. 66, no. 9, pp. 4577-4585, Jun. 2018.

[22] Z. Nie and Y. Yang, "A model independent scheme of adaptive focusing for wireless powering to in-body shifting medical device," IEEE Trans. Antennas Propag., vol. 66, no. 3, pp. 1497-1506, Jan. 2018.

[23] G. Lerosey et al., "Time reversal of electromagnetic waves," Phys. Rev. Lett., vol. 92, no. 19, pp. 193904, May. 2004.

[24] J. de Rosny, G. Lerosey, and M. Fink, "Theory of electromagnetic time-reversal mirrors," IEEE Trans. Antennas Propag., vol. 58, no. 10, pp. 3139-3148, Oct. 2010.

[25] R. Ibrahim et al., "Experiments of time-reversed pulse waves for wireless power transmission in an indoor environment,"

IEEE Trans. Microw. Theory Techn., vol. 64, no. 7, pp. 2159-2170, Jul. 2016.

[26] R. Ibrahim et al., "Novel design for a rectenna to collect pulse waves at 2.4 GHz," IEEE Trans. Microw. Theory Techn., vol. 66, no. 1, pp. 357-365, Jan. 2018.

[27] V. H. Rumsey, "Reaction concept in electromagnetic theory," Phys. Rev., vol. 94, no. 6, pp. 1483-1491, 1954.

[28] R. G. Harrington, Time-Harmonic Electromagnetic Fields. NJ, USA: IEEE Press, 2001.

[29] H. Cox et al. "Robust adaptive beamforming," IEEE Trans. Acoust. Speech Signal Process., vol. 35, pp. 1365-1376, Oct. 1987

[30] J. M. Steele, The Cauchy Schwarz Master Class. NY, USA: Cambridge, 2004.

[31] S. M. Mikki and A. A. Kishk, "Theory and application of infinitesimal dipole models for computational electromagnetics," IEEE Trans. Antennas Propag., vol. 55, no. 5, May 2007.

[32] S. Clauzier, S. M. Mikki, and Y. M. M. Antar, "Design of near-field synthesis arrays through global optimization," IEEE Trans. Antennas Propag., vol. 63, no. 1, pp. 151-165, Jan. 2015.

** Most of the contents of this chapter were published in the article, J.-H. Kim, Y. Lim, and S. Nam, "Efficiency bound of radiative wireless power transmission using practical antennas," IEEE Trans. Antennas Propagat., vol. 67, no. 8, pp. 5750-5755, 2019.

Chapter 4. Active: Radiative-WPT in Lossy Media

4.1. Motivation

In the previous chapter, research was conducted on wireless power transmission in lossless environment, which is ideal scenario. However, there might be lossy medium around the R-WPT system in practical scenarios. In order to extend the previous study to a general situation, a wireless power transmission study in a lossy environment is conducted and the results are described in this chapter.

4.2. Previous Works

The R-WPT in lossy environments has been a topic of interest [1]-[13]. In [1], the authors demonstrated WPT to sensors embedded in concrete blocks, showing the feasibility of a low-cost and reliable health monitoring system for infrastructure. Similarly, the optimal conditions for sending wireless power to sensors buried in concrete are studied using plane wave models in [2]. The authors concluded that the optimal frequency is within the very high frequency (VHF) range for air-concrete structures.

WPT to implantable medical devices (IMDs) used in radiative near-field regions has been demonstrated. In particular, the authors in [3] analytically showed that the optimal frequency is above 1 GHz for tissue layers. They suggested mid-field power transfer for IMD

applications. While [3] considered the electrical properties of the media, [4] considered the effects of a ferrite core incorporated with receivers. The analysis showed that the optimal frequency is maintained in the ultra-high frequency (UHF) range, while increasing the receiving power. Based on a theoretical analysis presented in [3], the optimal transmission current for small implanted receivers is studied in [5]. The authors determined the upper limit of the PTE with respect to the operating frequency. The authors in [6] studied WPT to an implantable conformal antenna in the radiative near-field region. They added a near-field plate to the transmission antenna, proposed in [5], to mitigate the leakage power and improve the PTE

The movement of implanted antennas in the body has been considered to reflect the real conditions [7–10]. In [7, 8], the phase-conjugation (PC) method is used to focus the transmitting power to movable implanted receivers. The transmitter and receiver antennas using magnetic current are designed to reduce tissue losses in [7]. In [8], the proposed phase-conjugation method is compared with the uniform excitation method; the former method gave better field focusing and specific absorption rate (SAR). These studies showed that the PTE of IMDs can be improved in the radiative near-field region. However, there has been little discussion on determining the maximum efficiency with respect to the size of the transmitter. In addition, it is difficult to physically interpret the optimal solutions obtained from the analysis.

References [9–12] reported an optimal design procedure to maximize the PTE using S-parameters. They optimized the excitation of transmission array antennas by solving an eigenvalue problem and demonstrated its usability in various scenarios. Chen *et al.* [12] implanted a planar inverted-F antenna (PIFA) in a head phantom and analyzed the optimal PTE in terms of the number of transmitting arrays and the operating distance. However, no method has been proposed to determine the optimal location and arrangement of the transmission array elements. In addition, the S-parameter of the entire system needs to be measured in each scenario to determine the maximum PTE.

This paper presents an analytical study on the optimal transmission current that can maximize the PTE in lossy media. It is assumed that the power is transferred using RWPT. The theoretical analysis is solved using reciprocity and mathematical substitutions, and the resulting solutions are interpreted. Based on our analysis, the maximum PTE is determined when the area of the transmission currents is limited. Examples with two types of receiving antennas are used to compare the maximum PTE with that obtained in previous research.

4.3. Theoretical Approach

We assume a case wherein a receiving antenna is buried in a homogeneous lossy medium, as shown in Fig. 4.1(a). The permeability of the material is set to the value of free space ($\boldsymbol{\mu_0}$). The transmission currents that send wireless power are assumed to have an arbitrary distribution at a distance of $\boldsymbol{d_{enc}}$ from the receiver antenna. The transmission surface, where electric current ($\mathbf{J_{Tx}}$) and magnetic current ($\mathbf{M_{Tx}}$) exist, can be formed into any shape such as curved or angled; we assumed a planar structure. We define $\boldsymbol{S_{Tx}}$ as the area of the transmitting surface and $\boldsymbol{S_{enc}}$ as the entire enclosed surface that surrounds the receiver including $\boldsymbol{S_{Tx}}$. $\boldsymbol{V_{enc}}$ is the volume inside $\boldsymbol{S_{enc}}$, as shown in Fig. 4.1(a).

Notably, only propagating fields are considered in this study; therefore, this method cannot be applied to regions where the evanescent fields are dominant. In general, the boundaries of the reactive near field and radiative near field are defined as the phase difference originating from the edge and center of the transmitter antenna [13]. On the other hand, for the RWPT, we take the region where the radiating fields dominate the evanescent fields, making this region slightly different from the boundary of the radiative near-field region given in literature. For example, we consider the current flow on the large transmitter antenna as the sum of the equivalent Huygens sources. The reactive evanescent fields will exist around each point source, even if they are added together. This implies that the boundary of the reactive near field is different from that assumed

for RWPT. Therefore, this method can be applied from the part of so-called reactive near-field region to the far-field region.

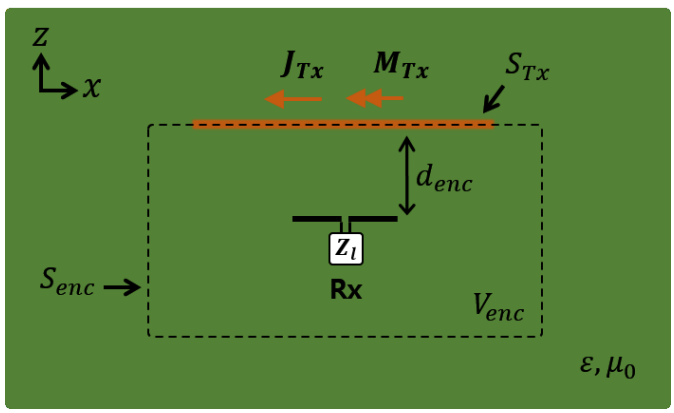

(a)

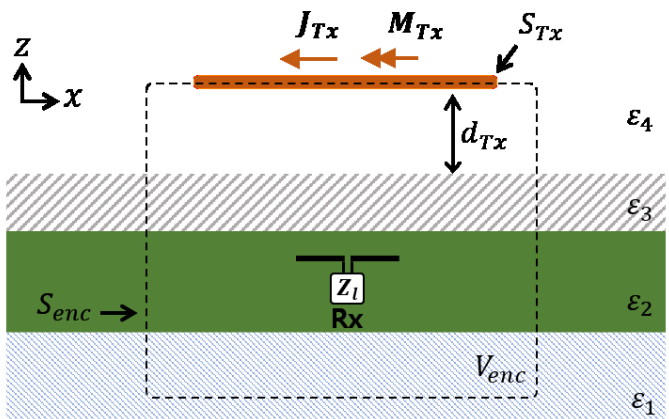

(b)

Fig. 4.1. Scenarios of RWPT in (a) Homogeneous lossy medium. (b) Multi-layer lossy media.

4.3.1 Problem Formulation

The objective of this study is to identify and then find a method to maximize the efficiency of RWPT in a lossy medium. The formulation is based on the analysis methods reported previously [14], except that the effects of lossy media are included to make it more applicable to general scenarios. The PTE, η, is defined as the ratio of the power received at the load of the receiver antenna (P_{rec_Rx}) to the power emitted by the current on the transmitting surface (P_{in_Tx}), which is the concept of operating gain. It can also be assumed that the receiver antenna is matched to the load (Z_l). Therefore, the PTE can be expressed as $\eta = P_{rec\_Rx} / P_{in\_Tx}$, and the objective is to find the maximum value of the PTE in the lossy media and the optimal transmission current distribution (i.e., $\mathbf{J_{Tx}}, \mathbf{M_{Tx}}$) on the transmission surface.

The receiving power, P_{rec_Rx}, in the numerator of the PTE expression can be expressed in terms of the open circuit voltage (V_{oc}) at the receiving antenna and the load resistance (R_l) [15]. V_{oc} can be obtained from the reaction effects of the transmitted field on the current flowing in the receiver antenna. The transmitted field (i.e., $\mathbf{E_{Tx}}, \mathbf{H_{Tx}}$) from the unknown currents should be expressed in complex integral forms. Now, we consider a reciprocal situation where the receiver antenna emits fields, while the transmission currents receive those fields. The reciprocity theorem can be applied, and the problem can be solved more easily:

$$P_{rec\_Rx} = \frac{1}{8\ |I_{Rx}\ |^2 R_l}\ \left|\iint (\ \mathbf{E_{Rx}} \cdot \mathbf{J_{Tx}} - \mathbf{H_{Rx}} \cdot \mathbf{M_{Tx}}\ )\ dS_{Tx}\right|^2 \quad (4.1)$$

where $\mathbf{E_{Rx}}$ and $\mathbf{H_{Rx}}$ are the propagating fields emitted by the receiver antenna, I_{Rx} is the magnitude of the current source of the receiver antenna, and R_l is the resistance of the load.

The transmission power, P_{in_Tx}, can be considered the radiating power from the transmission currents. To avoid using the field quantities (i.e., $\mathbf{E_{Tx}}, \mathbf{H_{Tx}}$) from the unknown transmission currents (i.e., $\mathbf{J_{Tx}}, \mathbf{M_{Tx}}$), a substitution is made to easily solve the expression. The values of the input powers P_{in_Tx} and P_{in_Rx}, when the transmitting surface currents are excited, and the receiver antenna is excited in the reciprocal situation, respectively, are positive real values. Therefore, we can substitute the input powers using a positive real constant α, $P_{in\_Tx} = \alpha\ P_{in\_Rx}$. The input power at the receiver antenna (P_{in_Rx}) can be expressed as the sum of the power dissipated inside the enclosed volume (P_{loss_Venc}) and the power that passes through the enclosed surface (P_{thr_Senc}). However, they cannot be combined into a single term because the volume loss power and the power that passes through have different integral regions. Therefore, we use the substitution once more to combine the two powers with a positive real constant β, yielding $P_{in\_Rx} = (1 + \beta)\ P_{thr\_Senc}$. Thus, we have:

$$P_{in\_Tx} = \frac{\alpha\ (1+\beta)}{2} Re\left\{\oint (\mathbf{E_{Rx}} \times \mathbf{H_{Rx}}^*) \cdot \hat{\mathbf{n}}_{\mathbf{enc}}\ dS_{enc}\ \right\}, \quad (4.2)$$

where $\hat{\mathbf{n}}_{\mathbf{enc}}$ is an outward normal vector from the inside of S_{enc}. By substituting (4.1) and (4.2) into the PTE equation, we obtain the following:

$$\eta = \frac{1}{\alpha\ (1+\beta)^2}\ \frac{|\int(\ \mathbf{E_{Rx}}\cdot\mathbf{J_{Tx}} - \mathbf{H_{Rx}}\cdot\mathbf{M_{Tx}}\ )\ dS_{Tx}|^2}{|Re\{\oint 2(\mathbf{E_{Rx}}\times\mathbf{H_{Rx}}^*)\cdot\hat{\mathbf{n}}_{\mathbf{enc}}\ dS_{enc}\ \}|^2}. \tag{4.3}$$

4.3.2 Maximum Power Transfer Efficiency

To find the optimal solution for (4.3), the relationship between the propagating electric and magnetic fields can be used:

$$\mathbf{E_{Rx}} = Z_w(\mathbf{H_{Rx}}\times\hat{\mathbf{r}}) \tag{4.4a}$$

$$\mathbf{H_{Rx}} = \frac{1}{Z_w}(\hat{\mathbf{r}}\times\mathbf{E_{Rx}}) \tag{4.4b}$$

where $\hat{\mathbf{r}}$ is a unit vector toward the propagation direction, and Z_w is the wave impedance in the lossy material. The fields and currents are expressed in the form of a row matrix as follows:

$$\mathcal{F}_{Rx} = [\ \mathbf{E_{Rx}}, \mathbf{H_{Rx}}\ ], \tag{4.5a}$$

$$\mathcal{S}_{Tx} = [\ \mathbf{J_{Tx}}, -\mathbf{M_{Tx}}]. \tag{4.5b}$$

The inner product is used: $< a, b >_S = \int ab^{\dagger}\, dS$, where $b^{\dagger}$ is the conjugate transpose (Hermitian) of vector b. Equation (4.3) becomes:

$$\eta = \frac{1}{\alpha\ (1+\beta)^2}\ \frac{\left|\langle\ \mathcal{F}_{Rx},\ \mathcal{S}_{Tx}{}^{*}\ \rangle_{S_{Tx}}\right|^2}{\left|\langle \mathcal{F}_{Rx}\ Z,\ \mathcal{F}_{Rx}\rangle_{S_{enc}}\right|^2}, \tag{4.6}$$

where $\mathcal{S}_{Tx}{}^{*}$ is a complex conjugate of the row matrix for the current vectors, and Z is defined as follows:

$$\mathrm{Z} = \begin{bmatrix} Re\left(\frac{1}{Z_w}\right)(\hat{\mathbf{r}}\cdot\hat{\mathbf{n}}_{\mathbf{enc}}) & 0 \\ 0 & Re(Z_w)(\hat{\mathbf{r}}\cdot\hat{\mathbf{n}}_{\mathbf{enc}}) \end{bmatrix}. \tag{4.7}$$

In a lossy media, the wave impedance becomes a complex value. Note that the approach used for free space in [14] cannot be directly applied to find the optimal $\mathcal{S}_{Tx}$ in (4.6), since the matrix Z must be a positive definite to use the Cholesky decomposition as a basic step for the Cauchy–Schwartz inequality [16,17]. The problem can be solved using the forms shown in (4.3), (4.4), and (4.7) and then by applying the modified Cauchy–Schwartz inequality. The resulting optimal solutions of the transmission currents that maximize the PTE are:

$$\mathbf{J}_{\mathbf{Tx\_opt}} = K\ \ Re\left(\frac{1}{Z_w}\right)(\hat{\mathbf{r}}\cdot\hat{\mathbf{n}}_{\mathbf{enc}})\ \ \mathbf{E}_{\mathbf{Rx}}{}^{*}, \tag{4.8a}$$

$$\mathbf{M}_{\mathbf{Tx\_opt}} = -\ K\ \ Re(Z_w)\ \ (\hat{\mathbf{r}}\cdot\hat{\mathbf{n}}_{\mathbf{enc}})\ \ \mathbf{H}_{\mathbf{Rx}}{}^{*}. \tag{4.8b}$$

where K is a real constant value. The physical implications of the optimal solutions in (4.8) are as follows. The optimal currents should be: 1) phase−conjugation of the fields emitted from the receiver antenna, 2) tangential to the transmission surface, and 3) real part of the wave impedance and its inverse. Before calculating the maximum efficiency by substituting (4.8) into (4.6), we must find the constant K. This can be done by equating (4.2) with the expression for the source power in (4.9) [15]:

$$P_{in\_Tx} = -\frac{1}{4}\ Re \int (\ \mathbf{E_{Tx}} \cdot \mathbf{J_{Tx}}^{*} + \mathbf{H_{Tx}}^{*} \cdot \mathbf{M_{Tx}})\ dS_{Tx}. \tag{4.9}$$

By applying the cross product of $\hat{\mathbf{r}}$ into the formula of the equivalent theorem between the magnetic field and the electric current, we obtain:

$$\mathbf{H_{Tx}}^{*} \cdot \mathbf{M_{Tx}} = -\frac{1}{\hat{\mathbf{r}} \cdot \hat{\mathbf{n}}_{\mathbf{Tx}}}\ \{\ \hat{\mathbf{r}} \cdot (\mathbf{J_{Tx}}^{*} \times \mathbf{M_{Tx}})\}, \tag{4.10}$$

where $\hat{\mathbf{n}}_{\mathbf{Tx}}$ is a normal vector from the transmission surface toward the receiver antenna, expressed as $\hat{\mathbf{n}}_{\mathbf{Tx}} = -\hat{\mathbf{n}}_{\mathbf{enc}}$ at S_{Tx}. The results can be obtained as follows:

$$K^2 = \ \alpha\ (1+\beta)\frac{\left|\langle\ \mathcal{F}_{Rx},\ \mathcal{S}_{Tx}^{*}\ \rangle_{S_{Tx}}\right|}{\left|\langle \mathcal{F}_{Rx}\ Z,\ \mathcal{F}_{Rx}\rangle_{S_{enc}}\right|}. \tag{4.11}$$

The optimal PTE is:

$$\eta_{opt} = \frac{1}{(1+\beta)} \frac{\left|\langle\ \mathcal{F}_{Rx},\ \mathcal{S}_{Tx}{}^{*}\ \rangle_{S_{Tx}}\right|}{\left|\langle \mathcal{F}_{Rx}\ \ Z,\ \mathcal{F}_{Rx}\rangle_{S_{enc}}\right|}, \tag{4.12}$$

where $\beta = P_{loss\_Venc} \ / \ P_{thr\_Senc}$. In the case of a highly lossy material, the optimal efficiency is very low because the volume loss power in V_{enc} (P_{loss_Venc}) is typically much greater than the passing-through power (P_{thr_Senc}). Therefore, the value of β becomes quite large. The analysis proposed in this paper can be applied to a planar multi-layer structure, as shown in Fig. 4.1 (b). However, the distance from any Huygens sources, such as d_{Tx} and d_{enc} in Fig. 4.1, should be at least $\lambda/2\pi$. This is because we assumed that the propagating fields are dominant in RWPT [13].

The resulting optimal efficiency in (4.12) is the ratio of the power passing through the specific area (S_{Tx}) to the power passing through the enclosed surface (S_{enc}). The exact value of the maximum PTE can be found by conducting full-wave simulations. We set the input power of the receiving antenna as 1 W and obtain the field quantities of the transmission plane (S_{Tx}). By calculating the Poynting vector, we can determine the power passing through a certain area, which is equivalent to the maximum PTE.

According to (4.12), a certain area where the through power is high becomes important for S_{Tx} to achieve high efficiency. This indicates that areas with a low through power should be avoided so that the transmission area can be efficiently used. By applying this approach, we can determine the maximum PTE when the transmitter is in the

limited area.

4.4. Practical Examples

In this section, the proposed theory is applied to practical scenarios. Representative examples for WPT in lossy media are implantable devices, and this topic has been extensively studied [1]–[12]. In the following examples, an air–skin half space is assumed, as shown in Fig. 4.2. The implanted antenna is inserted at a depth of d_{Rx} below the surface, and the transmitting plane is placed d_{Tx} above the interface. For the electric properties of the skin layers, the Cole–Cole model can be referred [18]. The operating frequency is set to the ISM band of 2.4 GHz, though the theory proposed in this paper can be applied to arbitrary frequency bands.

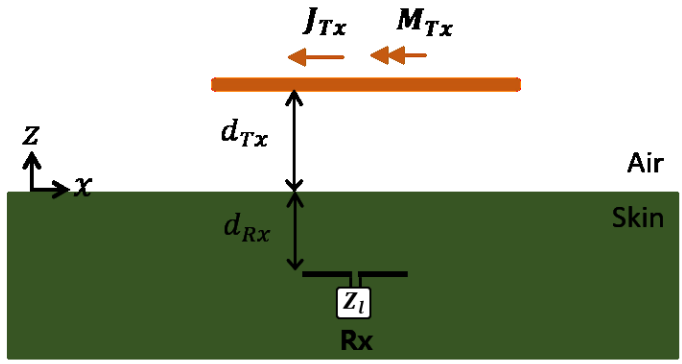

Fig. 4.2. Configuration for the examples of R-WPT.

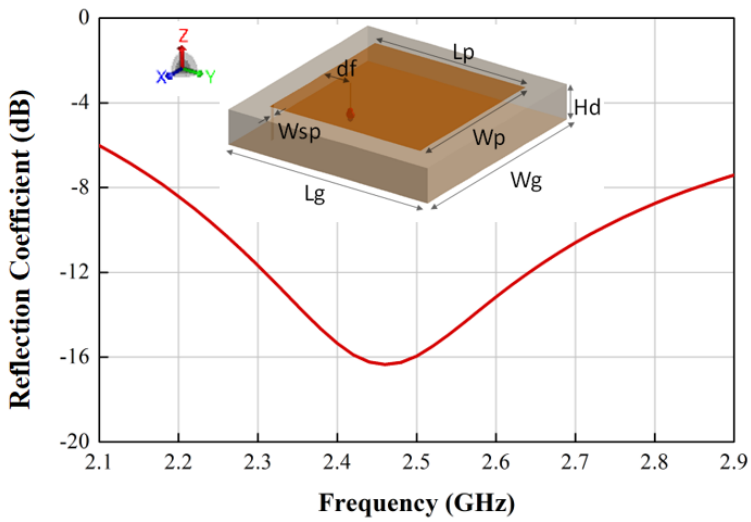

Fig. 4.3. Configuration of the designed PIFA and its reflection coefficient. The PIFA is embedded in the lossy media as shown in Fig. 4.2. $L_g = W_g = 5,\ L_p = W_p = 3.78,\ H_d = 0.8,\ d_f = 0.7, W_{sp} = 0.1$(unit: mm).

4.4.1 Planar Inverted-F Antenna

As an example of a receiving antenna for IMD, a low profile PIFA is designed, as shown in Fig. 4.3 [12], [19], [20]. The exact values of each parameter are given in the figure caption. The substrate of the PIFA antenna is Rogers Duroid 5880, whose ε_r is 2.2 and $tan\delta$ is 0.0009. The size of the designed PIFA is 5×5×0.8 mm^3. The receiving antenna is inserted at a depth of 5 mm from the interface, and the transmission surface is placed 120 mm above the interface. As an application of the theory presented in this paper, the maximum PTE of the PIFA antenna, with respect to the size of the transmission area (S_{Tx}), is obtained. To calculate the maximum PTE, a full−wave FEKO simulation is performed. The PTE can be obtained using the numerical values of the power that passes through the specific area over the power that is supplied to the source. The supplied power includes the volume loss ratio β.

Fig. 4 shows the normalized optimal distributions of the transmission currents. The size of the transmission surface is set as $8\lambda \times 8\lambda$. Fig. 4(a) shows the optimal magnitude of the transmitting electric current density, according to (4.8).

The current vector at the center area is plotted in Fig. 4(b), indicating the optimal polarization of the transmitting antennas. Figs.4(c) and (d) show the magnitude and vector of the optimal magnetic current, respectively. Fig. 4(e) shows the square root of the optimal power density. It can integrate the effects of the electric

and magnetic currents together. To effectively use this area, the power density below a certain value should be discarded. Fig. 4(f) shows the results without values below 20% of the maximum power density. This indicates that the remaining elliptical area has a significant effect on the PTE. Using this approach, we can determine the bound of the PTE under a certain transmission area.

The black solid line in Fig. 5 indicates the maximum efficiency for the PIFA, based on the proposed theory. The red square points in the figure indicates the maximum efficiency, which can be obtained using the methods proposed in previous works with transmission patch arrays [9]–[12]. Considering the total area of the transmission patch array, the maximum PTE is plotted for patch arrays comprising four, five, and nine elements. As shown in Fig. 4.5, the arrangement of the antenna has a significant influence on the efficient use of the transmission area. The maximum PTE of the five-element array is low, as the transmission area is not efficiently used. The proposed optimal PTE is in good agreement with those of previous works. There are differences between the theoretical bounds for patch arrays with four and nine elements, as the rectangular patch array cannot perfectly reproduce the ideal transmission currents. The electric current vector in Fig4.4(b) should be appropriately considered, since it shows the optimal polarization of the transmission array. Notably, the maximum PTE bound can be obtained by conducting a one-time EM simulation of the receiver antenna when it is in the transmitting mode.

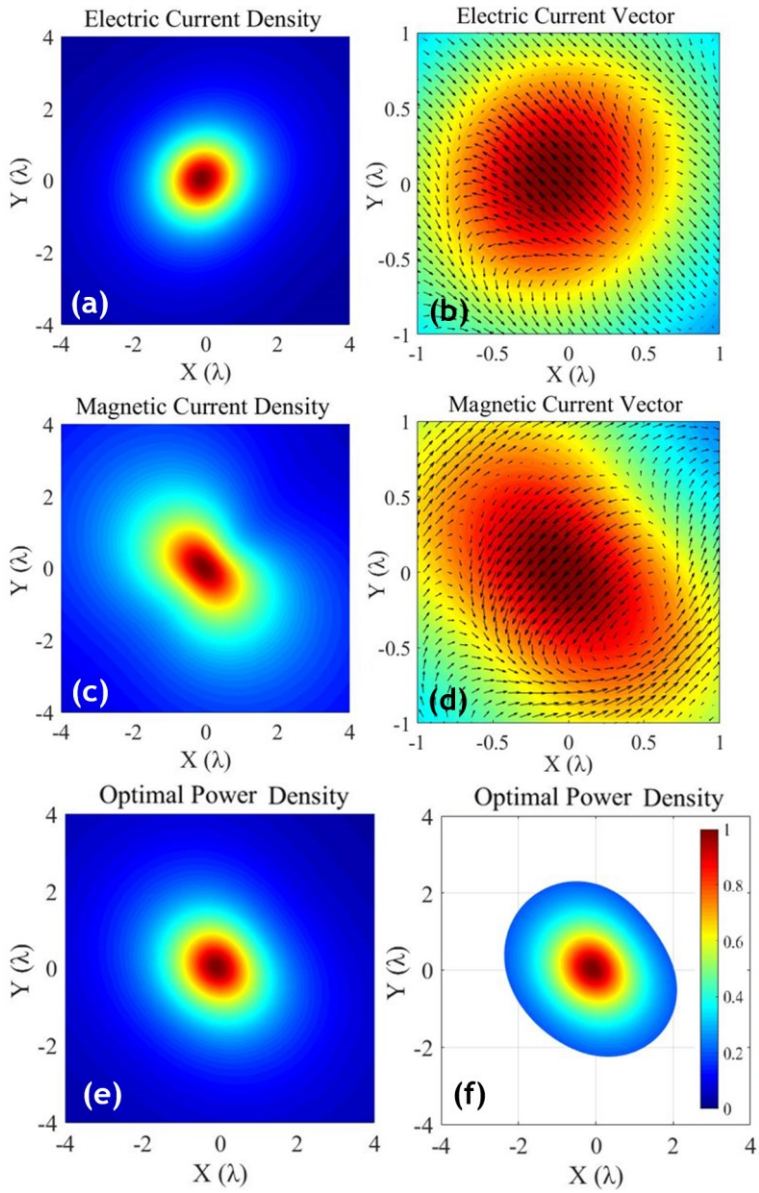

Fig. 4.4. Normalized distributions of the optimal currents and power density for the PIFA. (a) The magnitude and (b) vector plot of the electric current density ($\mathbf{J_{Tx}}$). (c) The magnitude and (d) vector plot of the magnetic current density ($\mathbf{M_{Tx}}$). (e) The magnitude of the square root of the optimal power density. (f) The remaining power density after removing the values less than 20% of the maximum power density.

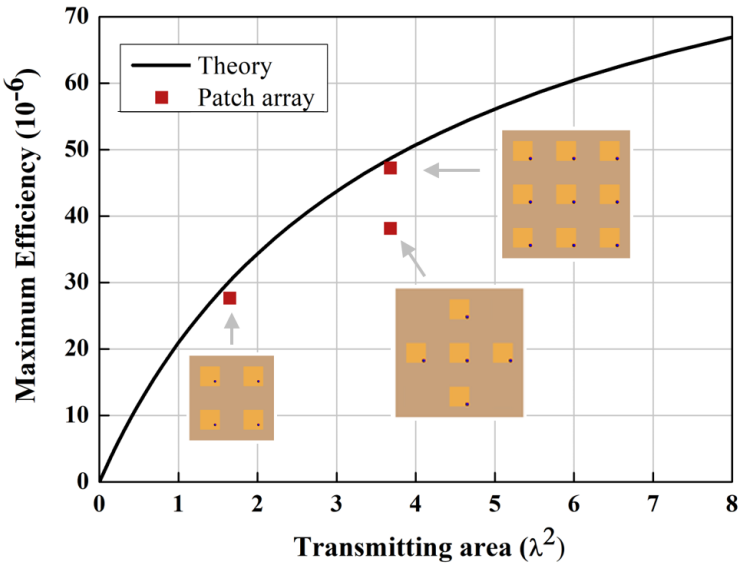

Fig. 4.5. Maximum efficiency bound for the designed PIFA. The side length of the patch is 36.5 mm, the offset distance for feeding is 5 mm, and the space between the patches is 7.3 mm.

4.4.2. Half-Mode Cavity-Backed Antenna

Considering the meaning of (4.12), the maximum PTE can be determined by the power that passes through a certain area. Therefore, the radiating pattern of the receiving antenna is a significant factor in determining the PTE. However, the designed PIFA emits its fields as an omni-directional pattern. Therefore, a unidirectional antenna is designed to enhance the power that passes through the transmission surface. Additionally, an antenna equivalent to a magnetic dipole is introduced to reduce the electrical losses in the tissue media. Considering the requirements, a compact half-mode cavity-backed antenna (HMCBA) is designed to serve as an embedded antenna [21, 22]. Fig. 4.6 shows the configuration of the HMCBA with a reflection coefficient around the target frequency of 2.4 GHz. The HMCBA is considered an equivalent magnetic current between the gap formed by the upper and lower conducting plates. Since a magnetic dipole causes less dielectric power losses than an electric dipole, β in (4.12) can be decreased. This is because the magnetic field is dominant in the reactive near-field region of the HMCBA, while the material loss is due to the electric field near the source [7, 13].

The optimal current and power density distributions suitable for the HMCBA are derived, as shown in Fig. 4.7. Fig. 4.7(a) and (b) show the magnitude and vector of the optimal electric current density, respectively, indicating the appropriate polarization for the transmission array design. There are differences in the magnitude

distribution between the electric current and magnetic current densities. The two parameters can be combined using the power density as shown in Fig. 4.7(e). Fig. 4.7(f) shows the remaining area of the square root of the power density, after removing the area that is below 20% of the maximum optimal power density. This shows that the oval shape elongated in the y−direction plays an important role in the PTE of the HMCBA.

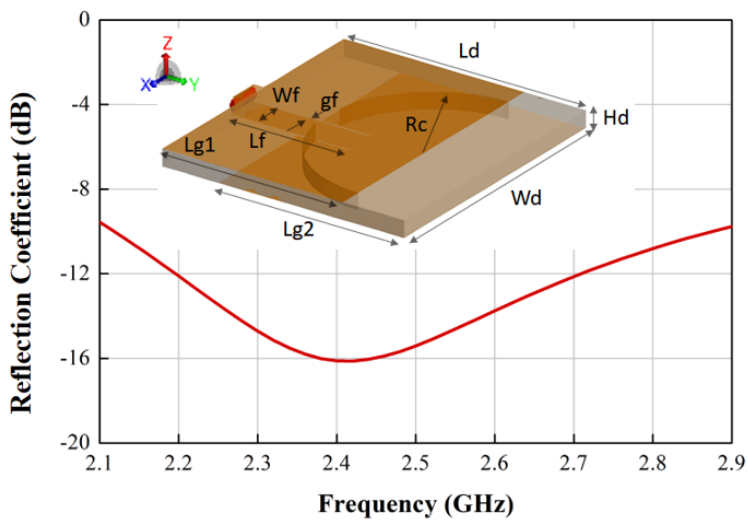

Fig. 4.6. Configuration of the designed HMCBA and its reflection coefficient. The antenna is embedded in the lossy medium as shown in Fig. 2. $L_{g1} = 8.94, L_{g1} = 9.2, L_f = 5.3, L_d = 12.9, W_d = 12, W_f = 1.5, g_f = 0.05, r_c = 5.3, H_d = 0.8$ (unit: mm).

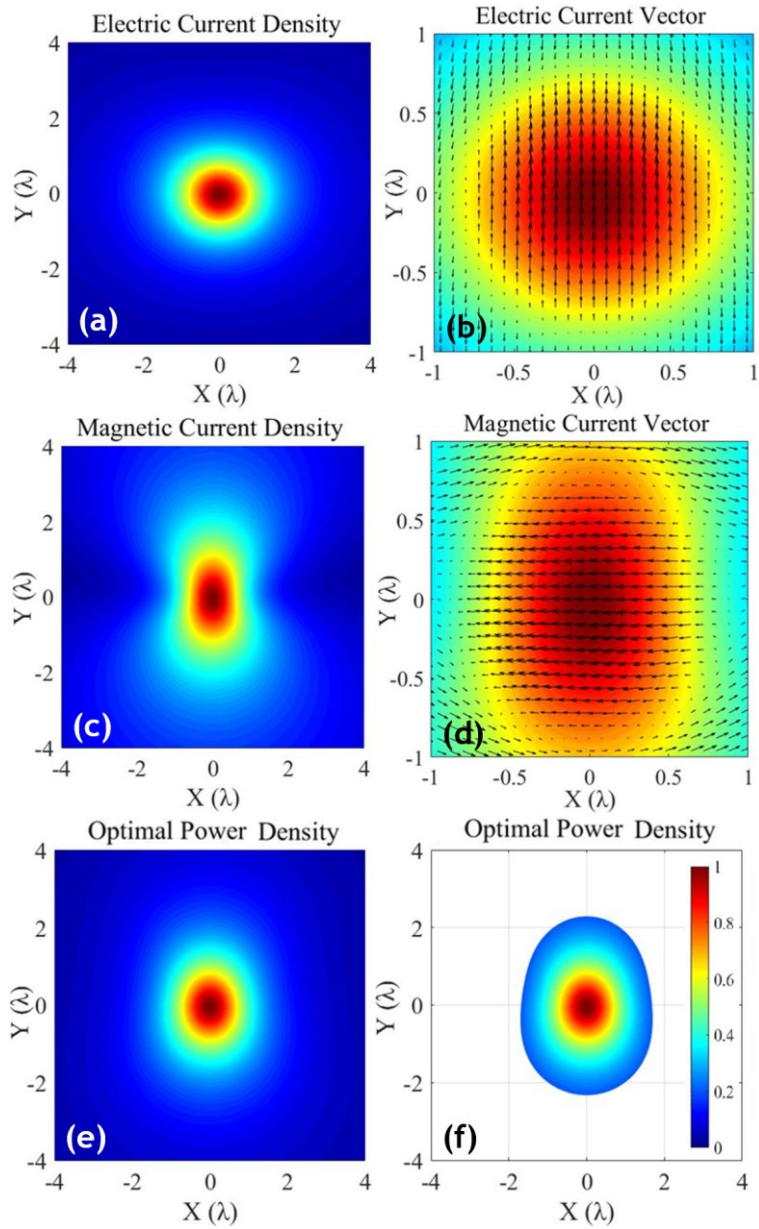

Fig. 4.7. Normalized distributions of the optimal currents and power density for HMCBA. (a) Magnitude and (b) Vector plot of $\mathbf{J_{Tx}}$. (c) Magnitude and (d) Vector plot of $\mathbf{M_{Tx}}$. (e) Magnitude of square root of the optimal power density. (f) The remaining power density after removing the values less than 20% of the maximum value.

In Fig. 4.8, the black dotted line indicates the maximum efficiency bound when using the HMCBA as the receiver antenna. The blue triangles indicate the optimal PTE based on the previous works, which use four, five, and nine elements of y−polarized patch arrays [9]–[12]. The black solid line indicates the efficiency bound of the PIFA, as shown in Fig4. 5. The efficiency decreases when five patch elements are used as the transmission array because of the inefficient sampling of the optimal power density, as shown in Fig. 4.7(e). The red square indicates the PTE for the nine−element patch array, which is polarized in the xy−direction. This shows an efficiency loss due to polarization mismatch, implying that the optimal polarization should be identified and considered, especially for multiple reflected environments. Note that the maximum PTE values for the PIFA and HMCBA are approximately 94×10^{-6} and 431×10^{-6}, respectively, when an infinite xy−plane is used for the transmission currents.

The efficiency bounds for the PIFA and HMCBA are compared in terms of the available size of the transmitter. Using a magnetic antenna with a uni−directional pattern instead of an electric antenna with an omni−directional pattern, we can improve the efficiency by four to five times. This means that the radiation pattern and types of equivalent currents of the receiving antenna play significant roles in practical RWPT scenario in lossy media. However, it should be noted that this comparison is not fair, since the size of the HMCBA is approximately 2.5 times greater than that of the PIFA. Nevertheless,

the two examples are not intended to show the superiority of the HMCBA, but rather to explain how the proposed theory can be used from a practical viewpoint.

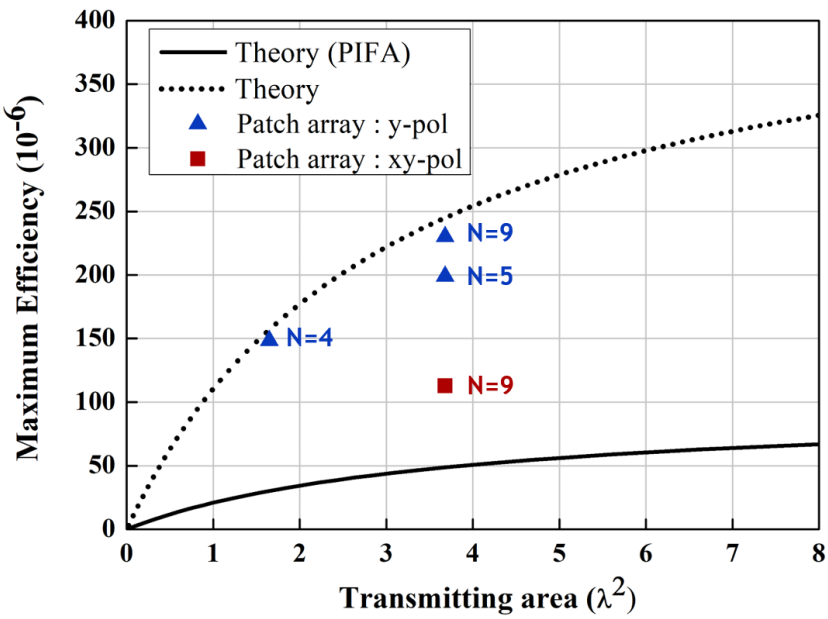

Fig. 4.8 Maximum efficiency bound for the examples.

4.5. Electromagnetic Human Exposure in Radiative WPT System

4.5.1. Motivation

In the previous section, research on wireless power transmission under general conditions is conducted. As a result, the optimum efficiency and current distribution in the case of lossy media are derived. Considering the results derived above and previous research in [9−12, 14], it is concluded that the optimum excitation of the transmitting base station in radiative region is the phase−conjugation when the practical antennas are used. In this chapter, the effects on the human phantom are compared when using phase−conjugation, which is optimum in radiative region, and the broadside (BS) uniform excitation, which is optimum in far−field region.

For radiative WPT applications, safety issue about a human exposure becomes more critical. In radio frequency, the human exposure on PTE wave can have the effect on heating tissues above 10MHz, and stimulate nerve due to contact currents or induced currents below 10MHz [23]. Therefore, it is necessary to study SAR level of a human body in a radiative WPT system in addition to the power transfer performances such as the PTE and the loss in human body. Many research uses specific absorption rate (SAR) as a human exposure evaluation especially in mobile devices [24, 25]. In this section, a study on the human body effect due to PTE field is performed using a homogeneous phantom model. The PTE of the

phase-conjugation WPT system, the power loss in human body, and SAR level are simulated for the typical phase-conjugation WRT system. Also the performances of the phase-conjugation WPT and the broadside Beam forming (BF) WPT systems are compared.

4.5.2. Results and Discussion

PTE using phase-conjugation, which can refocus a wave radiated by a source, is applied to WPT system to improve PTE [27]. We simulated the phase-conjugation system in a room (7.5x8.5x2.6 m^3) operating at 1GHz. Two phase-conjugation (bs), which is composed of 96 half lambda dipole array distributed uniformly over a rectangular ground plane (2x1.4 m^2), are located on top and bottom walls whereas the mobile (mb) receiver is located at the center of the room as shown in Fig4.9. The human body homogenous phantom with ε_r=42, σ=1 S/m, ρ=1000 kg/m^3 located at half lambda apart from the receiver is used to calculate PTE, body loss, and 10g average SAR.

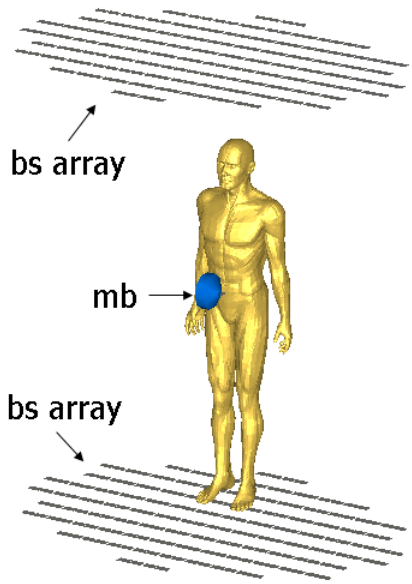

Fig. 4.9. Radiative-WPT scenario with human phantom [27].

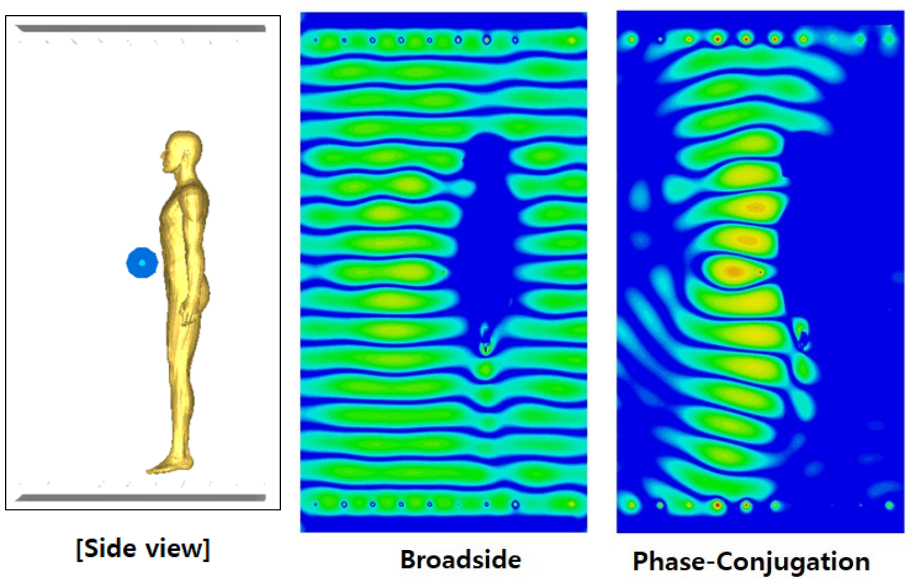

Fig. 4.10. Electric field distribution at the side view [27].

The simulated electric field distribution is plotted in the Fig. 4.10. It shows the side view of the human phantom with base station arrays. Following the figure, it can be seen that there is a clear difference between the broadside array and phase-conjugation array. The field emitted from the base station forms spherical shape, and is more focused on the mobile devices, while decreasing EM effects on the human body.

The simulated 10g average SAR of human phantom for the two arrays are depicted in the Fig. 4.11. It seems that the broadside array results less effects on the human body, however, the SAR is focused on the end of the phantom, such as hands and feet. On the other hand, the SAR of the phase-conjugation array is widely distributed throughout the phantom, so that more power can be transferred to the mobile antenna.

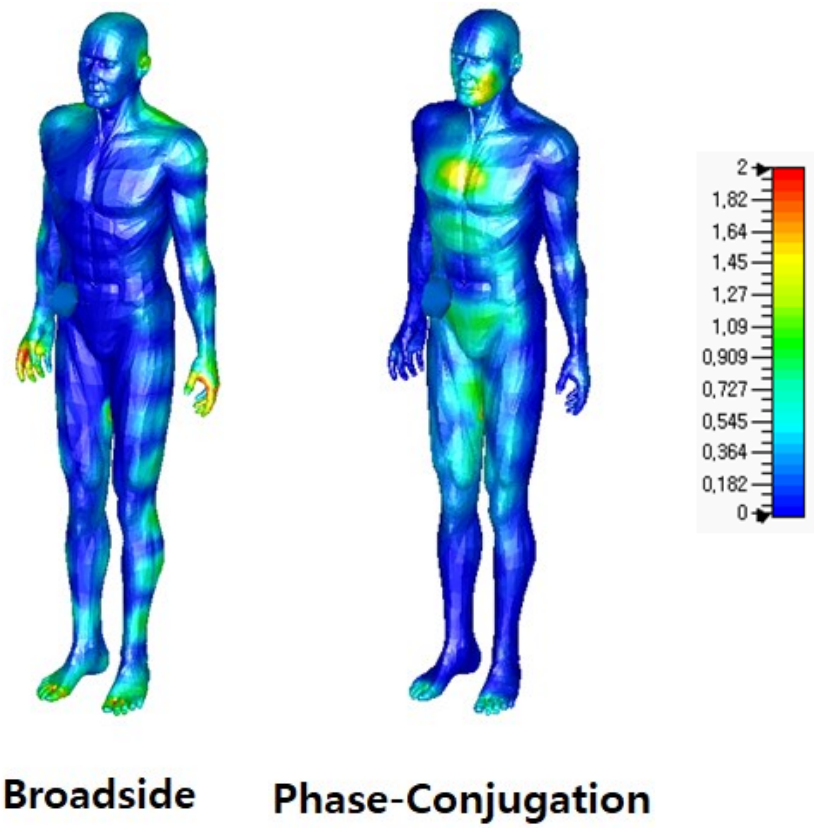

Fig. 4.11. Specific absorption rate (SAR) for the broadside and phase-conjugation array.

The PTE is defined as the received power at the mobile over transmitted power at the phase-conjugation base, which is equivalent to its vice versa in terms of reciprocity. The PTE of WPT system using phase-conjugation with the regular half lambda dipole array is 19.6% and it drops to 11.8% when the human body phantom exists near the receiver. The total power loss in the body phantom is 15.3% of the input power of the phase-conjugation transmitter. When the input power is 1 W, the 10g average SAR level is found as 0.04641 W/kg. According to IEEE or ICNIRP standard, the 10g SAR limit for the body is 2 W/kg. Within the limit value of SAR, the input power can be increased to 43.1 W at which the phase-conjugation WPT system can transfer the power of 5.1 W to the receiver.

The PTE, the power loss in the body, and the SAR level of WPT system with phase-conjugation array is compared with a broadside (BS) beam forming array in Table4.1. The results show that PTE of phase-conjugation array is 46 times higher than base array when the SAR level is maximum of IEEE regulation. In addition, the body loss of phase-conjugation array scheme is 75.7% of base array while more power can be transferred to mobile receiver antenna.

TABLE 4.1

Comparison Table of PC array and base array results

	P_{in} [W]	P_{rec} [W]	PTE [%]	Body loss [W]	SAR [W/kg]
BS array	43.10	5.09	11.83	6.59	2.00
PC array	116.70	0.30	0.26	8.70	2.00

4.6. Conclusion

In this chapter, we present a theoretical analysis of the optimal transmission currents for receivers implanted in lossy media. The results show that a specific part of the field radiating from the receiver antenna must be conjugated to maximize the PTE. Using the analysis, we determined the maximum bound of the PTE when the available transmission area is limited. Two examples are presented to show the usability of the proposed theory and to confirm the fundamental efficiency bounds. Through these examples, we revealed that the radiation characteristics of the receiver antenna play a significant role in determining the PTE. This study can be used to find the efficiency bounds in the design of RWPT systems in lossy materials, and to determine the appropriate location of the transmission antennas, even under complex conditions. We believe that this paper can be useful in further developing RWPT systems in lossy media intended for non-destructive sensing and implantable medical applications.

The electromagnetic effect on the human body phantom in phase-conjugation WPT system is described. The PTE of phase-conjugation WPT system without the human body phantom is 19.6% and it drops to 11.8% when the human body phantom exists near the receiver. The total power loss in the body phantom is 15.3% of the input power of the phase-conjugation transmitter. According to the maximum SAR level of IEEE standard, which is 2 W/kg, receiving power is up to 5.1 W while transmitting power is 43.1 W when

phase-conjugation array is used. In addition, the WPT system using phase-conjugation array is compared with conventional base array in the room. The results describe that the phase-conjugation array shows superior performance than base array in terms of PTE, power loss in body and SAR level.

4.7. References

[1] K. M. Z. Shams and M. Ali, "Wireless power transmission to a buried sensor in concrete," IEEE Sensors J., vol. 7, no. 12, pp. 1573–1577, 2007.

[2] S. Jiang and S. V. Georgakopoulos, "Optimum wireless powering of sensors embedded in concrete," IEEE Trans. Antennas and Propagat., vol. 60, no. 2, pp. 1106–1113, 2012.

[3] A. S. Y. Poon, S. O'Driscoll, and T. H. Meng, "Optimal frequency for wireless power transmission into dispersive tissue," IEEE Trans. Antennas Propagat., vol. 58, no. 5, pp. 1739–1750, 2010.

[4] D. K. Freeman and S. J. Byrnes, "Optimal frequency for wireless power transmission into the body: Efficiency versus received power," IEEE Trans. Antennas Propagat., vol. 67, no. 6, pp. 4073–4083, 2019.

[5] S. Kim, J. S. Ho, and A. S. Y. Poon, "Wireless power transfer to miniature implants: Transmitter optimization," IEEE Trans. Antennas Propagat., vol. 60, no. 10, pp. 4838–4845, Oct. 2012.

[6] R. Das and H. Yoo, "A multiband antenna associating wireless monitoring and nonleaky wireless power transfer system for biomedical implants," IEEE Trans. Microwave Theory Techniques, vol. 65, no. 7, pp. 2485–2495, 2017.

[7] K. Zhang et al., "Near-field wireless power transfer to deep-tissue implants for biomedical applications," IEEE Trans. Antennas Propagat., vol. 68, no. 2, pp. 1098–1106, 2020.

[8] Z. Nie and Y. Yang, "A model independent scheme of adaptive focusing for wireless powering to in-body shifting medical device," IEEE Trans. Antennas Propagat., vol. 66, no. 3, pp. 1497-1506, 2018.

[9] W. Geyi, Foundations of Applied Electrodynamics. USA, NJ, Hoboken: Wiley, 2011.

[10] L. Shan and W. Geyi, "Optimal design of focused antenna arrays," IEEE Trans. Antennas Propagat., vol. 62, no. 11, pp. 5565-5571, 2014.

[11] Z. Duan, L.-J. Xu, S. Gao, and W. Geyi, "Integrated design of wideband omnidirectional antenna and electronic components for wireless capsule endoscopy systems," IEEE Access, vol. 6, pp. 29626-29636, 2018.

[12] Z. Chen, H. Sun, and W. Geyi, "Maximum wireless power transfer to the implantable device in the radiative near-field," IEEE Antennas Wireless Propagat. Lett., pp. 1780-1783, 2017.

[13] C. A. Balanis, Antenna Theory: Analysis and Design, 3rd ed. Wiley, 2005.

[14] J.-H. Kim, Y. Lim, and S. Nam, "Efficiency bound of radiative wireless power transmission using practical antennas," IEEE Trans. Antennas Propagat., vol. 67, no. 8, pp. 5750-5755, 2019.

[15] R. G. Harrington, Time-Harmonic Electromagnetic Fields. NJ, USA: IEEE Press, 2001.

[16] G. Strang, Linear Algebra and its Applications, 4th ed.

Thomson, Brooks/Cole, 2006.

[17] G. H. Golub and C. F. Van Loan, Matrix Computations, 4th ed., MD, Baltimore: The Johns Hopkins Univ. Press, 2013.

[18] S. Gabriel, R. W. Lau, and C. Gabriel, "The dielectric properties of biological tissues: III. Parametric models for the dielectric spectrum of tissues," Phys. Med. Biol., vol. 41, no. 11, p. 2271, 1996.

[19] C. Liu, Y.-X. Guo, H. Sun, and S. Xiao, "Design and safety considerations of an implantable rectenna for far-field wireless power transfer," IEEE Trans. Antennas Propagat., vol. 62, no. 11, pp. 5798-5806, 2014.

[20] M. C. Huynh and W. Stutzman, "Ground plane effects on planar inverted-F antenna (PIFA) performance," in IEEE Proc. Microwaves Antennas Propagation, vol. 150, no. 4, 2003.

[21] H. Dashti and M. H. Neshati, "Development of low-profile patch and semi-circular SIW cavity hybrid antennas," IEEE Trans. Antennas Propagat., vol. 62, no. 9, pp. 4481-4488, 2014.

[22] T. Deckmyn et al., "A novel 60 GHz wideband coupled half-mode/quarter-mode substrate integrated waveguide antenna," IEEE Trans. Antennas Propagat., vol. 65, no. 12, pp. 6915-6926, 2017.

[23] J. Chakarothai, W. Kanako, S. Watanabe, "Evaluation of em absorption characteristics in realistic adult and child models in vicinity of wireless power transfer systems," Proc. Asia-Pac. Int. Symp. Electromagn. Compat., pp. 448-451, 2015.

[24] Mohsen Koohestani, Maxim Zhadobov, Mauro Ettorre, “Design methodology of a printed WPT system for HF−band mid−range applications considering human safety regulations,” IEEE Trans. Microw. Theory Techn, vol.65, Issue. 1, Jan. 2017.

[25] S. I. Kwak, D. cSim, J. H. Kwon, "Design of optimized multilayer PIFA with the EBG structure for SAR reduction in mobile applications,” IEEE Trans. Electromagnetic Compatibility, vol. 53, issue 2, pp. 325−331, 2011.

[26] F. Rachidi, M. Rubinstein, M. Paolone, Electromagnetic Time Reversal: Application to EMC and Power Systems, Hoboken, NJ, USA: Wiley, 2017.

[27] J. Kim, H. Kim and S. Nam, "Electromagnetic exposure on human phantom model in time−reversed wireless power transmission system," 2018 International Symposium on Antennas and Propagation (ISAP), Busan, Korea (South), 2018, pp. 1−2.

** The parts of the contents of this chapter was published in the articles [27]

Chapter 5. Implementation of Optimal Transmitting Current Distribution

5.1. Motivation

Through the study in the previous section, the optimal transmission current distribution for lossless and lossy situations could be identified. The derivation is conducted assuming the transmission current as an ideal current sheet to simplify the theoretical analysis. However, the Ideal Current Sheet should be implemented as a real antenna when the system is realized as WPT system. In this chapter, we described the research on how the ideal current sheet can be implemented as practical antenna arrays.

Research on implementing the ideal current distribution as antenna arrays have been studied and described in the array theory [1-3]. In [1,2], synthesis methods of planar sources are described. They explained representative array synthesis techniques, such as Dolph-Chebyshev array synthesis, or Taylor synthesis, and Bayliss difference pattern synthesis. The techniques are useful when the pattern need to satisfies a specific side-lobe ratio (SLR), to make sum pattern, or difference pattern, respectively. Most of previous works tried to find the array factors that can make the radiation pattern of the designed array similar with the target pattern satisfying the error bound or pattern mask [3,4].

On the other hand, the goal of this research is to figure out the proper way to realize the optimal current distribution as practical

antenna elements. Therefore, it is not easy to apply the methodology of the preceding study. The following study describes the ways to properly implement the optimal transmitting current as real antennas are described

5.2. Theoretical Approach

5.2.1 Radiation Pattern Matching

The proposed study is conducted to find an array structure that can replace the optimal transmitting current sheet. The goal is to design an array that can maximize the total efficiency. Therefore, the equations on the PTE in the previous section is referred as follows:

$$\eta = \frac{1}{2R_L\ |I_{mb}|^2}\ \frac{|\int(\ \mathbf{E_{mb}}\cdot\mathbf{J_{BS}}-\mathbf{H_{mb}}\cdot\mathbf{M_{BS}}\ )\ \ dS_{BS}\ |^2}{\oint(\ \mathbf{E_{BS}}\times\mathbf{H_{BS}}^*+\mathbf{E_{BS}}^*\times\mathbf{H_{BS}}\ )\cdot\hat{\mathbf{n}}\ \ dS}. \qquad (5.1)$$

Assume that the transmitting power at the base area is set as 1 to make the equation simple. The numerator becomes the important factor that decide the PTE. It implies the correlation between the radiating field from the mobile and the transmitting current distribution. Considering reciprocity in the numerator, the dominant factor in terms of the efficiency can be expressed as below:

$$\eta_{field} = \ k\ |\int(\ \mathbf{E_{BS}}\cdot\mathbf{J_{mb}}-\mathbf{H_{BS}}\cdot\mathbf{M_{mb}}\ )\ \ dS_{mb}\ |^2, \qquad (5.2)$$

where k is a constant value. Since the mobile antenna and its

location are already determined, the field, the only factor that decide the efficiency is the field radiated from the base station. Therefore, it can be considered that the alignment of the filed radiated from the ideal optimum current sheet is the core in terms of designing the transmitting base array antenna.

Since the study is conducted in radiative region, the transmitting field should be matched at the radiative region. There are some previous studied that focus or match the target field pattern at the near-field area [5,6]. However, near-field pattern matching requires huge field data if the real antenna is used as unit element.

Referring the other research in [7-10], it is confirmed that the field of the near field fits well when the far-field radiation pattern is matched. In [7,8], an optimization study is conducted to match the radiation pattern of an actual antenna with ideal point source arrays. It optimized the magnitude, phase, and position of the ideal point sources using genetic algorithm (GA). The authors in [9,10] represents spherical mode matching techniques to match the radiation pattern. It is argued that the radiation pattern of an actual antenna can be expressed as the sum of the spherical mode, and the coefficient of a specific spherical mode can be matched using a point source. In particular, after the spherical mode is matched, it is found that the field in the near-field region is also well matched since there exist same spherical modes. Therefore, the following study is conducted on the far-field pattern matching to effectively implement the ideal current sheet as practical antenna elements.

5.2.2. Optimal Excitation Coefficient

There is recent research to be noted in order to implement an optimized transmission array. Referring to the previous study [11-12], the phase-conjugation of the pilot field from the mobile antenna is the way to transmit the radiative power with maximum efficiency. According to the results of this previous study, it can be understood that the optimal excitation coefficient and maximum efficiency are determined when the position of the transmission array is decided. However, little research has been conducted on how to determine the initial position of the transmitting array and the arrangement of the whole array. Therefore, it is judged that to find the position and arrangement of the array that can implement the transmission current distribution most effectively is an important issue.

5.2.3. Thinning of Transmitting Array

In fact, it can be intuitively understood that arranging the antenna very closely in the area can operate as the optimal current sheet. The following results shows the implementation of the ideal current sheet using half lambda regular array with rectangular grid. The half lambda dipole array with ground plane at quarter lambda distance is placed in the oval shaped boundary referring the optimal transmitting current as shown in the Fig. 5.1. The theoretical efficiency bound, which can be obtained from the continuous current sheet, and

simulated results, which are the results using regular dipole array are described in Fig. 5.2. Although the simulated results are degraded at some extent, it shows the clear tendency with the theoretical curve.

However, it is great burden if the transmitting area is completely filled with the antennas. In particular, there need numerous array modules that adjust the magnitude and phase of each element, which require too much cost as well as weight and power loss. Therefore, in this study, the array thinning technique in which the efficiency is maintained to some extent while simplifying the densely arranged regular array. In the following section, array thinning is performed using two different methods. One is an optimization technique using genetic algorithm, and the second is a deterministic approach based on the density tapering, which adjusts the element spacing in proportion to the magnitude of the current.

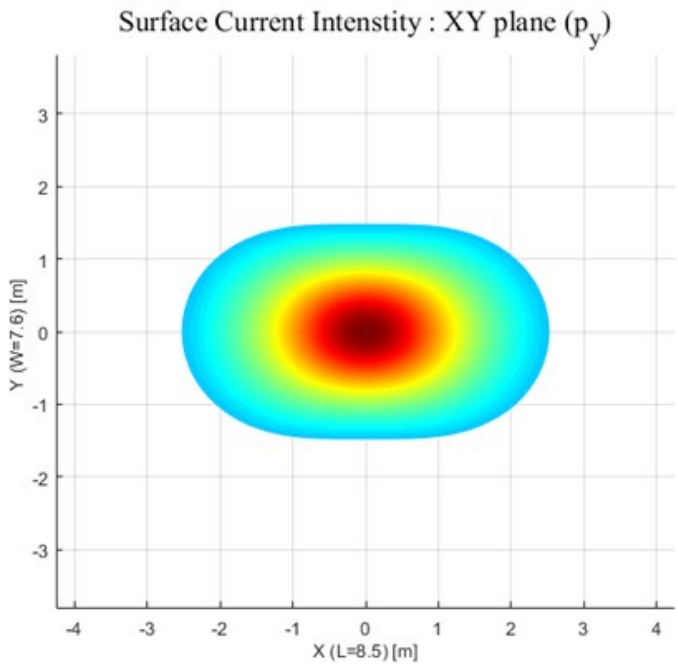

(a)

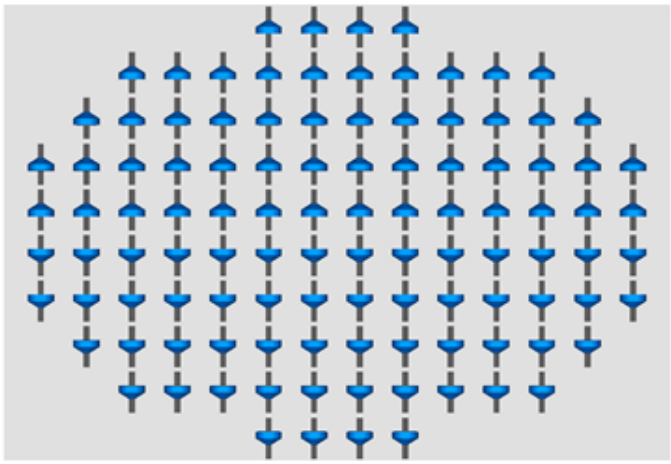

(b)

Fig. 5.1. Optimal transmitter for half-lambda dipole mobile antenna. (a) Shape of optimal transmitting current when the cut value is set as 31%. (b) Regular array following the optimal transmitting array.

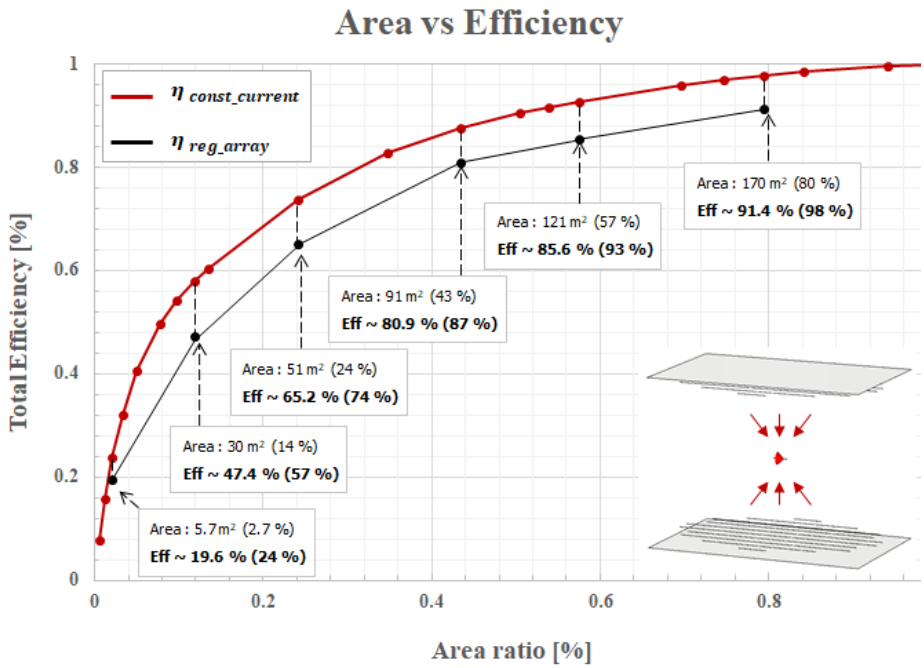

Fig. 5.2. Efficiency bound results for the half lambda dipole antenna array.

5.3. Implementation of the Optimal Current Sheet

5.3.1. Array Thinning using Genetic Algorithm

In this section, the array thinning is conducted considering all three ideas mentioned above. First, we implemented a regular array that densely samples the ideal current distribution. A patch array is used so that only equivalent magnetic current could be considered. In order to sample the current most similarly, the patches are placed as closely as possible, and the gap between the patches (dmin) is set to be 0.5 times the length (Lp) of one side of the patch antenna as shown in Fig. 5.3. A 10x10 arrays are designed as a reference array structure with 500mm distance from the mobile antenna. The resonance frequency of the all antenna are set as 2.45GHz and the Rogers Duroid 5880 with 5mm thickness is used as the substrate.

Second, find the optimized excitation coefficients for all patch elements by applying the theory of the previous study [11,12]. According to the study, the phase-conjugation is the optimal excitation coefficient. Therefore, the voltage applied to each load of the 10x10 base array element is extracted when pilot signal from the mobile antenna is excited. The magnitude of the extracted voltage is applied with reversed phase to satisfy the phase-conjugation condition.

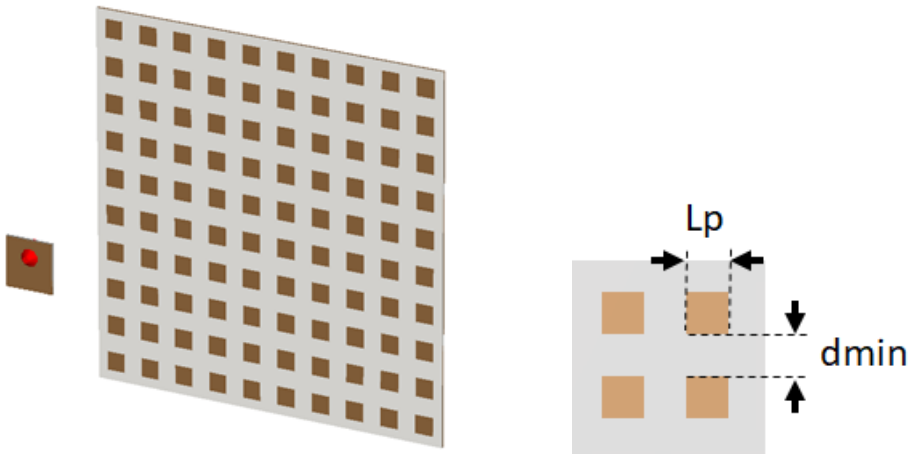

(a) (b)

Fig. 5.3. Configuration of WPT scenario. (a) The reference 10x10 regular array. (b) Description of the the variables in the patch arrays.

Third, the array thinning is conducted to reduce the number of the arrays, while efficiency of the thinned array is expected to be similar with the regular arrays. Before thinning the whole array, the phase conjugation condition is applied. Then, by turning on/off each patch element, the optimal array structure that is most similar to the radiation pattern of the regular array is searched. To find an optimal array structure, genetic algorithm is used referring the previous research [13-15]. The on/off state of the element is expressed as binary sequences of 1 and 0. The binary 'gene' is multiplied to the

magnitude of the excitation coefficient as below:

$$V_{opt} = V_{PC} \times G, \tag{5.3}$$

$$G = [\ 1, 0, 0, 1, \cdots, 1], \tag{5.4}$$

where V_{PC} is the magnitude excitation coefficient of the base array that satisfies the phase-conjugation condition. G is a binary sequence to which the genetic algorithm is applied, and the thinning ratio is determined as the ratio of the number of the on state to the number of the vector elements.

All of the radiation patterns used in the GA are derived by multiplying the active element pattern (AEP) and the array factor (AF). AEP is extracted from the full-wave simulation, CST, when only the central patch is excited while other 99 elements of the regular array are terminated to 50ohm load. The reference pattern (P_{ref}) of the regular array is calculated considering the excitation coefficient, which is phase-conjugation, of the 10x10 patch, and the pattern of the thinned array (P_{GA}) is calculated excluding the excitation coefficient of the off element. The cost function of GA is expressed as the relative error of the reference pattern at phi=0 and phi=90 plane, as shown below:

$$Y = \frac{P_{ref_0} - P_{GA_0}}{P_{ref_0}} + \frac{P_{ref_{90}} - P_{GA_{90}}}{P_{ref_{90}}}. \tag{5.5}$$

The radiation pattern is normalized in the optimization code to effectively perform the optimization.

5.3.2. Results and Discussions

The thinned array by applying GA algorithm to a 10x10 regular array is conducted with 81% of thinning ratio to the regular array. Genetic algorithm is performed using built in functions in MATLAB. The resultant cost function in (5.3) is 0.1370. The optimized configuration of the thinned array is shown in the Fig. 5.4. It can be seen that the elements in the periphery are removed compared to the regular array. The regular array is compared in terms of the same number, and same array size with the thinned array.

The efficiency is extracted for each array structures using full-wave simulation, CST. Reciprocal situation is considered to simply check the efficiency. The efficiency is defined as a ratio of the power received at 50ohm termination of the base array to the transmitting power at the mobile antenna. Following the Fig. 5.4, it can be shown that the efficiency of the thinned array is improved compared to the same number of regular array.

On the other hand, the efficiency is dropped compared to the same size of the regular array, which might be originated from the pattern errors. Indeed, the radiation pattern of the regular array and the thinned array in the Fig. 5.5 show some differences. Note that the radiation patterns are plotted in linear scale.

The results are well matched with expectations. The thinned array reduced the number of elements by 19% compared to using the regular array, while the relative efficiency decreased by about 7%. Additional comparison is conducted with same number of regular arrays (9x9) to propose the effects of thinning. It is shown that the efficiency of the thinned array is increased by about 4.7% compared to that of the regular array, while the number of patch elements is the same.

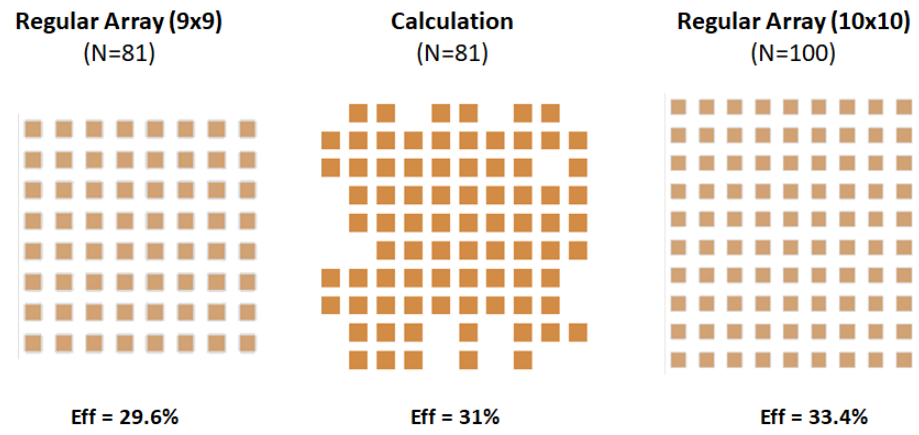

Fig. 5.4. Configuration and efficiency of the regular arrays and resultant thinned array.

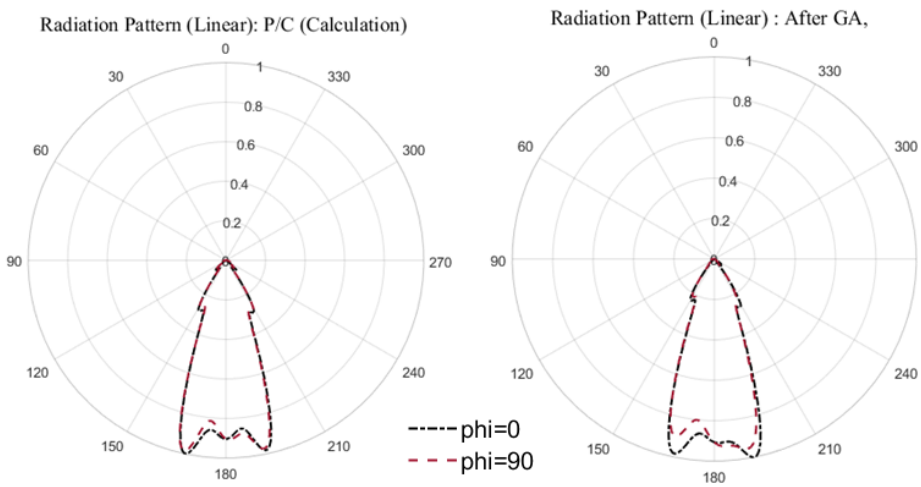

Fig. 5.5. Radiation pattern of the 10x10 regular array and the thinned array.

5.3.3. Array Thinning using Density Tapering

Majority of studies on array thinning is conducted based on optimization techniques to reduce the number of arrays. On the other hand, when the number of arrays is very large, such as antennas for satellite communications, it is important to feed the antennas of the array by identical magnitude. In terms of the uniform magnitude of the array, the density tapering (DT) technique is proposed to sample the distribution of the optimal current distribution [2,16,17].

DT is a method of arranging elements of the array such that the integral value of the current distribution over a distance is constant. The basic concept of the DT is described in Fig. 5.6. In the case of the previous research in which the density taper is applied, the phase variation is zero or relatively small [16−18]. The issue on the rapid phase variation and approximation condition is described in [16]. On the other hand, the phase variation of the optimum current distribution is rapid as shown in the Fig. 5.6(b), since the optimum current is defined in the radiative region, Therefore, it is concluded that direct adaptation of DT is not appropriate considering the phase variation of the proposed optimum current distribution.

However, the basic concept of DT that place the antenna according to the size of the current is quite intuitive, so DT can still be applied to design a thinned array with modification. The sampling location is not decided by the accumulated current density as described in the previous research, but gradually increased from the spot where the current distribution is large. The distance between the center points

of the adjacent patch element (d_{array}) is set by the following relationship.

$$d_{array} = d_{min,i} + L_p, \tag{5.4}$$

$$d_{min,i} = d_{min} + \left(i \times \Delta_{d_{min}}\right), \tag{5.5}$$

where L_p is the length of the patch antenna and d_{min} is the distance between the edge of adjacent patch antennas. The distance between the patches is designed to increase evenly by $\Delta_{d_{min}}$ as it moves away from the center.

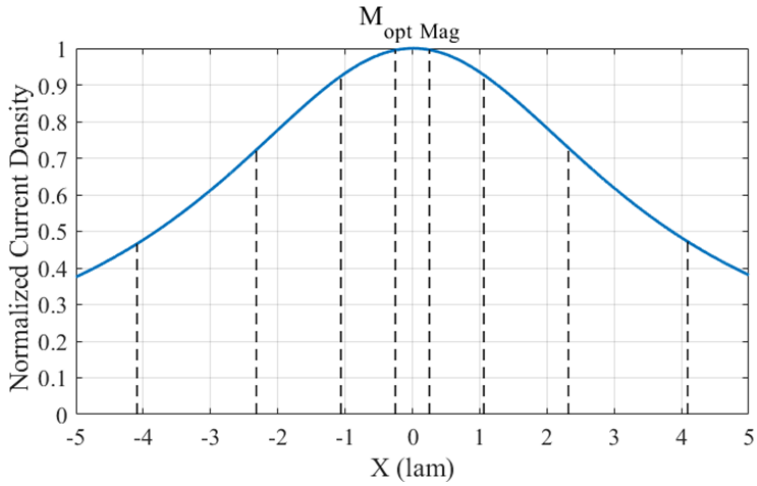

(a)

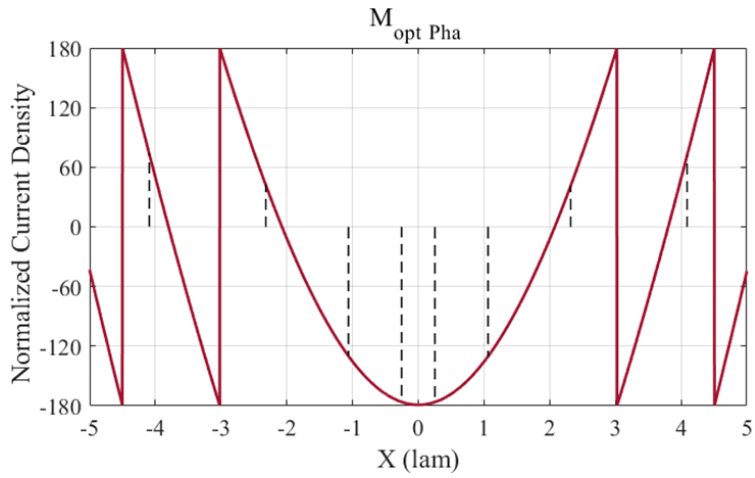

(b)

Fig. 5.6. Concept of density tapering (a) Magntidue plot. (b) Phase plot.

5.3.4. Results and Discussions

The resulting array is shown in the Fig. 5.7. and the efficiency is compared by using the same number, and same size of regular arrays. The efficiency is defined as the ratio of the power applied to the load of the base array to the power emitted by the mobile antenna, as defined in the previous section. The tapering parameter $\Delta_{d_{min}}$is set to $0.2L_p$. According to the results in Fig. 5.7., the efficiency of DT array is improved 20% compared than same number of regular arrays.

For additional performance comparison, simulation is performed for the 13x13 regular array, which has similar size. One side of the density tapered array is 743 mm, and the 13x13 regular array is 762 mm. The thinning ratio becomes 100/169, which is about 59%. The efficiency of the regular array with the similar size is found to be about 44.6%. Therefore, even if only 59% of the total number of arrays is used, the efficiency is reduced by only 9.6%. As a result, it can be seen that while reducing the number of elements, the efficiency is only slightly reduced. The results are described in the Fig. 5.8 using table.

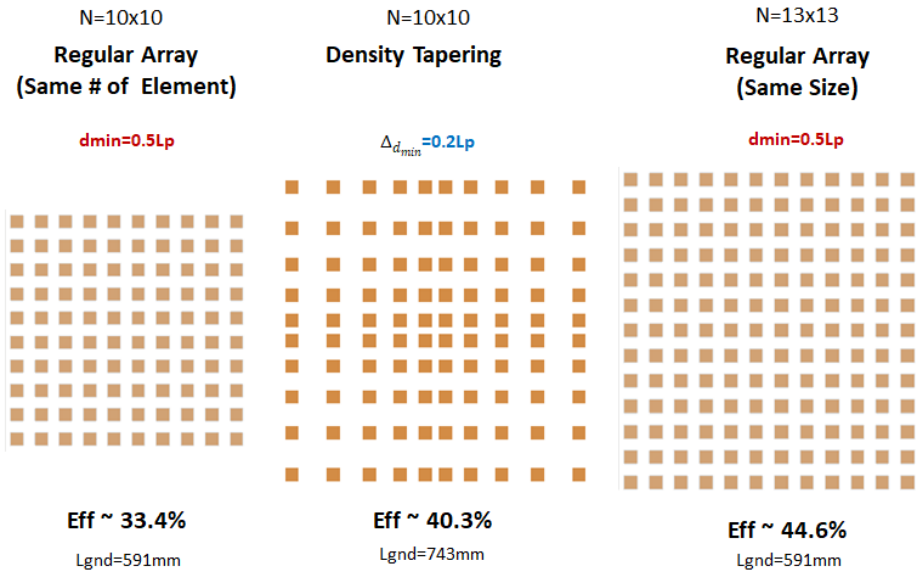

Fig. 5.7. Results of density tapering and regular arrays

	Regular Array (10x10)	Thinned Array	Regular Array (13x13)
Number of Antennas	100	100	169 (-41%)
Efficiency (%)	33.4 (+10%)	40.3	44.6 (-10%)
Area (m^2)	0.349	0.552	0.581

Weight, Cost, Power Loss (Heat)

Fig. 5.8. Results of density tapering and regular arrays

In practical scenarios, the mobile antenna can be placed slightly away from the center. Therefore, it is important to be able to charge even the mobile is not placed at the center. The PTE of regular array and DT arrays are compared when the mobile is moved from the center with offset distances as shown in the Fig. 5.9. The efficiency drops when the mobile is moved to x−axis and y−axis are plotted in the Fig. 5.10, showing that the DT results better PTE than same number of regular array. It indicates that the DT is also advantage when the mobile is off center, since the DT can cover wider transmitting area than 10 x 10 regular array.

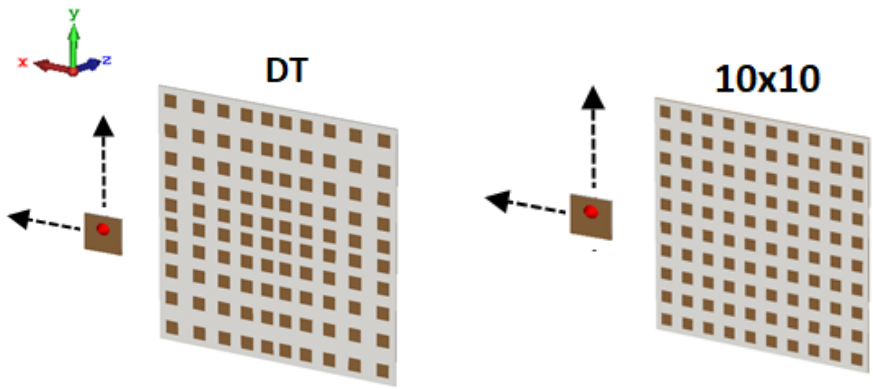

(a)

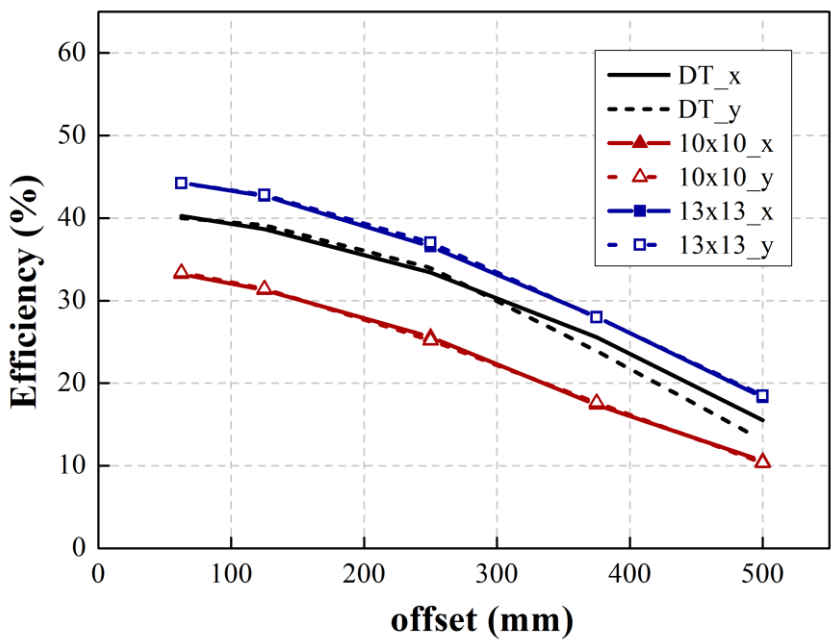

(b)

Fig. 5.9. (a) Configuration of the R-WPT scenario when the mobile is slightly moved from the center. (b) The efficiency drop of regular arrays and DT arrays.

5.4. Conclusion

This section contains the issue of implementing the ideal optimal current distribution as a real antenna. Since the ideal current sheet cannot be used in the actual R−WPT scenario, the implementation of the derived current distribution also has an important meaning.

In this study, the way to improve the efficiency while maintaining the number of arrays is described. First, a pattern matching method is performed by applying a genetic algorithm with binary sequence gene, which means the on/off state of each element. Second, density tapering that determines the location of the antenna according to the magnitude of the current is. As a result, both methods showed improved efficiency compared to the same number of regular arrays. Among the two approaches, density tapering, which is a deterministic approach, shows better performance compared to the results with genetic algorithm with binary sequence.

Using the methodology presented in this study, it is possible to design a transmitter array that is lighter, cheaper than densely arranged regular array. In addition, the thinned array is advantageous when the mobile antenna is slightly moved from the center. It is expected that the proposed array thinning can be useful in actual implementation of a WPT system.

5.5. References

[1] C. A. Balanis, Antenna Theory: Analysis and Design, 3rd e.d., Wiley, 2005.

[2] B. D. Steinberg, Principles of Aperture and Array System Design, Wiley, 1976.

[3] X. Wang, E. Aboutanios, and M. G. Amin, "Thinned array beampattern synthesis by iterative Soft-Thresholding-Based optimization algorithms," IEEE Transactions on Antennas and Propagation, vol. 62, no. 12, pp. 6102-6113, 2014.

[4] M. S. Narasimhan and B. Philips, “Synthesis of near-field patterns of arrays,” IEEE Trans. Antennas Propag., vol. 35, no. 2, pp. 212–218, Feb. 1987.

[5] Z. X. Huang and Y. J. Cheng, "Near-Field pattern synthesis for sparse focusing antenna arrays based on bayesian compressive sensing and convex optimization,"IEEE Trans. Antennas Propag., vol. 66, no. 10, pp. 5249-5257, 2018.

[6] G. Oliveri, L. Poli, and A. Massa, "Maximum Efficiency Beam Synthesis of Radiating Planar Arrays for Wireless Power Transmission,"IEEE Trans. Antennas Propag., vol. 61, no. 5, pp. 2490-2499, 2013.

[7] S. Clauzier, S. M. Mikki, and Y. M. M. Antar, "Design of near-field synthesis arrays through global optimization," IEEE Trans. Antennas Propag., vol. 63, no. 1, pp. 151-165, 2015.

[8] F. J. Ares-Pena, J. A. Rodriguez-Gonzalez, E. Villanueva-Lopez, and S. R. Rengarajan, “Genetic algorithms in the design and

optimization of antenna array patterns," IEEE Trans. Antennas Propag., vol. 47, no. 3, pp. 506–510, Mar. 1999

[9] M. Serhir, P. Besnier, and M. Drissi, "Antenna modeling based on a multiple spherical wave expansion method: application to an antenna array,"IEEE Trans. Antennas Propag., vol. 58, no. 1, pp. 51–58, 2010.

[10] M. Serhir, J.–M. Geffrin, A. Litman, and P. Besnier, "Aperture antenna modeling by a finite number of elemental dipoles from spherical field measurements,"IEEE Trans. Antennas Propag., vol. 58, no. 4, pp. 1260–1268, 2010.

[11] W.Geyi, Foundations of Applied Electrodynamics, Wiley, 2010.

[12] L. Shan and W. Geyi, "Optimal design of focused antenna arrays,"IEEE Trans. Antennas Propag., vol. 62, no. 11, pp. 5565–5571, 2014.

[13] R. L. Haupt and Y. Rahmat–Samii, "Antenna array developments: a perspective on the past, present and future," IEEE Antennas and Propagation Magazine, vol. 57, no. 1, pp. 86–96, 2015.

[14] R. L. Haupt, "Optimized element spacing for low sidelobe concentric ring arrays,"IEEE Trans. Antennas Propag., vol. 56, no. 1, pp. 266–268, 2008.

[15] O. M. Bucci, M. D'Urso, T. Isernia, P. Angeletti, and G. Toso, "Deterministic synthesis of uniform amplitude sparse arrays via

new flexible density taper techniques," IEEE Trans. Antennas Propag., vol. 58, no. 6, pp. 1949–1958, Jun. 2010.

[16] O. M. Bucci, T. Isernia, and A. F. Morabito, "An effective deterministic procedure for the synthesis of shaped beams by means of Uniform-Amplitude linear sparse arrays,"IEEE Trans. Antennas Propag., vol. 61, no. 1, pp. 169-175, 2013.

[17] O. M. Bucci, M. D'Urso, T. Isernia, P. Angeletti, and G. Toso, "Deterministic synthesis of uniform amplitude sparse arrays via new density taper techniques,"IEEE Trans. Antennas Propag., vol. 58, no. 6, pp. 1949-1958, 2010.

초 록

본 논문에는 방사하는 전자파를 이용한 무선 전력 전송에 대해 집중적으로 연구를 진행하였다. 보다 구체적으로는, 무지향성 안테나의 분석과 설계, 자유공간과 손실매질에서의 최적 송신 전류 분포, 전송 효율의 한계에 대한 연구를 기술하였다. 추가적으로, 전자파의 인체 영향에 대한 비교 및 이론적인 최적 전류 분포의 효과적 구현에 대한 연구를 진행하였다. 본 연구에서는 방사형 무선전력전송을 전원을 공급 유무에 따라 수동형과 능동형 무선전력전송으로 구분하고, 수동형 방사 무선전력전송부터 능동형 방사 무선전력전송까지의 연구를 순차적으로 기술하였다.

먼저, 수동형 방사 무선전력전송 연구에서는 전자파 에너지 하베스팅용 안테나에 대한 분석 및 설계에 대한 연구를 진행하였다. 수동 방사 무선전력전송의 상황을 고려하여 등방성 패턴, 전기적으로 작은 크기, 높은 효율 특성을 나타내는 안테나를 제안하였다. 전기적으로 소형이면서 등방성 패턴을 방사하는 SRR이 기본 구조로 활용되었다. SRR에 대한 이론적 분석을 진행하였고, 시뮬레이션 결과와 잘 맞는 것을 확인하였다. 분석에 기초하여 FSRR 안테나를 설계하였고, 측정을 통해 제안한 아이디어를 검증하였다. 수신 파워의 크기를 향상시키기 위해, 이중 대역 및 확장된 대역에서 동작하는 FSRR 안테나를 추가로 설계하였다. 제안된 구조는 선행연구와 비교하였을 때, 상대적으로 우수한 성능을 보여주었다. 한편 수동형 방사 무선 전력전송의 경우, 주변의 낮은 전력 밀도로 인해 수신 전력이 매우 낮은 한계점이 존재한다. 따라서, 송신 타워를 이용해 모바일 안테나로 무선 전력을 전송할 수 있는 능동형 방사 무선전력전송에 대한 후속 연구를 진행하였다.

능동형 방사 무선전력전송에서는, 송신 타워를 활용하여 모바일 기기에 효과적으로 무선전력전송을 수행하는 방법에 대한 연구를

진행하였다. 본 연구에서는 방사형 무선전력전송의 효율을 최대화 하는 송신 전류분포와 주어진 면적을 활용할 때 얻을 수 있는 최대 한계 효율을 이론적으로 도출하였다. 본 연구의 결과를 통해, 기존의 방식으로는 파악할 수 없었던 중거리 무선전력전송 효율의 최대 한계치와 송신 전류분포의 최적 형태를 파악할 수 있다. 연구의 결론에 따르면, 수신하는 안테나의 송신 방사 패턴이 효율을 결정함에 있어 중요한 역할을 하였다. 제안한 이론을 실제 안테나에 적용하여 선행연구와 비교를 하였고, 선행 연구로 파악할 수 없는 이론적 한계 효율을 도출하였다. 제안한 연구를 일반적인 상황으로 확장하기 위해 손실 매질 내부에서의 무선전력전송에 대한 추가 연구를 진행하였다. 손실 매질이 있는 경우에서도 최적 전류 분포와 효율의 최대 한계치를 도출하였다. 최적 송신 전류를 활용하여, 실제 안테나 어레이를 구현하고 인체 팬텀에 미치는 영향을 파악해보았다.

마지막으로, 앞서 도출한 이론적인 전류분포를 실제 안테나로 구현하는 방법에 대해 연구를 진행하였다. 선행 연구를 참고하여, 이상적인 전류분포를 thinned 배열로 구현하는 두가지 방법을 제안하였다. 이론적인 전류 분포에 유전 알고리즘을 활용한 방법과, density tapering을 응용한 방법을 적용하였다. 두 방법 모두 동일한 개수의 균등 어레이에 비해 성능이 개선되는 결과를 보였다. 특히 density tapering을 이용하면 같은 개수 및 같은 면적의 격자구조보다 비용, 무게, 효율 등에서 장점이 있으며, 수신기의 위치가 변할 때에도 더 높은 효율로 송신이 가능하다.

주요어: 전자파 에너지 하베스팅 안테나, 방사 무선 전력 전송, 마이크로파 전력 전송, 효율 최적화, 이식 형 의료 기기, Thinned 배열

학 번: 2014-22551

감사의 글

전자파에 대한 관심만 있을 뿐, 이해가 부족했던 학생을 받아주시고 학위과정을 지도해주신 남상욱 교수님께 가장 먼저 감사하다는 말씀을 드리고 싶습니다. 겸손한 태도로 스스로에게 엄격하셨던 교수님의 지도를 받으면서, 전공에 대한 지식과 삶을 대하는 태도를 배울 수 있었습니다. 다듬어지지 않은 젊은 시기에, 교수님의 지도를 받을 수 있었던 것이 커다란 행운이었다고 생각합니다. 졸업한 이후에도 교수님의 가르침을 되새기며 진지하게 고민하고 배우면서 성장해 나가도록 하겠습니다.

바쁘신 와중에도 시간을 내어 학위논문을 지도해 주신 서광석 교수님, 이정우 교수님, 오정석 교수님, 그리고 박익모 교수님께도 감사의 인사를 드립니다. 교수님들께서 조언 해주신 부분을 바탕으로 논문의 부족한 부분을 보완하고, 다양한 관점에서 저의 연구를 바라볼 수 있었습니다.

짧지 않은 학위 과정 동안 동고동락한 서울대학교 전파공학연구실의 모든 구성원분들께도 감사의 인사를 드립니다. 선후배 분들과 함께 지내면서 연구의 어려움도,, 개인적인 삶의 고됨도 이겨낼 수 있었습니다. 연구실을 졸업한 이후에도 함께 삶을 헤쳐나가는 인연이 되길 바라겠습니다.

마지막으로, 천방지축 막내 아들을 언제까지나 믿어주시고 물심양면으로 지원해 주신 부모님과, 인생의 선배이자 때로는 편안한 친구가 되어주는 누나들에게 진심 가득한 감사의 마음을 전하고 싶습니다. 가족의 따뜻한 지원과 응원 덕분에 어려움을 마주해도 긍정적으로 이겨낼 수 있었습니다. 항상 힘이 되어주는 가족들에게

한없는 존경과 사랑의 마음을 표합니다.

본 논문을 작성함에 도움주신 많은 분들에게 다시 한번 감사의 인사를 올립니다.

2020년 8월

김준홍 올림